8-2022

Natural and Experimental Slow Slip Observed Along Shallow Hematite Faults

Alexandra A. DiMonte
Utah State University

NATURAL AND EXPERIMENTAL SLOW SLIP OBSERVED ALONG SHALLOW HEMATITE FAULTS

by

Alexandra A. DiMonte

A thesis submitted in partial fulfillment

of the requirements for the degree

of

MASTER OF SCIENCE

in

Geology

Approved:

_____	_____
Alexis K. Ault, Ph.D. Major Professor	Kelly K. Bradbury, Ph.D. Committee Member
_____	_____
James P. Evans, Ph.D. Committee Member	D. Richard Cutler, Ph.D. Vice Provost of Graduate Studies

UTAH STATE UNIVERSITY

Logan, Utah

2022

ABSTRACT

Natural and Experimental Slow Slip Observed Along Shallow Hematite Faults

by

Alexandra A. DiMonte

Utah State University, 2022

Major Professor: Alexis K. Ault
Department: Geosciences

Transient, shallow slow slip is an essential component of the earthquake cycle observed in continental strike-slip fault systems. Exhumed faults provide a geologic record of slip over numerous earthquake cycles. Hematite commonly forms in shallow fault zones, and its textures and (U-Th)/He thermochronometric data patterns potentially distinguish slip rates and mineralization events. Laboratory shear experiments constrain hematite frictional behavior. The San Andreas fault (SAF) near the Mecca Hills experiences episodic slow slip. Exhumed basement-hosted faults in a flower-structure with the SAF in this region contain dense networks of minor hematite-coated slip surfaces. Hematite exhibits a nanometer-scale platy morphology that forms anastomosing and S-C fabrics, injection veins, and reworked clasts that imply episodic precipitation and ongoing deformation at subseismic rates. Hematite (U-Th)/He data indicate episodic hematite mineralization at <1.5 km within fault zones at ~0.8-0.4 Ma. These results imply mineralization and off-fault deformation at <1 Ma in the Mecca Hills is associated with

transient slip at subseismic rates. Comparison of these observations to results from rotary-shear experiments conducted at slow slip rates (<1 mm/s) and low (<8.5 MPa) normal stress on specular hematite slabs informs rate-and-state friction parameters and He loss during deformation. Hematite has a low (~0.35) coefficient of friction and displays primarily velocity-neutral to velocity-strengthening behavior. Generated hematite gouge shows evidence for He loss without associated temperature rise, which typically causes He loss by volume-diffusion. Rather, He loss occurred solely by extreme grain size reduction to expose He previously held within the crystal lattice, implying natural hematite ultracataclasite or gouge may experience He loss by this mechanism. These results imply that hematite can accommodate stable sliding in a fault zone when present within a network of slip surfaces.

(173 pages)

PUBLIC ABSTRACT

Natural and experimental slow slip observed along shallow hematite faults

Alexandra A. DiMonte

Fault slip relieves stress in the shallow crust by slipping suddenly during earthquakes, but some faults also slip slowly in between earthquakes. Exhumed faults, brought up to the Earth's surface from depth, preserve a record of fault processes and slip rates informed by fault rock structures, textures, and chemistry. Hematite, a common iron-oxide mineral that precipitates on fault surfaces, exhibits crystal textures that potentially indicate past slip rate. Hematite can be dated using the radioisotopic system of (U-Th)/He thermochronometry, which constrains the time when He is trapped within a crystal, a process that is a function of temperature. Exhumed faults that are parallel and connect to the San Andreas Fault (southernmost California) at depth cut crystalline rock and contain networks of small, hematite-coated faults. Here, hematite displays crystal morphology and structures that indicate hematite formed episodically and, following formation, repeatedly slipped at slow rates. Hematite (U-Th)/He dates show hematite formed at shallow depths (<1.5 km) within the past million years. These data imply the shallow portion of the San Andreas fault and nearby faults with hematite-bearing rock deformed at slow rates in the past. We compare these observations to fault surfaces that were generated in a lab using shear experiments at slow rates and characterize rock friction properties influencing fault behavior. Experiments show hematite is weak and strengthens with increasing velocity, which suggests hematite can accommodate slow slip. (U-Th)/He data from lab faults indicate He was released from hematite at cooler

temperatures than those that typically cause He loss, solely because grain size reduction during faulting creates new particle surfaces where He was previously trapped. This implies natural, tiny hematite particles produced during faulting may have younger (U-Th)/He dates than expected. Natural and experimental observations reveal hematite fault networks can host transient slow slip.

ACKNOWLEDGMENTS

I would like to extend a first and foremost thank you to my advisor Dr. Alexis Ault for her ongoing insight and support that drove improvements to this research and guided my development as a researcher and communicator. I would also like to thank my committee members Dr. Kelly Bradbury and Dr. Jim Evans for their feedback and knowledge of fault processes and the geology of the Mecca Hills, California. I also wish to extend thanks to my unofficial committee member Greg Hirth for his feedback and insight into fault mechanics and friction experiments.

Thank you to Alexis, Emma (Ema) Armstrong, Dr. Dennis Newell, and Kelly for field assistance and aid in sampling and making structural observations in California. Jim and Dr. Susanne Jänecke led a field trip to the Salton Trough, including Mecca Hills, that taught me the spatial-temporal context of geology in Southern California, and Susanne offered some suggestions that guided this research. Dr. Uttam Chowdhury and Dr. Peter Reiners provided analytical support at the University of Arizona's Helium Lab, and Dr. FenAnn Shen provided analytical support for the SEM at Utah State's Core Microscopy Lab. Dr. Cameron Meyers provided suggestions and analytical support and aided in the development of the experimental setup at Brown University's Rock Deformation Lab. Thank you to current and former FONTTTS members Jordan Jensen, Rob McDermott, and Amy Moser for providing info that aided development of this work. Finally, thanks to my family, friends, and fellow overlapping graduate students for support.

This research was supported by NSF (EAR-2039727) and SCEC awards (21068) to Alexis Ault and Greg Hirth (Brown University), a USGS-NEHRP grant (G15AP00011) to Kelly Bradbury and James Evans, a student grant from the Geological Society of America, the Graduate Research and Creative Opportunities award from the graduate school, and Beryl O. & Tura H Springer Memorial, J. Stewart Williams, Peter R. McKillop, and Robert Q. Oaks, Jr. scholarships from the Geosciences Department of Utah State University.

Alexandra A. DiMonte

CONTENTS

Page

LIST OF TABLES

Table Page

LIST OF FIGURES

Figure Page

CHAPTER I

INTRODUCTION

Geodesy and seismology reveal transient increases in slip rate along faults occurring over days to months (Jolivet and Frank, 2020, and references therein). This "slow slip" is ubiquitous within subduction zones and continental strike-slip faults both above and below the seismogenic zone and throughout the earthquake cycle (Bürgmann, 2018; Jolivet and Frank, 2020). However, the deformation mechanics and geology of faults that host shallow slow slip are poorly understood, limiting our ability to bridge between geologic and geophysical observations, construct accurate models of fault slip, and inform earthquake hazards.

Exhumed faults record deformation accumulated over numerous earthquake cycles and provide a structural and geochemical record of fault slip. Laboratory experiments conducted at short, observable timescales offer insight into deformation mechanisms operative at different temperature, pressure, and strain rate regimes. These mechanisms produce the textural and/or chemical signatures detected in the rock record. Integrating observations from the field and the lab informs the deformation processes currently operating in shallow fault zones where slow slip occurs, yielding crucial information for interpreting geophysical data and for models of earthquake propagation and arrest.

Fault rock composition and mineralogy, as well as the distribution of slip surfaces, influence the mechanical behavior of faults because minerals and rocks have unique frictional properties. Hematite is common in shallow continental fault zones, yet how it deforms throughout the earthquake cycle is not constrained. Prior work has

focused on how hematite accommodates coseismic slip (Ault et al., 2019; Ault et al., 2015; Evans et al., 2014; McDermott et al., 2017; Odlum et al., 2022; Taylor et al., 2021). The southernmost San Andreas fault in the vicinity of Mecca Hills, CA, hosts shallow, transient slow slip (Allen et al., 1972; Parker et al., 2021). In Mecca Hills, shallowly exhumed faults parallel to and in a flower structure with the San Andreas fault dissect basement and overlying Plio-Pleistocene sedimentary rocks (Bergh et al., 2019; Fattaruso et al., 2014; McNabb et al., 2017; Sylvester and Smith, 1976). Where some of these structures cut crystalline basement, networks of hematite-coated slip surfaces (Moser et al., 2017) provide an opportunity to explore if and how hematite accommodates or promotes deformation at slow slip rates. Rotary shear experiments conducted at slow rates on hematite slabs yield additional mechanical and frictional constraints and inform data from natural hematite faults.

1.1 Fault zones and the earthquake cycle

Fault zones with measurable displacement form as a response to the regional and local stress state (Van der Pluijm and Marshak, 2004). Classic models of fault zones delineate a brittle, elastic portion in the shallow crust comprising ‘cataclastic’ rocks (i.e., gouge or breccia in the shallowest portion of the fault zone, and cataclasite below depths of ~3-5 km), a brittle-plastic transition zone at depths of ~10-15 km, and a deeper viscous shear zone comprising plastically-deformed mylonites (Scholz, 1988; Sibson, 1977). Brittle faults have a fault core, an area of significant comminution where most strain (or slip) is accommodated, and a damage zone characterized by a wider distribution of minor

faults, fractures, and folds (Ben-Zion and Sammis, 2003; Caine et al., 1996; Faulkner et al., 2010).

Earthquakes nucleate within the seismogenic zone, above the brittle-plastic transition zone, where frictional processes dominate (Marone and Scholz, 1988; Scholz, 1988). Earthquakes may also propagate to depths below the seismogenic zone - within the transition zone, where frictional processes occur in conjunction with plastic deformation mechanisms (Scholz, 1988; Tse and Rice, 1986). In California, earthquakes typically nucleate at depths up to ~30 km (Zuza and Cao, 2020) and the majority of hypocenters are located at 2-14 km (Hauksson and Meier, 2019). The plastic region of fault zones at depth primarily slips due to thermally-activated plastic-viscous processes (Scholz, 1988; Sibson, 1977). The shallowest portion of fault zones experience aseismic creep, or slow (plate-rate velocity) fault slip occurring between earthquakes, due to frictional properties of shallow crustal materials (Harris, 2017; Marone and Saffer, 2007; Marone and Scholz, 1988). Geodesy reveals a deficit in slip occurring during earthquakes in the shallowest portion of the crust, and this deficit may be explained by the production of off-fault damage and by accommodation within voluminous fault damage zones (Jänecke et al., 2018; Kaneko and Fialko, 2011; Roten et al., 2017). Fault zones in nature are temporally and spatially complex with heterogenous fault structure and composition. Thus, fault behavior evolves through time, transitions with depth, and varies along strike (Fagereng and Beall, 2021; Williams et al., 2021).

Brittle fault behavior is governed by elasticity in the surrounding rock and by the frictional strength of the fault materials (Scholz, 2019). Stored elastic strain energy accumulates in a fault zone until the frictional strength of the rock is exceeded so that

failure occurs and induces fault slip (via Amonton's Law, Eqn 1.1), where σ_s is shear stress, μ is the coefficient of friction, σ_n is normal stress, and P_f is pore fluid pressure (Kanamori and Brodsky, 2004).

$$\sigma_s = \mu(\sigma_n - P_f) \qquad \text{Equation 1.1}$$

Fault stability is often modeled via empirical rate-and-state friction and stick-slip criteria (i.e., spring-slider model) (e.g., Dieterich, 1979; Marone, 1998; Ruina, 1983), and parameters are calculated based on laboratory experiments conducted on gouge or ground surfaces (Beeler et al., 1994). Rate-and-state friction parameters (μ, D_c, a – b) are measured via velocity-step tests during laboratory deformation experiments. A gouge layer or ground planar rock surface is sheared at an imposed velocity, and the coefficient of friction (μ) is observed as this parameter attains a steady-state (μ_{ss}). The velocity is changed, and the coefficient of friction initially jumps before it reaches a new steady state over a displacement, D_c. Fault behavior is also constrained by microphysical models (Thom et al., 2022; Van den Ende et al., 2018).

Multiple laws have been introduced to account for the first-order frictional dependence on velocity and the time-dependent or slip-dependent strength of the contact area (e.g., Beeler et al., 1994; Dieterich, 1979; Linker and Dieterich, 1992; Ruina, 1983). Stability is determined by the sign of the parameter a – b (Eqn. 1.2), where V is velocity (Beeler et al., 1994).

$$a - b = d(\mu_{ss})/d(lnV) \qquad \text{Equation 1.2}$$

If $a - b > 0$, velocity-strengthening behavior is predicted, implying the fault strengthens with increasing velocity so stable sliding occurs, which would act to impede earthquake propagation in nature (Marone, 1998). An $a - b$ value of ~ 0 is termed velocity-neutral. If $a - b < 0$, velocity-weakening is predicted, implying a velocity increase induces fault weakening (Marone, 1998; Scholz, 2019). In this case, sliding may be unstable or conditionally stable, and stability depends on elastic stick-slip criteria, or stiffness, of the fault and its surroundings (or the fault and loading system, in the laboratory) when subjected to a load (Kanamori and Brodsky, 2004; Leeman et al., 2016; Scholz, 2019).

The earthquake cycle is characterized by preseismic, coseismic, postseismic, and interseismic periods (Scholz, 2019). The preseismic period, or precursory earthquake behavior, may be expressed as foreshocks or slow slip events leading up to earthquake nucleation within the seismogenic zone (Dodge et al., 1996; Obara and Kato, 2016; Rubin and Ampuero, 2005). Coseismic refers to strain release via dynamic earthquake rupture propagation to shallower and deeper depths, or along strike, at seismic slip rates (~1 m/s, Kanamori and Brodsky, 2004; Rowe and Griffith, 2015; Scholz, 2019). Coseismic slip generates a temperature rise due to transfer of frictional work into heat causing dynamic weakening of the fault (e.g., Di Toro et al., 2011; Mase and Smith, 1987; Rice, 2006; Sibson, 1975; Wibberley and Shimamoto, 2005). The postseismic interval manifests as aftershocks, and/or various forms of slow slip including transient, accelerated aseismic creep, or afterslip, that occurs in the shallowest, velocity-strengthening region of a fault to depths of up to 3-5 km (Marone et al., 1991; Mendoza and Hartzell, 1988; Utsu and Ogata, 1995). The interseismic period is characterized by

healing, or the recovery of frictional strength and elastic strain in a locked fault zone, and/or by aseismic creep at shallow depths, viscous deformation at depth, and/or various forms of slow slip (Bürgmann, 2018; Dieterich, 1972; Fialko, 2006; Scholz, 2019).

Slow slip includes a family of transient fault slip at velocities above plate-motion rates and below coseismic slip rates, and are phenomena that are observed seismically and geodetically (Bürgmann, 2018; Jolivet and Frank, 2020). These phenomena are sometimes referred to as slow or silent earthquakes, and slow slip includes tremor, low-frequency and very-low-frequency earthquakes (LFE, VLFE), triggered and spontaneous slow slip events and creep events, episodic tremor and slip (ETS) (e.g., Bilham et al., 2016; Frank et al., 2018; Goulty and Gilman, 1978; Linde et al., 1996; Lowry et al., 2001; Nadeau and McEvilly, 2004; Schwartz and Rokosky, 2007; Shirzaei and Bürgmann, 2013; Wallace et al., 2016; Wei et al., 2013). Tremor, LFEs, and VLFEs are observed via seismology and are often associated with geodetic slip (ETS), but slow slip events and creep events are evident only via geodetic observation (e.g., Bilham et al., 2016; Frank et al., 2018; Goulty and Gilman, 1978; Linde et al., 1996; Lowry et al., 2001; Nadeau and McEvilly, 2004; Schwartz and Rokosky, 2007; Shirzaei and Bürgmann, 2013; Wallace et al., 2016; Wei et al., 2013). Here, we use the term slow slip to refer to fault slip at rates slower than earthquakes ($<10^{-4}$ m/s). Slow slip occurs directly above and below the seismogenic zone, and it may nucleate within transitional or heterogeneous frictional and rheologic regimes (Fagereng and Beall, 2021; Skarbek et al., 2012; Wei et al., 2013). Additional mechanisms suggested to promote slow slip include the presence of pore fluids that act to weaken a fault by reducing effective stress (Saffer and Wallace, 2015), shifts between the mineral phases accommodating deformation

(French and Condit, 2019), or slip stabilization by dilatant hardening (Rudnicki and Chen, 1988; Xing et al., 2019). Slow slip may also arise due to the stress state induced by geometrically complex faults that interact as a system (Romanet et al., 2018).

Laboratory observations of fault slip constrain potential mechanisms of slow slip and aseismic creep, and exhumed faults provide a geochemical and structural record of the phases that accommodate slip over numerous earthquake cycles within a fault zone. Phyllosilicates are secondary minerals that form within fault rocks following mechanical breakdown and/or chemical weathering of the host rock (Janecke and Evans, 1988; Schleicher et al., 2010; Vrolijk and van der Pluijm, 1999; Williams et al., 2021; Wintsch et al., 1995). Phyllosilicates, including clay minerals, micas, serpentine minerals, and Al-rich phyllosilicates, have a low μ (~0.1-0.5) because of their sheet-like crystallographic structures that incorporate varying amounts of water (Behnsen and Faulkner, 2012; Carpenter et al., 2015; Moore and Lockner, 2004; Morrow et al., 2000; Sánchez-Roa et al., 2017; Schleicher et al., 2010), and they influence bulk fault strength even when comprising a small percentage of fault rock composition (Collettini et al., 2009). Phyllosilicates deform by sliding along their cleavage planes, or by dislocation glide, processes which distribute slip and develop an anastomosing fabric (e.g., Arch et al., 1988; Collettini et al., 2009; Evans, 1988; French et al., 2015; Niemeijer et al., 2010; Schleicher et al., 2010; Tarling and Rowe, 2016; Vannucchi, 2019). Additionally, phyllosilicates primarily display velocity-strengthening to velocity-neutral behavior (Ikari et al., 2011; Moore et al., 2016; Niemeijer et al., 2010; Sánchez-Roa et al., 2017), and in combination with their low μ and anastomosing fabric, promote aseismic creep within thick clay-rich shear zones (Moore et al., 2016; Schleicher et al., 2010).

Prior work has focused on brittle-viscous structures from fault zones exhumed from *below* the seismogenic zone and that are interpreted to have hosted past slow slip events (e.g., Kirkpatrick et al., 2021, and references therein). One study focuses on heterogeneous frictional properties of rocks and brittle-viscous structures from a subduction zone exhumed from above the seismogenic zone where slow slip occurs (Phillips et al., 2020). To date, primarily laboratory studies have investigated the mechanisms of shallow slow slip within continental fault zones and point to potential "universal" slow slip mechanisms. For example, slow slip events may nucleate where faults display velocity-neutral behavior and/or a transition from stable to unstable sliding (Leeman et al., 2018). Alternatively, slow slip reflects stable slip that propagates at an increased velocity (Ikari, 2019). Investigation of shallowly exhumed continental fault rocks adjacent to where shallow slow slip currently occurs may offer insight to the mechanics, and structural and/or geochemical signatures of prior slow slip.

1.2 Hematite (U-Th)/He Thermochronometry

Iron is the fourth-most abundant element in the Earth, and hematite precipitates in a variety of forms from a range of environments within the crust (Allegre et al., 1995; Cornell and Schwertmann, 2003). Hematite (U-Th)/He thermochronometry (hematite He) resolves the low-temperature thermal history of hematite-bearing rocks within the upper crust. In this system, the He diffusion domain is an individual hematite crystal, diffusivity is modulated by the shortest grain dimension, and fractional loss decreases with increasing grain size (Balout et al., 2017; Farley, 2018; Jensen et al., 2018). The grain (domain) size-dependent closure temperature, T_c, or the transition from open to closed

system behavior with respect to He retentivity, is ~50-250 °C (Balout et al., 2017; Farley, 2018) assuming a 10 °C/Ma cooling rate.

Hematite often precipitates as microcrystalline aggregates comprising various grain sizes (Cornell and Schwertmann, 2003). Arrhenius relationships, which define diffusivity as a function of temperature, from ^{4}He and $^{4}He/^{3}He$ diffusion experiments exhibit a non-linear behavior that is the result of polydomain diffusion (Bahr et al., 1994; Evenson et al., 2014; Farley and Flowers, 2012; Farley and McKeon, 2015; Scoggin et al., 2021). Polydomain diffusion behavior indicates He diffuses simultaneously from domains comprising different crystal sizes. Individual domains all have the same activation energy, but smaller domains release some to all of their He during the lower temperature steps and larger grain-size domains progressively release some fraction of their He at higher temperatures. Because He retention is grain-size dependent and aliquots targeted for hematite He analysis commonly comprise polycrystalline aggregates, aliquot diffusion kinetics and resulting T_c variations reflect the aliquot's grain size distribution, which can be estimated using scanning electron microscopy (SEM) (Ault, 2020; Bahr et al., 1994; Evenson et al., 2014; Farley and Flowers, 2012; Jensen et al., 2018).

Secondary hematite precipitates over a range of ambient temperatures above or below its T_c, so hematite He thermochronometry has the potential to inform the timing and rates of thermal processes including exhumation, mineralization, fluid flow, and seismicity (Ault, 2020; Cooperdock and Ault, 2020). (U-Th)/He dates may record the timing of formation (e.g., Ault et al., 2016; Channer, 2017; Jensen et al., 2018; Lippolt et al., 1995; McDermott et al., 2021; Moser et al., 2017; Taylor et al., 2021; Wernicke and

Lippolt, 1994b; Wu et al., 2019), exhumation or cooling through the grain-size controlled T_c (e.g., Calzolari et al., 2018; Evenson et al., 2014; Farley and Flowers, 2012; Odlum et al., 2022; Scoggin et al., 2021), complete or partial resetting from hydrothermal fluid circulation (e.g., Ault et al., 2016; Scoggin et al., 2021; Wernicke and Lippolt, 1993, 1994a, 1997), or He loss by volume diffusion or recrystallization due to friction-generated heat produced during earthquakes (e.g., Ault et al., 2015; McDermott et al., 2017; Taylor et al., 2021).

Meaningful interpretation of fault rock hematite He data requires (1) knowledge of the plate half-width distribution to calculate the range of aliquot T_c (assuming the individual grain half-width or radius corresponds to the diffusion domain length scale); (2) low-temperature thermochronometry from accessory phases in the host-rock to constrain ambient cooling; (3) textural and geochemical characterization to identify and isolate pure hematite and to determine whether the grains may have comminuted or recrystallized; and (4) careful consideration of hematite He data patterns from individual samples and across a dataset (Ault, 2020). If hematite formed at fluid and ambient crustal temperatures below its T_c, and subsequent He loss did not occur, the (U-Th)/He date is a formation age (Ault, 2020). If mineralization occurred at ambient temperatures above the T_c, and the sample did not experience significant reheating at temperatures below its T_c, the date reflects the time when a sample cooled through its T_c during tectonic or erosional exhumation (Ault, 2020). Regardless of the formation conditions (depth, temperature), reburial, high-temperature fluidization, or flash heating from friction generated heat at asperities can induce He loss that partially or completely resets He dates (Ault, 2020).

To discriminate between exhumation-related cooling or mineralization, a host rock thermochronometer with a similar T_c, such as the apatite or zircon (U-Th)/He (apatite He, zircon He) systems or apatite fission track (AFT) thermochronometry, is utilized. Hematite He data patterns reflecting exhumation may appear as hematite He dates that overlap with bedrock thermochronometry depending on the hematite He T_c. In this scenario, hematite precipitated prior to or while cooling through the T_c, and hematite He dates are minimum formation ages or may imply some degree of resetting. If hematite He dates are younger than adjacent host rock conventional thermochronometry dates, then the hematite He dates do not reflect exhumation, and instead reflect fault-related processes (i.e., fluid flow and associated mineralization, or fault slip).

Textural characterization using SEM aids further interpretation of hematite He dates from fault rocks. Hematite commonly precipitates as hexagonal plates, and the grain size is a function of the fluid and ambient temperatures (Cornell and Schwertmann, 2003). Preservation of the original plate morphology (i.e., specularite) indicates hematite did not experience grain size reduction or recrystallization during seismic slip associated with temperatures that induce significant He loss (Figs. 1.1A, 1.1B; Ault, 2020), so hematite He dates that are younger than host rock dates are mineralization dates. However, analyzed aliquots may include multiple generations of hematite, so that He dates are mixed formation ages (McDermott et al., 2021). Reburial, high-temperature fluidization, or flash heating from friction generated heat at asperities can induce He loss that partially or completely “resets” hematite He dates (Ault, 2020). Hematite exhibits polygonal, lobate, and/or sintered grain morphologies on fault mirror surfaces that may appear iridescent, and these textures reflect coseismic flash heating that induces local He loss (Figs. 1.1C, 1.1D;

Ault et al., 2015; Calzolari et al., 2020; Evans et al., 2014; McDermott et al., 2017). Hematite cataclasite or ultracataclasite indicates grain-size reduction, which changes the T_c, so hematite He dates may reflect a partial memory of higher temperature processes if not reset following comminution. Thus, interpretation of hematite He dates requires careful integration of thermochronometric, geochemical, microtextural, and microstructural data.

1.4. Objectives of this study

The purpose of this study is to investigate if and how hematite-bearing fault surfaces form and then deform in the shallow portion of fault zones. We hypothesize that (1) naturally-deformed hematite-bearing faults can accommodate transient slow slip above the seismogenic zone and, (2) that experimentally-generated hematite faults exhibit frictional behavior that promotes slow slip.

Chapter 2 of this thesis examines the rock record of slow slip in shallowly exhumed fault zones that are part of the San Andreas fault system within the Mecca Hills, CA. Data sets presented in this chapter include field observations of exhumed crystalline basement-hosted faults, scanning electron microscopic images of hematite slip surface textures, and hematite (U-Th)/He dates from hematite-coated slip surfaces found within the damage zones of the Painted Canyon fault and the Platform fault and from minor faults within the Platform block between the two faults. The results presented in this chapter document a textural and geochemical record of Pleistocene slow slip occurring at <1.5 km up to 4 km away from the main San Andreas fault. These interpretations have

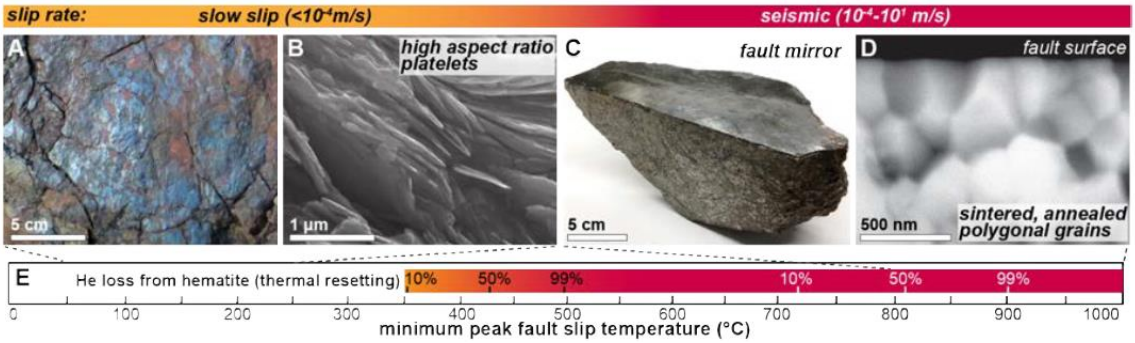

Figure 1.1. Photographs and SEM images of hematite textures that reflect slip rate. **A:** Curvilinear, striated hematite fault surface (Moser et al., 2017). **B:** Nanometer-scale, high aspect ratio platelets reflecting subseismic slip rates. **C:** Hematite fault mirror (Ault et al., 2015). **D:** Sintered, polygonal grains reflecting coseismic temperature rise. **E:** Temperatures required for fractional He loss (%) over 1 s for the grain sizes in B and D.

implications for the geologic mechanisms of slow slip within other shallow-crustal hematite-coated faults. This chapter is currently in revision for *Geology*[1]. Chapter 3 of this thesis investigates the geochemical and textural signatures, as well as deformation mechanics of hematite faults generated via rotary shear experiments at slow slip rates. Data sets presented in this chapter include friction data from single-velocity and velocity-step experiments, scanning electron microscope textures, and hematite (U-Th)/He dates from deformed and undeformed hematite slabs to evaluate He loss at slow slip rates. The results presented in this chapter show that hematite is weak and exhibits primarily velocity-strengthening rate-state frictional behavior at slow slip rates. We demonstrate that extreme grain size reduction and gouge development induces some He loss without an associated temperature rise during fault slip. These observations have implications for the deformation and accommodation of slow slip within hematite-bearing faults in natural fault systems. These results will be expanded upon in the future by conducting additional slow slip experiments using hematite gouge and mixed hematite-clay gouge. A revised version of this chapter will be submitted for publication following additional data analysis.

Chapter 4 synthesizes results from previous chapters and integrates findings from natural and experimental hematite faults. The thesis concludes with a summary of the implications of the research, reviews questions that arose through the work, and provides suggestions for future research directions.

---

[1] DiMonte, A. A., Ault, A. K., Hirth, G., and Bradbury, K. K., in review, Hematite accommodates shallow, transient Pleistocene slow slip in the exhumed southern San Andreas fault system: submitted to Geology.

REFERENCES

Allegre, C. J., Poirier, J.-P., Humler, E., and Hofmann, A. W., 1995, The chemical composition of the Earth: Earth and Planetary Science Letters, v. 134, no. 3-4, p. 515-526.

Allen, C. R., Wyss, M., Brune, J. N., Grantz, A., and Wallace, R. E., 1972, Displacements on the Imperial, Superstition Hills, and San Andreas faults triggered by the Borrego Mountain earthquake: US Geol. Surv. Prof. Pap, v. 787, p. 87-104.

Arch, J., Maltman, A., and Knipe, R., 1988, Shear-zone geometries in experimentally deformed clays: the influence of water content, strain rate and primary fabric: Journal of Structural Geology, v. 10, no. 1, p. 91-99.

Ault, A. K., 2020, Hematite fault rock thermochronometry and textures inform fault zone processes: Journal of Structural Geology, p. 104002.

Ault, A. K., Frenzel, M., Reiners, P. W., Woodcock, N. H., and Thomson, S. N., 2016, Record of paleofluid circulation in faults revealed by hematite (U-Th)/He and apatite fission-track dating: an example from Gower Peninsula fault fissures, Wales: Lithosphere, v. 8, p. 379-385.

Ault, A. K., Jensen, J. L., McDermott, R. G., Shen, F.-A., and Van Devener, B. R., 2019, Nanoscale evidence for temperature-induced transient rheology and postseismic fault healing: Geology.

Ault, A. K., Reiners, P. W., Evans, J. P., and Thomson, S. N., 2015, Linking hematite (U-Th)/He dating with the microtextural record of seismicity in the Wasatch fault damage zone, Utah, USA: Geology, v. 43, p. 771-774.

Bahr, R., Lippolt, H. J., and Wernicke, R. S., 1994, Temperature-induced ^{4}He degassing of specularite and botryoidal hematite: A ^{4}He retentivity study: Journal of Geophysical Research, v. 99, p. 17695-17707.

Balout, H., Roques, J., Gautheron, C., Tassan-Got, L., and Mbongo-Djimbi, D., 2017, Helium diffusion in pure hematite (α-Fe2O3) for thermochronometric applications: A theoretical multi-scale study: Computational and Theoretical Chemistry, v. 1099, p. 21-28.

Beeler, N., Tullis, T., and Weeks, J., 1994, The roles of time and displacement in the evolution effect in rock friction: Geophysical Research Letters, v. 21, no. 18, p. 1987-1990.

Behnsen, J., and Faulkner, D. R., 2012, The effect of mineralogy and effective normal stress on frictional strength of sheet silicates: Journal of Structural Geology, v. 42, p. 49-61.

Ben-Zion, Y., and Sammis, C. G., 2003, Characterization of fault zones: Pure and applied geophysics, v. 160, no. 3, p. 677-715.

Bergh, S. G., Sylvester, A. G., Damte, A., and Indrevær, K., 2019, Polyphase kinematic history of transpression along the Mecca Hills segment of the San Andreas fault, southern California: Geosphere, v. 15, no. 3, p. 901-934.

Bilham, R., Ozener, H., Mencin, D., Dogru, A., Ergintav, S., Cakir, Z., Aytun, A., Aktug, B., Yilmaz, O., and Johnson, W., 2016, Surface creep on the North Anatolian fault at Ismetpasa, Turkey, 1944–2016: Journal of Geophysical Research: Solid Earth, v. 121, no. 10, p. 7409-7431.

Bürgmann, R., 2018, The geophysics, geology and mechanics of slow fault slip: Earth and Planetary Science Letters, v. 495, p. 112-134.

Caine, J. S., Evans, J. P., and Forster, C. B., 1996, Fault zone architecture and permeability structure: Geology, v. 24, no. 11, p. 1025-1028.

Calzolari, G., Ault, A. K., Hirth, G., and McDermott, R. G., 2020, Hematite (U-Th)/He thermochronometry detects asperity flash heating during laboratory earthquakes: Geology.

Calzolari, G., Rossetti, F., Ault, A. K., Lucci, F., Olivetti, V., and Nozaem, R., 2018, Hematite (U-Th)/He thermochronometry constrains strike-slip faulting on the Kuh-e-Faghan fault, central Iran: Tectonophysics, v. 728-729, p. 41-54.

Carpenter, B., Saffer, D., and Marone, C., 2015, Frictional properties of the active San Andreas Fault at SAFOD: Implications for fault strength and slip behavior: Journal of Geophysical Research: Solid Earth, v. 120, no. 7, p. 5273-5289.

Channer, M., 2017, (Uranium-Thorium)/Helium Thermochronologic Constraints on Secondary Iron-Oxide Mineralization in Southwestern New Mexico.

Collettini, C., Niemeijer, A., Viti, C., and Marone, C., 2009, Fault zone fabric and fault weakness: Nature, v. 462, no. 7275, p. 907-910.

Cooperdock, E. H., and Ault, A. K., 2020, Iron oxide (U–Th)/He thermochronology: new perspectives on faults, fluids, and heat: Elements: An International Magazine of Mineralogy, Geochemistry, and Petrology, v. 16, no. 5, p. 319-324.

Cornell, R. M., and Schwertmann, U., 2003, The iron oxides: structure, properties, reactions, occurrences and uses, John Wiley & Sons.

Di Toro, G., Han, R., Hirose, T., De Paola, N., Nielsen, S. B., Mizoguchi, K., Ferri, F., Cocco, M., and Shimamoto, T., 2011, Fault lubrication during earthquakes: Nature, v. 471, no. 7339, p. 494-498.

Dieterich, J. H., 1972, Time-dependent friction in rocks: Journal of Geophysical Research, v. 77, no. 20, p. 3690-3697.

-, 1979, Modeling of rock friction: 1. Experimental results and constitutive equations: Journal of Geophysical Research: Solid Earth, v. 84, no. B5, p. 2161-2168.

DiMonte, A. A., Ault, A. K., Hirth, G., and Bradbury, K. K., in review, Hematite accommodates shallow, transient Pleistocene slow slip in the exhumed southern San Andreas fault system: submitted to Geology.

Dodge, D. A., Beroza, G. C., and Ellsworth, W., 1996, Detailed observations of California foreshock sequences: Implications for the earthquake initiation process: Journal of Geophysical Research: Solid Earth, v. 101, no. B10, p. 22371-22392.

Evans, J. P., 1988, Deformation mechanisms in granitic rocks at shallow crustal levels: Journal of Structural Geology, v. 10, no. 5, p. 437-443.

Evans, J. P., Prante, M. R., Janecke, S. U., Ault, A. K., and Newell, D. N., 2014, Hot faults: iridescent slip surfaces with metallic luster document high-temperature ancient seismicity in the Wasatch fault zone: Geology, v. 42, no. 7, p. 636-626.

Evenson, N. S., Reiners, P. W., Spencer, J., and Shuster, D. L., 2014, Hematite and Mn oxide (U-Th)/He dates from the Buckskin-Rawhide detachment system, western Arizona: constraining the timing of mineralization and hematite (U-Th)/He systematics: American Journal of Science, v. 314, p. 1373-1435.

Fagereng, Å., and Beall, A., 2021, Is complex fault zone behaviour a reflection of rheological heterogeneity?: Philosophical Transactions of the Royal Society A, v. 379, no. 2193, p. 20190421.

Farley, K. A., 2018, Helium diffusion parameters of hematite from a single-diffusion-domain crystal: Geochimica et Cosmochimica Acta, v. 231, p. 117-129.

Farley, K. A., and Flowers, R. M., 2012, (U-Th)/Ne and multidomain (U-Th)/He systematics of a hydrothermal hematite from eastern Grand Canyon: Earth and Planetary Science Letters, v. 359-360, p. 131-140.

Farley, K. A., and McKeon, R. E., 2015, Radiometic dating and temperature history of banded iron formation-associated hematite, Gogebic iron range, Michigan, USA: Geology, v. 43, p. 1083-1086.

Fattaruso, L. A., Cooke, M. L., and Dorsey, R. J., 2014, Sensitivity of uplift patterns to dip of the San Andreas fault in the Coachella Valley, California: Geosphere, v. 10, no. 6, p. 1235-1246.

Faulkner, D. R., Jackson, C. A. L., Lunn, R. J., Schlische, R. W., Shipton, Z. K., Wibberley, C. A. J., and Withjack, M. O., 2010, A review of recent developments concerning the structure, mechanics and fluid flow properties of fault zones: Journal of Structural Geology, v. 32, p. 1557-1575.

Fialko, Y., 2006, Interseismic strain accumulation and the earthquake potential on the southern San Andreas fault system: Nature, v. 441, no. 7096, p. 968-971.

Frank, W. B., Rousset, B., Lasserre, C., and Campillo, M., 2018, Revealing the cluster of slow transients behind a large slow slip event: Science advances, v. 4, no. 5, p. eaat0661.

French, M., Chester, F., and Chester, J., 2015, Micromechanisms of creep in clay-rich gouge from the Central Deforming Zone of the San Andreas Fault: Journal of Geophysical Research: Solid Earth, v. 120, no. 2, p. 827-849.

French, M. E., and Condit, C. B., 2019, Slip partitioning along an idealized subduction plate boundary at deep slow slip conditions: Earth and Planetary Science Letters, v. 528, p. 115828.

Goulty, N. R., and Gilman, R., 1978, Repeated creep events on the San Andreas fault near Parkfield, California, recorded by a strainmeter array: Journal of Geophysical Research: Solid Earth, v. 83, no. B11, p. 5415-5419.

Harris, R. A., 2017, Large earthquakes and creeping faults: Reviews of Geophysics, v. 55, no. 1, p. 169-198.

Hauksson, E., and Meier, M.-A., 2019, Applying depth distribution of seismicity to determine thermo-mechanical properties of the seismogenic crust in Southern California: comparing lithotectonic blocks: Pure and Applied Geophysics, v. 176, no. 3, p. 1061-1081.

Ikari, M. J., 2019, Laboratory slow slip events in natural geological materials: Geophysical Journal International, v. 218, no. 1, p. 354-387.

Ikari, M. J., Marone, C., and Saffer, D. M., 2011, On the relation between fault strength and frictional stability: Geology, v. 39, no. 1, p. 83-86.

Janecke, S. U., and Evans, J. P., 1988, Feldspar-influenced rock rheologies: Geology, v. 16, no. 12, p. 1064-1067.

Jänecke, S. U., Markowski, D. K., Evans, J. P., Persaud, P., and Kenney, M., 2018, Durmid ladder structure and its implications for the nucleation sites of the next

M> 7.5 earthquake on the San Andreas fault or Brawley seismic zone in southern California: Lithosphere, v. 10, no. 5, p. 602-631.

Jensen, J. L., Reiners, P. W., Siddoway, C. S., Ault, A. K., Thomson, S. N., and Steele-MacInnis, M., 2018, Single-crystal hematite (U-Th)/He dates and fluid inclusions document Cryogenian seismic clastic injection in granite: Earth and Planetary Science Letters, v. 500, p. 145-155.

Jolivet, R., and Frank, W., 2020, The transient and intermittent nature of slow slip: AGU Advances, v. 1, no. 1, p. e2019AV000126.

Kanamori, H., and Brodsky, E. E., 2004, The physics of earthquakes: Reports on Progress in Physics, v. 67, p. 1429-1496.

Kaneko, Y., and Fialko, Y., 2011, Shallow slip deficit due to large strike-slip earthquakes in dynamic rupture simulations with elasto-plastic off-fault response: Geophysical Journal International, v. 186, no. 3, p. 1389-1403.

Kirkpatrick, J. D., Fagereng, Å., and Shelly, D. R., 2021, Geological constraints on the mechanisms of slow earthquakes: Nature Reviews Earth & Environment, v. 2, no. 4, p. 285-301.

Leeman, J., Marone, C., and Saffer, D., 2018, Frictional mechanics of slow earthquakes: Journal of Geophysical Research: Solid Earth, v. 123, no. 9, p. 7931-7949.

Leeman, J., Saffer, D., Scuderi, M., and Marone, C., 2016, Laboratory observations of slow earthquakes and the spectrum of tectonic fault slip modes: Nature communications, v. 7, no. 1, p. 1-6.

Linde, A. T., Gladwin, M. T., Johnston, M. J., Gwyther, R. L., and Bilham, R. G., 1996, A slow earthquake sequence on the San Andreas fault: Nature, v. 383, no. 6595, p. 65-68.

Linker, M., and Dieterich, J. H., 1992, Effects of variable normal stress on rock friction: Observations and constitutive equations: Journal of Geophysical Research: Solid Earth, v. 97, no. B4, p. 4923-4940.

Lippolt, H. J., Wernicke, R. S., and Bahr, R., 1995, Paragenetic specularite and adularia (Elba, Italy): concordant (U+Th)-He and K-Ar ages: Earth and Planetary Science Letters, v. 132, p. 43-51.

Lowry, A. R., Larson, K. M., Kostoglodov, V., and Bilham, R., 2001, Transient fault slip in Guerrero, southern Mexico: Geophysical Research Letters, v. 28, no. 19, p. 3753-3756.

Marone, C., 1998, Laboratory-derived friction laws and their application to seismic faulting: Annual Review of Earth and Planetary Sciences, v. 26, no. 1, p. 643-696.

Marone, C., and Saffer, D. M., 2007, Fault friction and the upper transition from seismic to aseismic faulting: The seismogenic zone of subduction thrust faults, p. 346-369.

Marone, C., and Scholz, C., 1988, The depth of seismic faulting and the upper transition from stable to unstable slip regimes: Geophysical Research Letters, v. 15, no. 6, p. 621-624.

Marone, C. J., Scholtz, C., and Bilham, R., 1991, On the mechanics of earthquake afterslip: Journal of Geophysical Research: Solid Earth, v. 96, no. B5, p. 8441-8452.

Mase, C. W., and Smith, L., 1987, Effects of frictional heating on the thermal, hydrologic, and mechanical response of a fault: Journal of Geophysical Research: Solid Earth, v. 92, no. B7, p. 6249-6272.

McDermott, R. G., Ault, A. K., and Caine, J. S., 2021, Dating fault damage along the eastern Denali fault zone with hematite (U-Th)/He thermochronometry: Earth and Planetary Science Letters, v. 563, p. 116872.

McDermott, R. G., Ault, A. K., Evans, J. P., and Reiners, P. W., 2017, Thermochronometric and textural evidence for seismicity via asperity flash heating on exhumed hematite fault mirrors, Wasatch fault zone, UT, USA: Earth and Planetary Science Letters, v. 471, p. 85-93.

McNabb, J. C., Dorsey, R. J., Housen, B. A., Dimitroff, C. W., and Messé, G. T., 2017, Stratigraphic record of Pliocene-Pleistocene basin evolution and deformation within the southern San Andreas fault zone, Mecca Hills, California: Tectonophysics, v. 719, p. 66-85.

Mendoza, C., and Hartzell, S. H., 1988, Aftershock patterns and main shock faulting: Bulletin of the Seismological Society of America, v. 78, no. 4, p. 1438-1449.

Moore, D. E., and Lockner, D. A., 2004, Crystallographic controls on the frictional behavior of dry and water-saturated sheet structure minerals: Journal of Geophysical Research: Solid Earth, v. 109, no. B3.

Moore, D. E., Lockner, D. A., and Hickman, S., 2016, Hydrothermal frictional strengths of rock and mineral samples relevant to the creeping section of the San Andreas Fault: Journal of Structural Geology, v. 89, p. 153-167.

Morrow, C., Moore, D. E., and Lockner, D., 2000, The effect of mineral bond strength and adsorbed water on fault gouge frictional strength: Geophysical research letters, v. 27, no. 6, p. 815-818.

Moser, A. C., Evans, J. P., Ault, A. K., Janecke, S. U., and Bradbury, K. K., 2017, (U-Th)/He thermochronometry reveals Pleistocene punctuated deformation and synkinematic hematite mineralization in the Mecca Hills, southernmost San Andreas Fault zone: Earth and Planetary Science Letters, v. 476, p. 87-99.

Nadeau, R. M., and McEvilly, T. V., 2004, Periodic pulsing of characteristic microearthquakes on the San Andreas fault: Science, v. 303, no. 5655, p. 220-222.

Niemeijer, A., Marone, C., and Elsworth, D., 2010, Fabric induced weakness of tectonic faults: Geophysical Research Letters, v. 37, no. 3.

Obara, K., and Kato, A., 2016, Connecting slow earthquakes to huge earthquakes: Science, v. 353, no. 6296, p. 253-257.

Odlum, M., Ault, A., Channer, M., and Calzolari, G., 2022, Seismicity recorded in hematite fault mirrors in the Rio Grande rift: Geosphere, v. 18, no. 1, p. 241-260.

Parker, J., Donnellan, A., Bilham, R., Ludwig, L. G., Wang, J., Pierce, M., Mowery, N., and Jänecke, S., 2021, Buried aseismic slip and off-fault deformation on the southernmost San Andreas fault triggered by the 2010 El Mayor Cucapah earthquake revealed by UAVSAR: Earth and Space Science, v. 8, no. 8, p. e2021EA001682.

Phillips, N. J., Motohashi, G., Ujiie, K., and Rowe, C. D., 2020, Evidence of localized failure along altered basaltic blocks in tectonic mélange at the updip limit of the

seismogenic zone: Implications for the shallow slow earthquake source: Geochemistry, Geophysics, Geosystems, v. 21, no. 7, p. e2019GC008839.

Rice, J. R., 2006, Heating and weakening of faults during earthquake slip: Journal of Geophysical Research, v. 111, p. B05311.

Romanet, P., Bhat, H. S., Jolivet, R., and Madariaga, R., 2018, Fast and slow slip events emerge due to fault geometrical complexity: Geophysical Research Letters, v. 45, no. 10, p. 4809-4819.

Roten, D., Olsen, K., and Day, S., 2017, Off-fault deformations and shallow slip deficit from dynamic rupture simulations with fault zone plasticity: Geophysical Research Letters, v. 44, no. 15, p. 7733-7742.

Rowe, C. D., and Griffith, W. A., 2015, Do faults preserve a record of seismic slip: a second opinion: Journal of Structural Geology, v. 78, p. 1-26.

Rubin, A. M., and Ampuero, J. P., 2005, Earthquake nucleation on (aging) rate and state faults: Journal of Geophysical Research: Solid Earth, v. 110, no. B11.

Rudnicki, J. W., and Chen, C. H., 1988, Stabilization of rapid frictional slip on a weakening fault by dilatant hardening: Journal of Geophysical Research: Solid Earth, v. 93, no. B5, p. 4745-4757.

Ruina, A., 1983, Slip instability and state variable friction laws: Journal of Geophysical Research: Solid Earth, v. 88, no. B12, p. 10359-10370.

Saffer, D. M., and Wallace, L. M., 2015, The frictional, hydrologic, metamorphic and thermal habitat of shallow slow earthquakes: Nature Geoscience, v. 8, no. 8, p. 594-600.

Sánchez-Roa, C., Faulkner, D., Boulton, C., Jimenez-Millan, J., and Nieto, F., 2017, How phyllosilicate mineral structure affects fault strength in Mg-rich fault systems: Geophysical Research Letters, v. 44, no. 11, p. 5457-5467.

Schleicher, A. M., van der Pluijm, B. A., and Warr, L. N., 2010, Nanocoatings of clay and creep of the San Andreas fault at Parkfield, California: Geology, v. 38, no. 7, p. 667-670.

Scholz, C., 1988, The brittle-plastic transition and the depth of seismic faulting: Geologische Rundschau, v. 77, no. 1, p. 319-328.

Scholz, C. H., 2019, The mechanics of earthquakes and faulting, Cambridge university press.

Schwartz, S. Y., and Rokosky, J. M., 2007, Slow slip events and seismic tremor at circum-Pacific subduction zones: Reviews of Geophysics, v. 45, no. 3.

Scoggin, S. H., Reiners, P. W., Shuster, D. L., Davis, G. H., Ward, L. A., Worthington, J. R., Nickerson, P. A., and Evenson, N. S., 2021, He and 4He/3He thermochronology of secondary oxides in faults and fractures: A regional perspective from southeastern Arizona: Geochemistry, Geophysics. Geosystems, v. 22, p. e2021GC009905.

Shirzaei, M., and Bürgmann, R., 2013, Time-dependent model of creep on the Hayward fault from joint inversion of 18 years of InSAR and surface creep data: Journal of Geophysical Research: Solid Earth, v. 118, no. 4, p. 1733-1746.

Sibson, R., 1977, Fault rocks and fault mechanisms: Journal of the Geological Society, v. 133, no. 3, p. 191-213.

Sibson, R. H., 1975, Generation of pseudotachylyte by ancient seismic faulting: Geophysical Journal of the Royal Astronomical Society, v. 43, no. 3, p. 775-794.

Skarbek, R. M., Rempel, A. W., and Schmidt, D. A., 2012, Geologic heterogeneity can produce aseismic slip transients: Geophysical Research Letters, v. 39, no. 21.

Sylvester, A. G., and Smith, R. R., 1976, Tectonic transpression and basement-controlled deformation in San Andreas fault zone, Salton Trough, California: AAPG Bulletin, v. 60, no. 12, p. 2081-2102.

Tarling, M. S., and Rowe, C. D., 2016, Experimental slip distribution in lentils as an analog for scaly clay fabrics: Geology, v. 44, no. 3, p. 183-186.

Taylor, M. P., Ault, A. K., Odlum, M. L., and Newell, D. L., 2021, Shallow Rupture Propagation of Pleistocene Earthquakes Along the Hurricane Fault, UT, Revealed by Hematite (U-Th)/He Thermochronometry and Textures: Geophysical Research Letters, v. 48, no. 17, p. e2021GL094379.

Thom, C., Hansen, L., Goldsby, D., and Brodsky, E., 2022, A microphysical model of rock friction and the brittle-ductile transition controlled by dislocation glide and backstress evolution.

Tse, S. T., and Rice, J. R., 1986, Crustal earthquake instability in relation to the depth variation of frictional slip properties: Journal of Geophysical Research: Solid Earth, v. 91, no. B9, p. 9452-9472.

Utsu, T., and Ogata, Y., 1995, The centenary of the Omori formula for a decay law of aftershock activity: Journal of Physics of the Earth, v. 43, no. 1, p. 1-33.

Van den Ende, M., Chen, J., Ampuero, J.-P., and Niemeijer, A., 2018, A comparison between rate-and-state friction and microphysical models, based on numerical simulations of fault slip: Tectonophysics, v. 733, p. 273-295.

Van der Pluijm, B. A., and Marshak, S., 2004, Earth structure, W.W. Norton & Company, Inc., 656 p.:

Vannucchi, P., 2019, Scaly fabric and slip within fault zones: Geosphere, v. 15, no. 2, p. 342-356.

Vrolijk, P., and van der Pluijm, B. A., 1999, Clay gouge: Journal of Structural Geology, v. 21, no. 8-9, p. 1039-1048.

Wallace, L. M., Webb, S. C., Ito, Y., Mochizuki, K., Hino, R., Henrys, S., Schwartz, S. Y., and Sheehan, A. F., 2016, Slow slip near the trench at the Hikurangi subduction zone, New Zealand: Science, v. 352, no. 6286, p. 701-704.

Wei, M., Kaneko, Y., Liu, Y., and McGuire, J. J., 2013, Episodic fault creep events in California controlled by shallow frictional heterogeneity: Nature geoscience, v. 6, no. 7, p. 566-570.

Wernicke, R. S., and Lippolt, H. J., 1993, Botryoidal hematite from the Schwarzwald (Germany): heterogeneous uranium distributions and their bearing on the helium dating method: Earth and Planetary Science Letters, v. 114, p. 287-300.

-, 1994a, ^{4}He age discordance and release behavior of a double shell botryoidal hematite from the Schwarzwald, Germany: Geochimica et Cosmochimica Acta, v. 58, no. 1, p. 421-429.

-, 1994b, Dating of vein specularite using internal (U+Th)/^{4}He isochrons: Geophysical Research Letters, v. 21, p. 345-347.

-, 1997, (U+Th)-He evidence of Jurassic continuous hydrothermal activity in the Schwarzwald basement, Germany: Chemical Geology, v. 138, p. 273-285.

Wibberley, C. A. J., and Shimamoto, T., 2005, Earthquake slip weakening and asperities explained by thermal pressurization: Nature, v. 436, p. 689-692.

Williams, R. T., Rowe, C. D., Okamoto, K., Savage, H. M., and Eves, E., 2021, How Fault Rocks Form and Evolve in the Shallow San Andreas Fault: Geochemistry, Geophysics, Geosystems, v. 22, no. 11, p. e2021GC010092.

Wintsch, R., Christoffersen, R., and Kronenberg, A., 1995, Fluid-rock reaction weakening of fault zones: Journal of Geophysical Research: Solid Earth, v. 100, no. B7, p. 13021-13032.

Wu, L.-Y., Stuart, F. M., Di Nicola, L., Heizler, M., Benvenuti, M., and Hu, R.-Z., 2019, Multi-aliquot method for determining (U+ Th)/He ages of hydrothermal hematite: Returning to Elba: Chemical Geology, v. 504, p. 151-157.

Xing, T., Zhu, W., French, M., and Belzer, B., 2019, Stabilizing effect of high pore fluid pressure on slip behaviors of gouge-bearing faults: Journal of Geophysical Research: Solid Earth, v. 124, no. 9, p. 9526-9545.

Zuza, A. V., and Cao, W., 2020, Seismogenic thickness of California: Implications for thermal structure and seismic hazard: Tectonophysics, v. 782, p. 228426.

CHAPTER II

HEMATITE ACCOMODATES SHALLOW, TRANSIENT PLEISTOCENE SLOW SLIP IN THE EXHUMED SOUTHERN SAN ANDREAS FAULT SYSTEM

ABSTRACT

Shallow slow slip is a fundamental part of the earthquake cycle, but the processes controlling this phenomenon in space and time are poorly constrained. Hematite, common in continental fault zones, exhibits unique textures and (U-Th)/He thermochronometry data patterns reflecting different slip rates. We investigate networks of small hematite-coated slip surfaces in basement fault damage of exhumed strike-slip faults that connect to the southern San Andreas fault in a flower structure in Mecca Hills, CA. Scanning electron microscopy shows these mm-thick surfaces exhibit basal hematite injection veins and layered veinlets, comprising nanoscale, high-aspect ratio hematite plates akin to phyllosilicates. Combined microstructural and hematite (U-Th)/He data (n=64 new, 24 published individual analyses) record hematite mineralization events ~0.8 Ma to 0.4 Ma at <1.5 km depth. We suggest these faults formed via fluid overpressure, and then hematite localized repeated subseismic slip, creating zones of shallow off-fault damage up to 4 km orthogonal to the trace of the southern San Andreas fault. Distributed hematite slip surfaces develop by and then accommodate transient slow slip, potentially dampening earthquake energy in shallow continental faults.

2.1. Introduction

Exhumed fault rocks record time-integrated thermochemical and mechanical signatures of past deformation processes that currently operate at depth over repeated earthquake cycles. Minerals and slip surface textures may generate rheological contrasts that promote different slip behaviors (Collettini et al., 2009; Williams et al., 2021). In the shallow portion of continental faults, hematite is common and forms from interactions of oxidizing groundwater with Fe-rich minerals. Hematite textures and (U-Th)/He (hematite He) thermochronometry can document the timing, temperatures, depths, and/or rates of fault slip (Ault, 2020). Recent work from natural and experimental faults shows clear evidence for earthquakes (Ault et al., 2019; Calzolari et al., 2020; McDermott et al., 2017). However, other observations suggest hematite deforms subseismically (Moser et al., 2017; McDermott et al., 2021), implying hematite may accommodate a range of slip behaviors.

Faults slip is a continuum from earthquakes to aseismic slip (Jolivet and Frank, 2020). This includes seismically- and geodetically-observed low (and very low) frequency earthquakes, tremor, slow slip events, and creep events (Beroza and Ide, 2011; Peng and Gomberg, 2010; Shelly et al., 2006). Here we use slow slip as a general term for the release of elastic energy along faults at rates slow enough that radiated energy is not detected (Bürgmann, 2018; Jolivet and Frank, 2020). The mechanisms that cause slow slip are not clear but include mechanical effects of increased pore fluid pressure or heterogeneous frictional, lithologic, or geometric fault properties (French and Condit, 2019; Ikari, 2019; McCaffrey et al., 2008; Wei et al., 2013). Accurate models of slow slip, bridging

geophysical and geologic data and informing earthquake hazards, require direct observations of fault zones that experience limited overprinting deformation.

Along the southernmost segment of the San Andreas fault (SAF) system, California, a series of oblique strike-slip faults in the Mecca Hills connect to the southern SAF at depth in a positive flower structure (Fuis et al., 2017; Sylvester and Smith, 1976). Geophysical data show recent triggered and spontaneous shallow creep events along the southern SAF and other minor structures in the area (Allen et al., 1972; Lindsey et al., 2014; Parker et al., 2021; Tymofyeyeva et al., 2019). Prior work revealed hematite-coated slip surfaces in some basement fault zones in Mecca Hills (Moser et al., 2017). Limited hematite He analyses identified Pleistocene hematite mineralization events at ~1-2 km depth (Moser et al., 2017), placing these surfaces at the target depth range to evaluate if they accommodated shallow slow slip in the past. Here we expand this Mecca Hills hematite He dataset and integrate new field and microstructural results to document where, when, and how hematite fault damage forms and deforms, with implications for how deformation occurs at depth today in the southern SAF system.

2.2. Basement-hosted fault damage in the Mecca Hills

Transpression on the SAF and other related faults initiated in the Pliocene, exhumed Precambrian crystalline basement and Orocopia Schist in Mecca Hills, and formed adjacent sedimentary basins (Bergh et al., 2019; Fattaruso et al., 2014; McNabb et al., 2017; Moser et al., 2017; Spotila et al., 2020; Sylvester and Smith, 1976). Oblique strike-slip faults cut basement and Plio-Pleistocene sedimentary rock, delineating

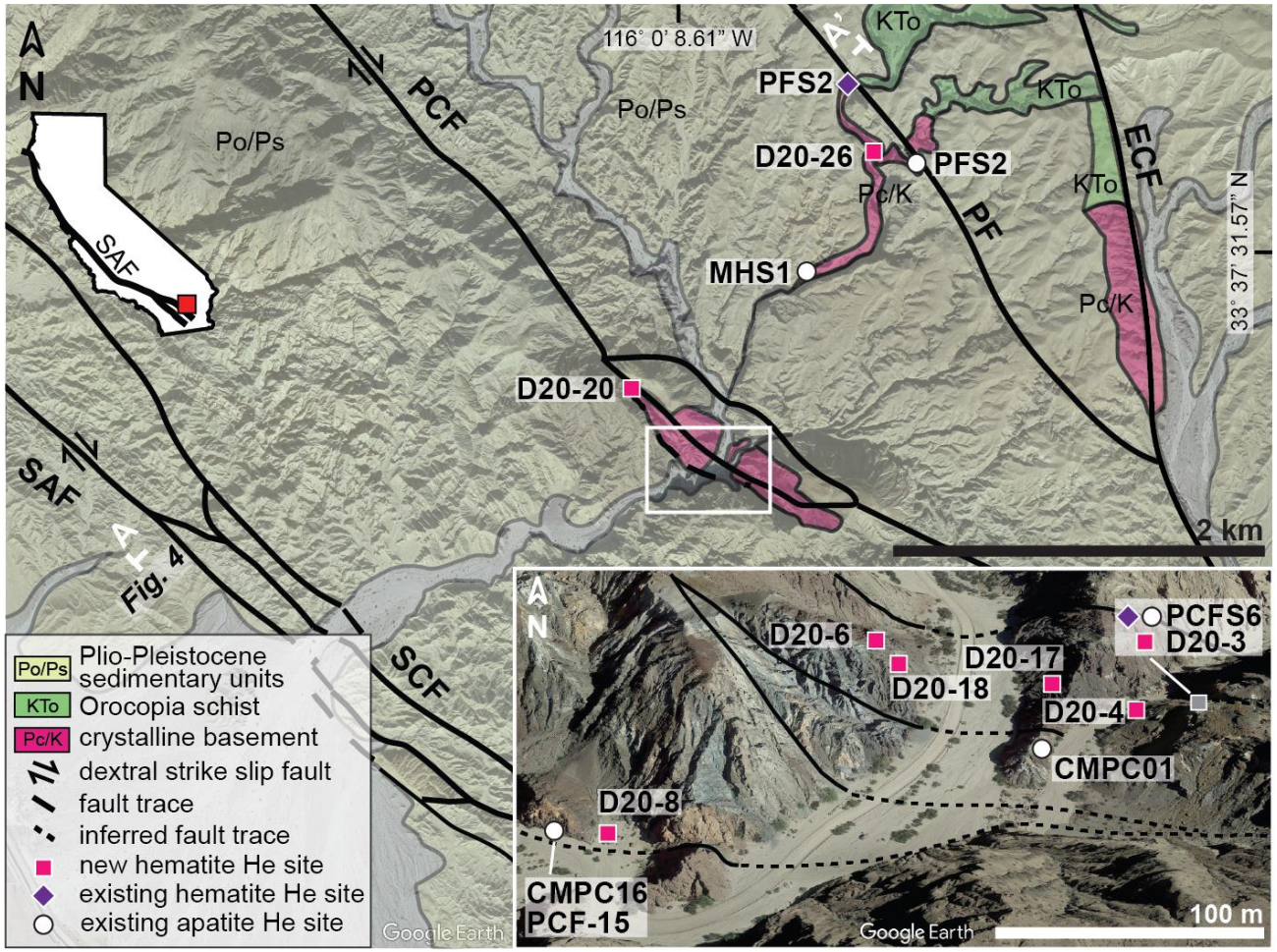

Figure 2.1. Simplified geologic map of Mecca Hills, CA, with site locations, modified from Fattaruso et al. (2014); McNabb et al. (2017); Moser et al. (2017). San Andreas (SAF), Skeleton Canyon (SCF), Painted Canyon (PCF), Platform (PF), Eagle Canyon (ECF) faults. A-A': cross-section line for figure 4A. White box denotes Google Earth inset location with site details.

separate fault blocks (Fig. 2.1; Sylvester and Smith, 1976). Incised canyons expose fault zones up to 1 km-wide, including the Painted Canyon Fault (PCF) and the Platform Fault (PF), that bound the Platform block (Sylvester and Smith, 1976). We identified a map-scale low-angle normal fault in the Platform Block that offsets different basement rock types. These faults do not deform the overlying sedimentary rock, indicating initial faulting predates deposition (Fig. A1).

Fe-oxide-coated slip surfaces are ubiquitous in basement damage zones of the PCF, PF, and within the Platform Block. Here we focus on pure hematite surfaces amenable to (U-Th)/He analysis, which occur as networks of minor (1 cm^2- to 1000 cm^2-surface area) faults cutting chlorite-rich schistose gneiss) and epidote-rich granite (Table A1; Figs. 2.1, 2.2A, A2, A3). These dominantly NNW- and NE-striking surfaces are metallic, blue-gray, curviplanar, with linear and/or curved slickenline orientations indicating oblique- and dip-slip with mm- to cm-scale offset. Newly observed hematite-clay slip surfaces occur within and adjacent to clay gouge zones of map-scale faults.

2.3. Microstructural characterization

Scanning electron microscopy (SEM) with energy dispersive X-ray spectroscopy (EDS) was used to characterize 50 μm to 2 mm-thick fault surfaces (n=10) with nanometer-scale hematite plates that appear opaque in thin section (See Supplemental Material for detailed methods; Figs. 2.2, A4). EDS data indicate some surfaces comprise interlayered and/or cross-cutting hematite veins with calcite and phyllosilicate veins (Fig. 2.2B). A subset of surfaces are cataclasite with a hematite matrix and clasts of host rock and/or reworked clasts of secondary calcite, phyllosilicate, or hematite veins (Fig. 2.2C).

Foliated hematite locally exhibits S-C fabrics, hematite-tailed clasts, and 'hematite mica-fish' (Figs. 2.2F, A5). Some surfaces display ~10 to 100 μm-wide, ~100 μm to 1 mm-long hematite-filled injection veins into host rock or calcite oriented perpendicular to the fault surface (Figs. 2.2D, A5).

Foliated, high-aspect ratio hematite platelets are planar or cuspate in cross-section with smooth or serrated grain boundaries (Figs. 2.2G, A6). Some surfaces also exhibit euhedral, hexagonal plates with equant c-axis perpendicular cross-sections (Figs. 2.2E, A6). For aliquots analyzed for thermochronometry, we quantified hematite plate-width distributions (n=1567) from SEM images, because this dimension is the minimum He diffusion domain length scale (See Supplemental Material for methods). Plate-width measurements display a left-skewed normal distribution of 12-87 nm with a mean of 31 nm (Fig. A7); plate-lengths are ~200 nm-1 μm. Observed phyllosilicates exhibit similar dimensions (Figs. A5, A6).

2.4. Hematite (U-Th)/He data

Hematite aliquots were analyzed for He, U, and Th at the Arizona Radiogenic Helium Dating Laboratory using apatite lasing temperatures (to prevent U and Th volatilization) and modified zircon dissolution procedures (see Supplemental Material for sample preparation and analytical details). We present 64 new individual hematite He dates from 17 samples on 15 fault surfaces collected from eight sites (Table A2; Figs. A3, A8) and combine these data with previously reported results in Moser et al. (2017; 24 aliquots from five surfaces) (Fig. 2.1). We report mean dates ± 1σ standard deviation for all samples because they yield <15% standard deviation, except D20-6 (26% standard

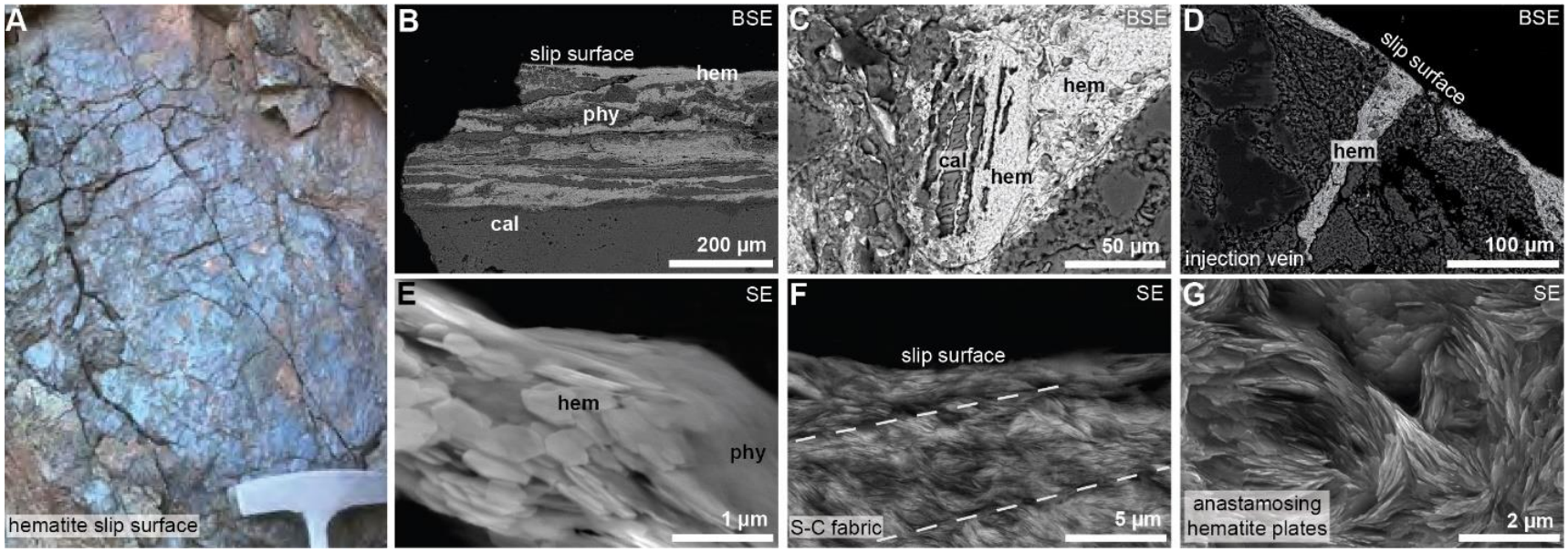

Figure 2.2. A: Hematite slip surfaces in PCF. Backscatter electron (BSE) images of (**B**) slip surface with interlayered hematite (hem), phyllosilicates (phy), calcite (cal); (**C**) reworked clast; (**D**) hematite injection vein. Secondary electron (SE) images of (**E**) euhedral hematite plates and phyllosilicates, (**F**) hematite S-C fabric, (**G**) anastomosing, high-aspect ratio hematite plates.

Deviation), where we report the range of individual aliquot dates with their 2σ analytical uncertainty(c.f. Flowers and Kelley, 2011). We do not apply an alpha (α)-ejection correction to individual dates because α-ejection from one crystal is balanced by He implantation from another in dense polycrystalline material, and aliquots are extracted from slip surfaces that developed within larger hematite veins. Consideration of α-ejection from aliquot margins would at most increase dates by 12% (see Supplemental Material). For samples with dates <1 Ma, variable [$^{234}U/^{238}U$] and [$^{230}Th/^{238}U$] activity ratios may cause <15% error on individual analyses, within the standard deviation for most samples (cf. Farley et al., 2002; see Supplemental Material).

We delineate four hematite He sample groups by structural position along a SW-NE transect: (1) W of the main PCF near a faulted basement-sedimentary rock nonconformity, (2) within the voluminous PCF zone, (3) near the low-angle normal fault in the Platform Block, and (4) near the PF (Fig. 2.3). Mean dates from samples in group (1) are 0.79 ± 0.01 Ma and 0.70 ± 0.09 Ma, (2) range from 0.71 ± 0.03 Ma to 0.38 ± 0.01 Ma, (3) are 0.42 ± 0.05 Ma and 0.36 ± 0.02 Ma, and (4) 0.63 ± 0.09 Ma (Fig. 2.3). Individual dates from site D20-6 in group 2 range from 2.2 ± 0.1 Ma to 0.99 ± 0.04 Ma.

2.5. Shallow Pleistocene hematite precipitation

Polycrystalline hematite yields a (U-Th)/He closure temperature (T_c) of ~25-250 °C (Farley et al., 2018) that is controlled by the grain size distribution. Because hematite can precipitate at temperatures above or below its T_c, we interpret the significance of our hematite He data using T_c estimates from our plate half-width distributions and ambient thermal conditions constrained by adjacent basement apatite (U-Th)/He (apatite He)

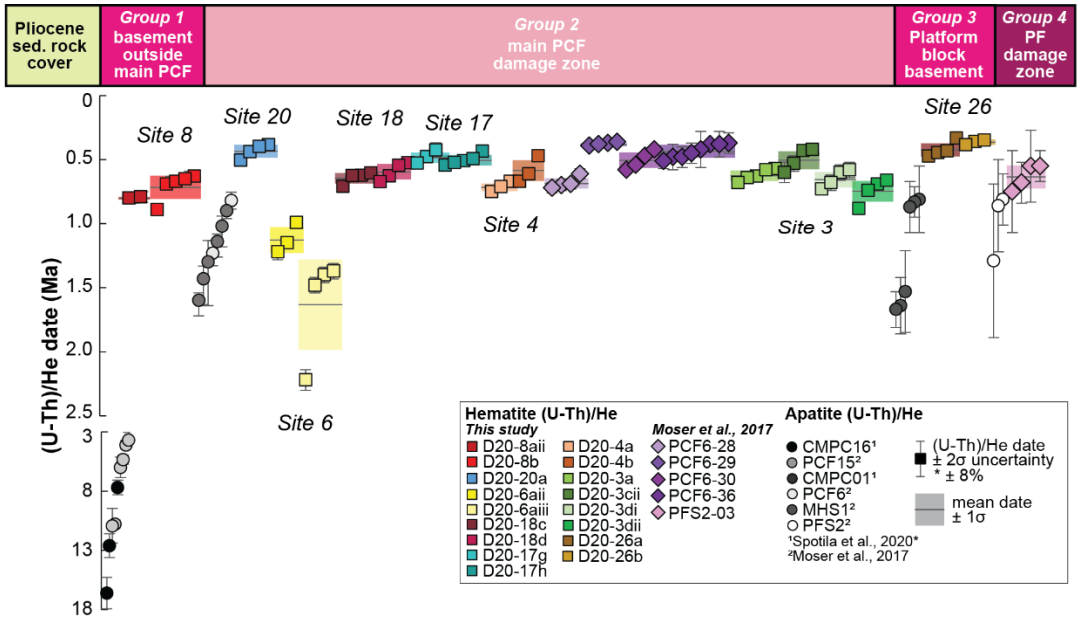

Figure 2.3. Individual hematite (U-Th)/He dates ± 2σ analytical uncertainty, x-axis is position (not to scale) along SW-NE transect. Top bar shows hematite He date group, structural context. Hematite He dates, squares (this study) and diamonds (Moser et al., 2017) with mean ± standard deviation; colored by site, shades are different samples. Apatite He dates, circles (Moser et al., 2017; Spotila et al., 2020), for each group plotted to left of hematite He dates for comparison.

thermochronometry. Assuming the diffusion kinetics of Farley (2018), a spherical geometry that yields a conservative lower T_c (compared to plane-sheet geometry), and 10 °C/My cooling rate, calculated hematite He T_c are ~60-72 °C (Fig. A7). This T_c range overlaps with the apatite He system (Flowers et al., 2009), so dates from each system may be directly compared (Fig. 2.3). Individual ~1.6-0.8 Ma apatite He dates across the Platform Block record rapid exhumation through <1.5 km at that time (Moser et al., 2017; Spotila et al., 2020). Outside the Platform Block, apatite He dates are ~18-3 Ma, implying slower and/or a lower magnitude of exhumation (Fig. 2.3).

Across our transect, most (91%) individual hematite He dates are younger than structurally adjacent apatite He dates (Fig. 2.3) despite similar calculated Tc for all hematite aliquots and between the hematite He and apatite He systems. These patterns indicate mean hematite He dates from these samples do not record ambient cooling and instead record hematite formation ~0.8 Ma to ~0.4 Ma at <1.5 km depth. Consideration of the maximum aliquot α-ejection correction factor or secular disequilibrium effects does not change these interpretations. Individual hematite He dates from site D20-6 (group 2) overlap with nearby apatite He dates; these hematite He results reflect cooling due to exhumation, with a minimum formation age of ~2.2 Ma.

We interpret mean hematite He dates record mineralization events because variation in mean dates between samples (~0.43 Ma) exceeds the maximum intrasample data scatter (~0.26 Ma). Intrasample scatter may reflect aliquots capture multiple Pleistocene hematite generations (i.e., mixed ages). Within the PCF (group 2), mean dates from different slip surfaces within a site show broadly contemporaneous hematite formation (e.g., D20-4) and distinct periods of mineralization (e.g., D20-3/PCF6; Fig.

2.3, Table A2). Group 3 hematite He dates are from minor slip surfaces in the damage zone of the low-angle fault within the Platform Block that likely pre-dates the SAF. Collectively, these data patterns support the creation and reactivation of Pleistocene hematite fault damage in larger structures linked to or not associated with the SAF.

2.6. Repeated slow slip on hematite slip surfaces

We suggest injection veins at the base of some slip surfaces reflect initial hematite precipitation during transient fluid overpressure events. Along other slip surfaces, fluid-rock interactions, including with lower permeability clay minerals, mobilized Fe and precipitated hematite along precursor grain interfaces and in veins. Interlayered and crosscutting hematite and calcite veins, as well as clasts of older hematite veins, indicate repeated and episodic hematite precipitation on individual slip surfaces. Hematite textures, such as S-C fabrics, demonstrate on-going slip occurred on these surfaces following hematite growth (Fig. 2.2).

Hematite grain morphologies along slip surfaces are distinct from polygonal or sintered grains associated with coseismic friction-generated heat (Ault et al., 2019; Calzolari et al., 2020), or comminuted and recrystallized particles formed during propagation of seismic slip at shallow depths at other locations (Taylor et al., 2021). Our observed hematite plates have a similar aspect ratio to phyllosilicate sheets. The platy structure and crystal-bound water in phyllosilicates contribute to a low coefficient of friction and velocity-strengthening behavior that promote stable sliding (Collettini et al., 2009; French et al., 2015; Moore and Lockner, 2004). Phyllosilicate-rich rocks produce transient slow slip events in the lab (Ikari, 2019). Although hematite does not contain

crystal bound water, available data reveal its coefficient of friction (0.28 ± 0.12; Calzolari et al., 2020) may be comparable to phyllosilicates, suggesting similar frictional behavior.

Preserved plates, homogenous grain size distributions, and foliated textures (Fig. 2.2) show hematite did not experience post-formation comminution and instead deformed by interplate sliding. Reproducible intrasample hematite He dates record hematite growth and indicate that repeated reactivation of these surfaces occurred at slip rates slow enough to not induce He loss from hematite. These observations imply hematite formed and continued to deform by slow slip.

2.7. Geologic controls on shallow transient slow slip

Hematite He thermochronometry lacks the temporal resolution to characterize the time scale(s) of a slow slip (or earthquake) cycle. However, when integrated with microstructures, these data bracket episodes of past fault damage creation and inform transient aseismic slip processes, such as slow slip events, occurring at depth today along shallow continental faults including the SAF. In the Mecca Hills, we interpret networks of small hematite slip surfaces, each with mm of cumulative offset, in damage zones of the PCF, PF, and structures within the Platform Block develop by repeated, *transient* slow slip at <1.5 km depth from ~0.8 Ma to 0.4 Ma. Transient slow slip is subsequently localized on these surfaces, even after ~0.4 Ma. Hematite fault damage is preserved up to 4 km perpendicular to the main trace of the southern SAF, revealing the spatial scales of past transient slow slip in off-fault damage of the SAF system (Fig. 2.4A).

Development of hematite fault damage influences shallow fault rheology that may contribute to slow slip at depth in the southern SAF system (Fig. 2.4) and other

continental faults worldwide (e.g. Calzolari et al., 2018; McDermott et al., 2021). We suggest that hematite damage initially forms by pore fluid overpressure and fluid-rock interaction reflecting transient slow slip (Fig. 4B). Once formed, slip surface networks of anisotropic, foliated hematite (Fig. 4B), which is weaker than the surrounding basement rock, continue to deform by transient slow slip. Observations from the shallow rock record reveal hematite, like phyllosilicates, may play a role in accommodating the aseismic propagation of transient or triggered slow slip, potentially facilitating arrest of earthquakes in the shallowest crust.

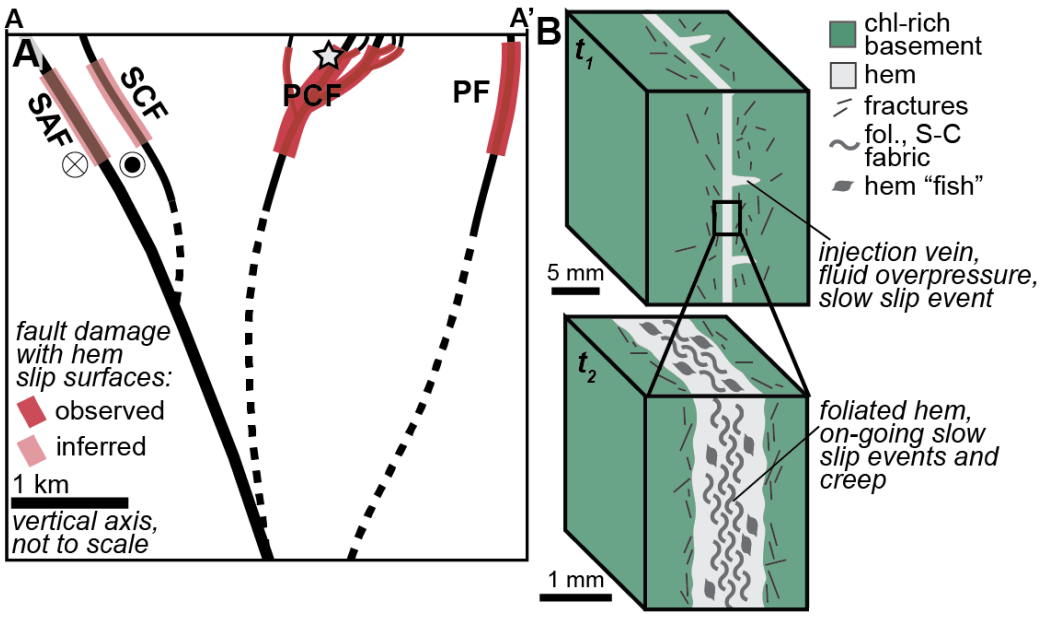

Figure 2.4. A: Schematic A-A' cross section of the southern SAF system through Mecca Hills, with location of hematite fault damage in red. Star is example location of B. **B:** Simplified block diagrams show textural evolution of an individual hematite surface with initial precipitation (t_1) and repeated slow slip on same surface (t_2).

REFERENCES

Allen, C. R., Wyss, M., Brune, J. N., Grantz, A., and Wallace, R. E., 1972, Displacements on the Imperial, Superstition Hills, and San Andreas faults triggered by the Borrego Mountain earthquake: US Geol. Surv. Prof. Pap, v. 787, p. 87-104.

Ault, A. K., 2020, Hematite fault rock thermochronometry and textures inform fault zone processes: Journal of Structural Geology, p. 104002.

Ault, A. K., Jensen, J. L., McDermott, R. G., Shen, F.-A., and Van Devener, B. R., 2019, Nanoscale evidence for temperature-induced transient rheology and postseismic fault healing: Geology.

Bergh, S. G., Sylvester, A. G., Damte, A., and Indrevær, K., 2019, Polyphase kinematic history of transpression along the Mecca Hills segment of the San Andreas fault, southern California: Geosphere, v. 15, no. 3, p. 901-934.

Beroza, G. C., and Ide, S., 2011, Slow earthquakes and nonvolcanic tremor: Annual review of Earth and planetary sciences, v. 39, p. 271-296.

Bürgmann, R., 2018, The geophysics, geology and mechanics of slow fault slip: Earth and Planetary Science Letters, v. 495, p. 112-134.

Calzolari, G., Ault, A. K., Hirth, G., and McDermott, R. G., 2020, Hematite (U-Th)/He thermochronometry detects asperity flash heating during laboratory earthquakes: Geology.

Calzolari, G., Rossetti, F., Ault, A. K., Lucci, F., Olivetti, V., and Nozaem, R., 2018, Hematite (U-Th)/He thermochronometry constrains strike-slip faulting on the Kuh-e-Faghan fault, central Iran: Tectonophysics, v. 728-729, p. 41-54.

Collettini, C., Niemeijer, A., Viti, C., and Marone, C., 2009, Fault zone fabric and fault weakness: Nature, v. 462, no. 7275, p. 907-910.

Farley, K., Kohn, B., and Pillans, B., 2002, The effects of secular disequilibrium on (U–Th)/He systematics and dating of Quaternary volcanic zircon and apatite: Earth and Planetary Science Letters, v. 201, no. 1, p. 117-125.

Farley, K. A., 2018, Helium diffusion parameters of hematite from a single-diffusion-domain crystal: Geochimica et Cosmochimica Acta, v. 231, p. 117-129.

Fattaruso, L. A., Cooke, M. L., and Dorsey, R. J., 2014, Sensitivity of uplift patterns to dip of the San Andreas fault in the Coachella Valley, California: Geosphere, v. 10, no. 6, p. 1235-1246.

Flowers, R. M., and Kelley, S. A., 2011, Interpreting data dispersion and "inverted" dates in apatite (U-Th)/He and fission track datasets: An example from the U.S. midcontinent: Geochimica et Cosmochimica Acta, v. 75, p. 5169-5186.

Flowers, R. M., Ketcham, R. A., Shuster, D. L., and Farley, K. A., 2009, Apatite (U-Th)/He thermochronometry using a radiation damage accumulation and annealing model: Geochimica et Cosmochimica Acta, v. 73, p. 2347-2365.

French, M., Chester, F., and Chester, J., 2015, Micromechanisms of creep in clay-rich gouge from the Central Deforming Zone of the San Andreas Fault: Journal of Geophysical Research: Solid Earth, v. 120, no. 2, p. 827-849.

French, M. E., and Condit, C. B., 2019, Slip partitioning along an idealized subduction plate boundary at deep slow slip conditions: Earth and Planetary Science Letters, v. 528, p. 115828.

Fuis, G. S., Bauer, K., Goldman, M. R., Ryberg, T., Langenheim, V. E., Scheirer, D. S., Rymer, M. J., Stock, J. M., Hole, J. A., and Catchings, R. D., 2017, Subsurface geometry of the San Andreas fault in southern California: Results from the Salton Seismic Imaging Project (SSIP) and strong ground motion expectations: Bulletin of the Seismological Society of America, v. 107, no. 4, p. 1642-1662.

Ikari, M. J., 2019, Laboratory slow slip events in natural geological materials: Geophysical Journal International, v. 218, no. 1, p. 354-387.

Jolivet, R., and Frank, W., 2020, The transient and intermittent nature of slow slip: AGU Advances, v. 1, no. 1, p. e2019AV000126.

Lindsey, E. O., Fialko, Y., Bock, Y., Sandwell, D. T., and Bilham, R., 2014, Localized and distributed creep along the southern San Andreas Fault: Journal of Geophysical Research: Solid Earth, v. 119, no. 10, p. 7909-7922.

McCaffrey, R., Wallace, L. M., and Beavan, J., 2008, Slow slip and frictional transition at low temperature at the Hikurangi subduction zone: Nature Geoscience, v. 1, no. 5, p. 316-320.

McDermott, R. G., Ault, A. K., and Caine, J. S., 2021, Dating fault damage along the eastern Denali fault zone with hematite (U-Th)/He thermochronometry: Earth and Planetary Science Letters, v. 563, p. 116872.

McDermott, R. G., Ault, A. K., Evans, J. P., and Reiners, P. W., 2017, Thermochronometric and textural evidence for seismicity via asperity flash heating on exhumed hematite fault mirrors, Wasatch fault zone, UT, USA: Earth and Planetary Science Letters, v. 471, p. 85-93.

McNabb, J. C., Dorsey, R. J., Housen, B. A., Dimitroff, C. W., and Messé, G. T., 2017, Stratigraphic record of Pliocene-Pleistocene basin evolution and deformation within the southern San Andreas fault zone, Mecca Hills, California: Tectonophysics, v. 719, p. 66-85.

Moore, D. E., and Lockner, D. A., 2004, Crystallographic controls on the frictional behavior of dry and water-saturated sheet structure minerals: Journal of Geophysical Research: Solid Earth, v. 109, no. B3.

Moser, A. C., Evans, J. P., Ault, A. K., Janecke, S. U., and Bradbury, K. K., 2017, (U-Th)/He thermochronometry reveals Pleistocene punctuated deformation and synkinematic hematite mineralization in the Mecca Hills, southernmost San Andreas Fault zone: Earth and Planetary Science Letters, v. 476, p. 87-99.

Parker, J., Donnellan, A., Bilham, R., Ludwig, L. G., Wang, J., Pierce, M., Mowery, N., and Jänecke, S., 2021, Buried aseismic slip and off-fault deformation on the southernmost San Andreas fault triggered by the 2010 El Mayor Cucapah earthquake revealed by UAVSAR: Earth and Space Science, v. 8, no. 8, p. e2021EA001682.

Peng, Z., and Gomberg, J., 2010, An integrated perspective of the continuum between earthquakes and slow-slip phenomena: Nature geoscience, v. 3, no. 9, p. 599-607.

Shelly, D. R., Beroza, G. C., Ide, S., and Nakamula, S., 2006, Low-frequency earthquakes in Shikoku, Japan, and their relationship to episodic tremor and slip: Nature, v. 442, no. 7099, p. 188-191.

Spotila, J. A., Mason, C. C., Valentino, J. D., and Cochran, W. J., 2020, Constraints on rock uplift in the eastern Transverse Ranges and northern Peninsular Ranges and

implications for kinematics of the San Andreas fault in the Coachella Valley, California, USA: Geosphere.

Sylvester, A. G., and Smith, R. R., 1976, Tectonic transpression and basement-controlled deformation in San Andreas fault zone, Salton Trough, California: AAPG Bulletin, v. 60, no. 12, p. 2081-2102.

Taylor, M. P., Ault, A. K., Odlum, M. L., and Newell, D. L., 2021, Shallow Rupture Propagation of Pleistocene Earthquakes Along the Hurricane Fault, UT, Revealed by Hematite (U-Th)/He Thermochronometry and Textures: Geophysical Research Letters, v. 48, no. 17, p. e2021GL094379.

Tymofyeyeva, E., Fialko, Y., Jiang, J., Xu, X., Sandwell, D., Bilham, R., Rockwell, T. K., Blanton, C., Burkett, F., and Gontz, A., 2019, Slow Slip Event On the Southern San Andreas Fault Triggered by the 2017 M w 8.2 Chiapas (Mexico) Earthquake: Journal of Geophysical Research: Solid Earth, v. 124, no. 9, p. 9956-9975.

Wei, M., Kaneko, Y., Liu, Y., and McGuire, J. J., 2013, Episodic fault creep events in California controlled by shallow frictional heterogeneity: Nature geoscience, v. 6, no. 7, p. 566-570.

Williams, R. T., Rowe, C. D., Okamoto, K., Savage, H. M., and Eves, E., 2021, How Fault Rocks Form and Evolve in the Shallow San Andreas Fault: Geochemistry, Geophysics, Geosystems, v. 22, no. 11, p. e2021GC010092.

CHAPTER III

HEMATITE FRICTIONAL BEHAVIOR AND HE LOSS DURING DEFORMATION EXPERIMENTS AT SLOW RATES

ABSTRACT

Friction deformation experiments on hematite, common in fault zones, characterize its slip-rate dependent frictional properties and deformation mechanisms, and frictional behavior informs observations from natural, exhumed hematite-coated faults and present-day deformation at depth. We conducted single-velocity and velocity-step experiments on hematite slabbed from a specularite boulder using an Instron rotary-shear apparatus at slip rates of 0.85 μm/s to 320 mm/s over displacements up to 45 cm at normal stresses of 5 and 8.5 MPa. The coefficient of friction for hematite ranges from ~0.25 to 0.45, and velocity-step experiments indicate hematite displays primarily velocity-strengthening and velocity-neutral behavior at rates <1 mm/s. Scanning electron microscopy reveals experimentally generated faults localize in a thin layer of hematite gouge. Angular gouge particles have an average diameter of ~0.69 um, indicating grain size reduction generates a 7200% increase in surface area. Hematite is amenable to thermochronometry and application of this tool to experiments can quantify fault-related thermal and mechanical processes. Comparison of hematite (U-Th)/He dates from undeformed specularite and gouge indicates He loss occurs during comminution along newly-generated gouge particle surfaces without an associated temperature rise required for volume diffusion. These results imply natural hematite faults accommodate stable slip

and that hematite (U-Th)/He dates acquired from ultracataclasite or gouge may reflect minor He loss unrelated to thermal processes.

3.1. Introduction

Faults slip over a range of rates at different depths. Some faults experience aseismic creep, or continuous slip at plate-rates along the shallow portion of a fault between earthquakes (Harris, 2017). Geodesy reveals transient increases in slip rate at subseismic rates above background creep rates updip of the seismogenic zone, referred to as shallow slow slip (Bürgmann, 2018; Jolivet and Frank, 2020; Wei et al., 2013). Slow slip occurs throughout the earthquake cycle, and integrated observations from geodesy, exhumed faults, and laboratory experiments inform the in-situ mechanisms operative where slow slip occurs today. The mechanisms suggested to promote slow slip at various depths include heterogeneous frictional behavior reflecting mineralogical contrasts (Fagereng and Beall, 2021; French and Condit, 2019; Skarbek et al., 2012; Wei et al., 2013), elevated pore fluid pressure that reduces effective stress (Saffer and Wallace, 2015) and increases dilatancy (Rudnicki and Chen, 1988; Xing et al., 2019), and geometric complexities that influence the stress state (Romanet et al., 2018).

Shallow, brittle fault behavior is controlled by fault friction that is often modeled using empirical rate-and-state friction laws (Beeler et al., 1994; Dieterich, 1979; Linker and Dieterich, 1992; Ruina, 1983). Rate-and-state parameters are derived from laboratory experiments that shear gouge or ground blocks at an applied rate and normal stress. The coefficient of friction (μ) is calculated at various velocities by velocity-step experiments that are utilized to evaluate the influence the rate on friction in different materials.

Materials or minerals that strengthen with increasing rate are velocity-strengthening and promote stable slip (Marone, 1998). For example, phyllosilicates are weak and often display velocity-strengthening behavior that is thought to explain shallow creep (Behnsen and Faulkner, 2012; Carpenter et al., 2015; Moore and Lockner, 2004; Sánchez-Roa et al., 2017). Materials that weaken with increasing rate are velocity-weakening and promote unstable or conditionally stable fault behavior, which depends on the critical stiffness, or the ratio of stiffness of the fault and its surroundings (or the experimental loading system) (Leeman et al., 2018; Marone, 1998; Scholz, 2019). Fault healing, or the recovery of strength between earthquakes, is evaluated with slide-hold-slide tests that include intermittent holds at 0 m/s between velocities (Marone, 1997). Laboratory slow slip events indicate transitional frictional behavior (a-b ~ 0) at critical stiffness ratios near or >1 (Ikari, 2019; Leeman et al., 2018). Because friction reflects mineralogy and fault composition evolves as faults mature, investigating the frictional behavior of minerals that form within fault zones provides insight to fault mechanics (e.g., Janecke and Evans, 1988; Williams et al., 2021; Wintsch et al., 1995).

Iron (Fe) is the fourth-most common element in the Earth, and hematite is a secondary mineral that precipitates from Fe-rich fluids flowing or diffusing through shallow fractures or fault zones or from alteration of Fe-bearing host rock (Allegre et al., 1995; Ault, 2020; Cornell and Schwertmann, 2003). Hematite from exhumed faults shows textures that reflect fault slip rates (Ault, 2020). Coseismic friction-generated heat at asperities may recrystallize hematite to form polygonal or sintered grains on fault mirrors (Ault et al., 2019; McDermott et al., 2017). Hematite cataclasite reflects slip-induced grain-size reduction (McDermott et al., 2017). In contrast, preserved nanometer-

scale, high-aspect ratio hematite plates suggest slip at subseismic rates (DiMonte et al., in review; McDermott et al., 2017). Hematite is amenable to (U-Th)/He (hematite He) thermochronometry, and hematite He data patterns may reflect mineralization, exhumation, hydrothermal fluid circulation, or coseismic slip (Ault, 2020). Accurate interpretation of hematite He data requires integration with other low temperature thermochronometers, characterization of textures and grain size, and analysis of inter- and intra-sample patterns (Ault, 2020). “Thermally-reset” dates reflect He loss due to high coseismic temperatures, but it is unknown if mechanical deformation (i.e., comminution) during fault slip also induces He loss.

Prior work characterized frictional properties and He loss from hematite deformed by slide-hold-slide (or ‘interrupted slip’) and ‘continuous slip’ rotary-shear experiments conducted at rates of ~320 mm/s, displacement of 1.5 m, and normal stress of 8.5 MPa (Calzolari et al., 2020). Hematite displays a low value of μ of 0.28 ± 0.12 over rates of 0.01 to 320 mm/s and dynamic weakening was observed at rates of 320 mm/s, although machine challenges introduced some data error (Calzolari et al., 2020). Experimental fault surfaces have thin layers of gouge with localized fault mirrors comprising sintered nanoparticles (Calzolari et al., 2020). Gouge and fault mirrors yield ~13 to 71% He loss, respectively, interpreted to reflect thermally-activated volume diffusion during coseismic friction-generated heat (Calzolari et al., 2020). These hematite textures and He loss are comparable to natural fault mirrors that experienced coseismic temperature rise (Calzolari et al., 2020; McDermott et al., 2017).

Here we conduct deformation experiments using the same rotary shear apparatus and starting material as Calzolari et al. (2020), but at slip rates below 1 mm/s to

characterize hematite friction behavior and grain morphologies during slow slip. We analyze experimental faults developed within specular hematite deformed at subseismic rates using mechanical data, (U-Th)/He thermochronometry, and SEM textural observations to evaluate hematite rate-and-state friction, textures, and He loss during slow slip.

3.2. Methods

3.2.1 Sample

We utilized the same specular hematite boulder, collected from the central Wellsville Mountains, Utah, as Calzolari et al. (2020) for deformation experiments. The boulder was sawed into ~0.5-1.5 cm slabs with a water-cooled rock saw, epoxied to aluminum plates, and dried at room temperature for 24 hrs. The surface was gently ground in water to even and level it, sonicated for 20 minutes, dried in an oven at ~100 °C for <20 hrs (time and temperatures low enough *not* to induce He loss), and roughened using wet sandpaper prior to conducting experiments.

3.2.2 Rotary shear experiments

Deformation experiments were conducted using the Instron rotary-shear apparatus at Brown University's Rock Deformation Laboratory (Calzolari et al., 2020; Goldsby and Tullis, 2011; Kohli et al., 2011) at ambient room temperature and humidity (Table 3.1). Lower plates of slabbed specular hematite were deformed by rotating cylindrical ring-shaped upper annuli comprising material that varied between experiments (Fig. 3.1A). We used Frederick diabase (experiment IDs: Test001, Mock, Setup1, Setup2, PV1, PHe01, PHe02, PHe04, PHe05, PH06), Westerley granite (experiment IDs: Plan 1, Plan

2), and SiC (experiment ID: PHe03). These materials were cored to create rings with a ~54.1 mm outer diameter and ~44.2 mm inner diameter. Experiments were conducted at loads of 5 (PV1 only) and 8.5 MPa with rates ranging from 0.85 μm/s to ~320 mm/s up to a maximum of ~45 cm of displacement (Table 3.1). Velocity-step tests were conducted on a subset of experiments (Mock, Plan1, Plan2, Setup1, Setup2, PV1) to inform velocity-dependent frictional properties. Velocity step-tests began with slip at 0.85-1 μm/s until steady-state friction was observed. After initial slip, the controlled sliding velocity was stepped up to a new velocity and experiments were conducted by varying the velocity on the same sample (Fig. 3.1B). Data was acquired at 20-1000 Hz sampling rates. Single-velocity runs (Test001, PHe01-06) inform steady-state friction and run products were analyzed with (U-Th)/He thermochronometry to investigate He loss at slow slip velocities. We note that the upper annulus cracked during some experiments, implying the applied normal stress and shear stresses were not constant during these runs. Experiments conducted at higher slip rates (Test001, PHe06) resulted in some movement of the upper load cell with the lower plate, suggesting the observed velocity was lower than expected.

3.2.3 Scanning Electron Microscopy

Secondary electron (SE) and back-scattered electron (BSE) images were acquired using a FEI Quanta FEG 650 scanning electron microscope (SEM) at Utah State University's Microscopy Core Facility to identify microscale textures and to image grains for grain size measurements necessary for interpretation of hematite (U-Th)/He dates. SEM mounts were created by cutting small ~3 mm blocks parallel to the slip surface with

Table 3.1. Applied parameters of friction experiments.

Name	Type	Velocity (range)	Displacement (cm)	Annulus	Load (MPa)
Test001	single-velocity	1 mm/s	~45	diabase	8.5
Mock	velocity-step	1-10 mm/s	~45	diabase	8.5
Plan1, Plan2	velocity-step	1-500 μm/s	~13, ~26	granite	8.5
Setup1, Setup2	velocity-step	10 μm/s-1 mm/s	~10, ~13	diabase	8.5
PV1	velocity-step	1-100 μm/s	~13.5	diabase	5
PHe01	single-velocity	1 mm/s	1	diabase	8.5
PHe02	single-velocity	1 mm/s	3	diabase	8.5
PHe03	single-velocity	1 cm/s	150	SiC	8.5
PHe04	single-velocity	.858 μm/s	1	diabase	8.5
PHe05	single-velocity	.858 μm/s	3	diabase	8.5
PHe06	single-velocity	.32 m/s	3	diabase	8.5

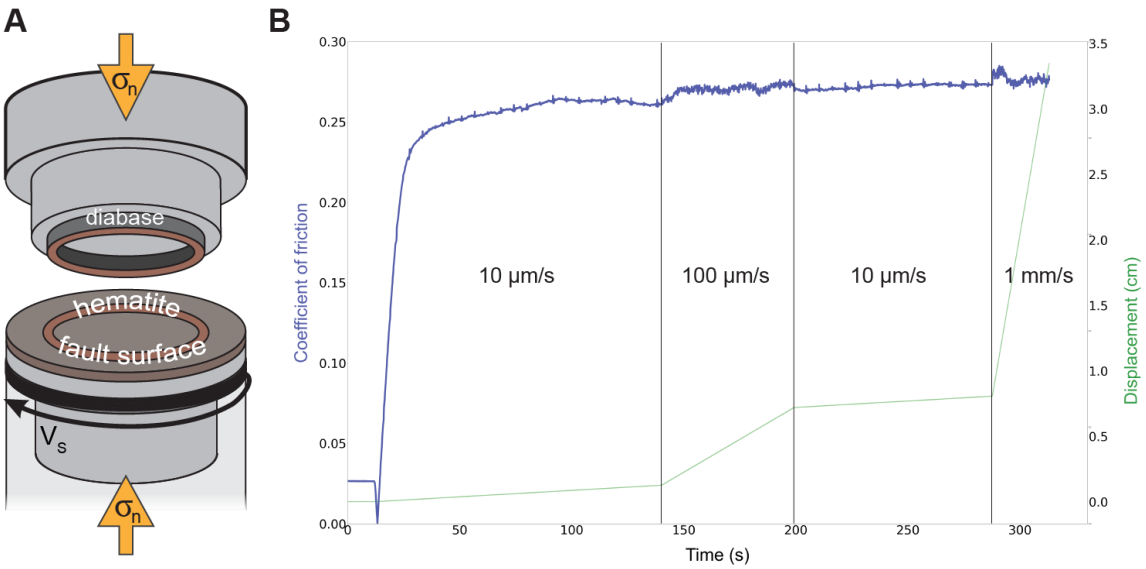

Figure 3.1. A: Schematic of rotary shear (modified from Calzolari et al., 2020). **B:** Example of a velocity-step test (initial three steps of Setup1) showing velocity-steps leading to a change in the coefficient of friction.

using a water-cooled saw. Fault surfaces were epoxied following experiments to preserve textures and cross-sectional and a few plan-view sample blocks were affixed to ½" and 1" metal posts with double-sided Cu-tape. Mounts were imaged in low vacuum mode at pressures of 0.15-0.53 torr at 100-100,000x magnifying power. The software ImageJ was utilized to measure diameters of gouge particles and plate-widths of undeformed or preserved plates (with radius of spherical particles and plate half-width representing the diffusion domain size) from images acquired at 1,000-100,000x magnifying power.

3.2.4 Hematite (U-Th)/He thermochronometry

Aliquots were analyzed for He, U, and Th at the University of Arizona's Radiogenic Helium Dating Laboratory following procedures outlined in Reiners et al. (2014). We do not apply an alpha-ejection correction to our hematite He dates because polycrystalline aliquots were selected from a larger volume of pure hematite. Thus, alpha-ejection from any given hematite plate is balanced by alpha-implantation from surrounding plates. We sampled hematite gouge from the experimentally-generated slip surfaces, which were localized between pure hematite slabs and an upper annulus observed to be coated with gouge post-experiment. Material for initial (undeformed) hematite He analysis from each slab was acquired from the same slab, but at the edge away from the deformed specularite. Because prior work revealed a positive relationship between plate-width of individual plates and hematite He date (Calzolari et al., 2020), we crushed starting material using a mortar and pestle with ethanol to obtain a more

homogenous grain size using the approach of Calzolari et al. (2020) to reduce the effect of grain size on He date.

We acquired four homogenized undeformed hematite He dates from each of the seven plates. Hematite He dates were also acquired from slip surfaces deformed at a uniform velocity (PHe1-Phe6) and from once surface (PV1) deformed in a velocity-step test. Gouge material from experiments was extracted from the slip surface using a spatula and distributed into aliquots. The number of aliquots was limited for each sample by the amount of gouge produced during the experiment. Varying amounts of underlying undeformed platy material were incorporated into the aliquots. Material was dry pipetted into Nb tubes that were closed at both ends to prevent loss of powder.

3.3. Results

3.3.1. Friction data

The steady-state coefficient of friction (μ_{ss}), calculated at velocities of 0.85 μm/s to 320 mm/s, ranges from 0.18 to 0.45, with an average of 0.35 (Table 3.2, Fig. 3.2). Reported values were estimated from individual velocity steps in the velocity-step experiments (Mock, Plan1, Plan2, Setup1, Setup2, PV1) and from single-velocity experiments (Phe01-6 and Test001). Some experimental error is expected for these data due to movement of the upper load cell and cracking of the upper annulus.

Single-velocity tests

Phe01 displays an initial rapid increase in μ and then a drop to μ_{ss} (avg. = 0.18), which then continues to increase with sliding distance (Fig. B1). Phe02 shows an initial μ

increase, followed by rising μ_{ss} (avg. = 0.41) with sliding distance (Fig. B2). Phe04 yields increasing μ_{ss} (avg. = 0.4) with sliding distance (Fig. B4). Phe05 exhibits a sharp increase in μ and then decreasing μ_{ss} (avg. = 0.4) with time (Fig. B5). Phe06 was conducted over a short time interval (0.09 s), over which μ_{ss} (0.3) was estimated (Fig. B6). Phe03 and Test001 are cyclical experiments where the rotating annulus reverses direction every 80° (~3.4 cm). Phe03 yields increasing μ_{ss} (avg. = 0.4, Fig. B3) but Test001 shows a decreasing μ_{ss} (avg. = 0.37, Fig. B7) over the course of each experiment.

Velocity-step tests

Rate-state frictional behavior of hematite is derived from velocity-step tests, including two velocity steps from Mock (Fig. B8), one step from Plan1 (Fig. B9), two steps from Plan2 (Fig. B10), seven steps from Setup1 (Figs. 3.1B, B11) five steps from Setup2 (Fig. B12), and seven steps from PV1 (Fig. B13). Values of the rate-state frictional parameter *a-b* for velocities steps were calculated using Equation 3.1 (Beeler et al., 1994) using estimates of the initial and final steady-state coefficient of friction from the average of the oscillations in μ_{ss} for velocities that were applied (Table 3.3, Fig. 3.3).

$$a\text{-}b = \frac{d(\mu_{ss})}{d(\ln V)}$$

(Equation 3.1)

Calculations of a-b reveal hematite exhibits primarily velocity strengthening to velocity neutral behavior at slow slip rates (Figure 3.3). For example, experiment Mock yields

Table 3.2. Average calculated values of μ_{ss} at imposed velocity for velocity-step (left) and single velocity (right, italics) experiments.

Name	σ_n (Mpa)	Velocity (μm/s)	Average μ_{ss}
Mock_1	8.5	50	0.41
Mock_2	8.5	1000	0.41
Mock_3	8.5	3	0.4
Mock_4	8.5	30	0.41
Plan1_1	8.5	0.85	0.35
Plan1_2	8.5	50	0.36
Plan2_1	8.5	4.3	0.42
Plan2_2	8.5	50	0.41
Plan2_3	8.5	500	0.41
Setup1_1	8.5	10	0.26
Setup1_2	8.5	100	0.27
Setup1_3	8.5	10	0.27
Setup1_4	8.5	1000	0.28
Setup1_5	8.5	10	0.26
Setup1_6	8.5	1000	0.27
Setup1_7	8.5	10	0.24
Setup1_8	8.5	50	0.25
Setup1_9	8.5	100	0.26
Setup1_10	8.5	500	0.26
Setup2_1	8.5	10	0.25
Setup2_2	8.5	0.85	0.26
Setup2_3	8.5	1000	0.26
Setup2_4	8.5	5	0.22
Setup2_5	8.5	500	0.26
Setup2_6	8.5	50	0.25
Setup2_7	8.5	500	0.26
PV1_1	5	10	0.43
PV1_2	5	100	0.41
PV1_3	5	1000	0.42
PV1_4	5	100	0.44
PV1_5	5	10	0.43
PV1_6	5	100	0.44
PV1_7	5	10	0.45
PV1_8	5	500	0.45
PV1_9	5	10	0.44
PV1_10	5	50	0.43
PV1_11	5	500	0.44

Name	σ_n (Mpa)	Velocity (μm/s)	Average μ_{ss}
Phe01	8.5	1000	0.18
Phe02	8.5	1000	0.41
Phe03	8.5	10000	0.4
Phe04	8.5	0.85	0.4
Phe05	8.5	0.85	0.4
Phe06	8.5	320000	0.3

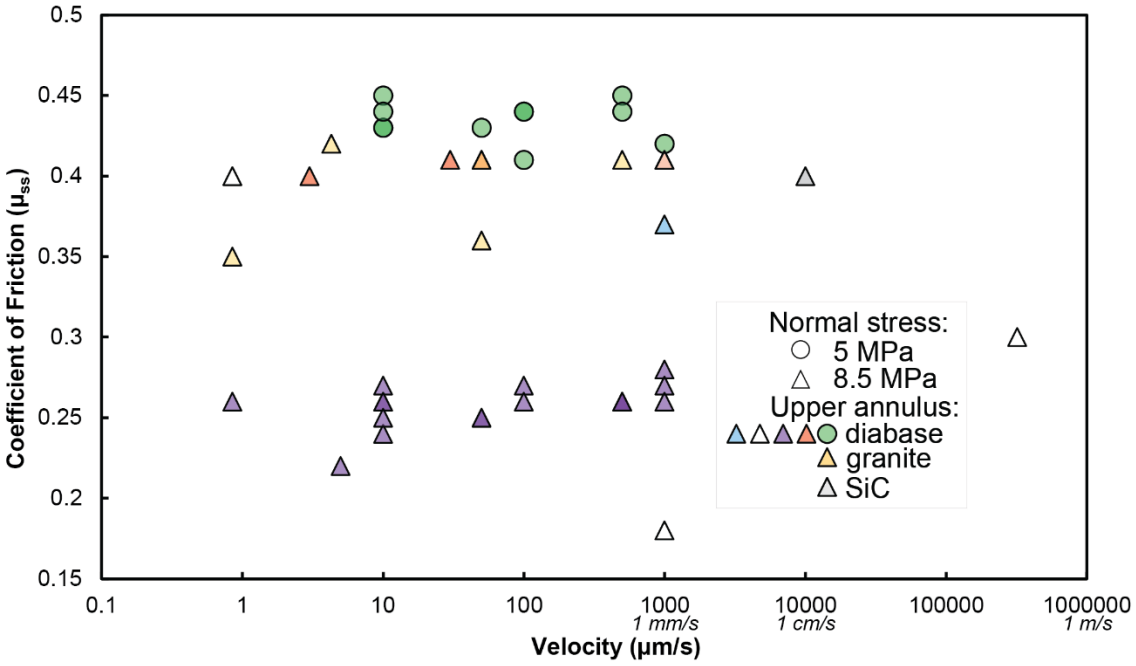

Figure 3.2. Steady-state coefficient of friction (μ) of hematite for experiments at velocities of 1 μm/s to 320 mm/s (darker shaded symbols display overlapping data points). μ ranges from 0.18 to 0.45, with an average of 0.35.

velocity-strengthening behavior in both positive velocity-steps (a-b = 0.0010 and 0.0039). Plan1 shows velocity-strengthening behavior in a positive velocity-step (a-b = 0.0012). Plan2 exhibits velocity-strengthening behavior during one positive step (a-b = 0.0013), but stronger velocity-weakening behavior (more negative a-b) during another positive step (a-b = -0.0053). Setup1 has five velocity-steps with velocity-strengthening frictional behavior (first three, a-b ranges 0.0009 to 0.0074; Fig. 3.1B), followed by velocity-weakening in the final two steps with magnitudes similar to the previous five (a-b = -0.0014 and -0.0012. Setup2 has an initial velocity-weakening step (a-b = -0.0008) followed by four velocity-strengthening steps (a-b ranges 0.0004 to 0.0087). PV1 yields two velocity-weakening (a-b = -0.0030 and -0.0006) and five velocity-strengthening steps (a-b ranges 0.0015 to 0.0100).

Most experiments show values of a–b ~ 0, implying velocity-neutral behavior. Importantly, there is no relationship between the magnitude of the velocity step (nor final velocity) and a-b in any of the experiments. Additionally, the results do not show a definitive relationship between the coefficient of friction or a-b and gouge thickness or accumulated displacement.

3.3.2. Scanning Electron Microscopy

SEM reveals the starting material comprises undeformed hematite plates with thicknesses consistent with (Calzolari et al., 2020) (Figure 3.4A). Slow slip deformation experiments formed variable amounts of gouge and the slip surfaces of the plates exhibit slickenlines (Figs. 3.5, B14-19). Experiments PV1 (< 100 μm thick) and PHe03 (< 60 μm thick) generated the greatest volume of gouge. PHe02 (< 60 μm thick), PHe04 (< 60 μm thick), and PHe06 (< 50 μm thick) generated minor volumes, and

Table 3.3. Results of a-b calculations from velocity-step tests.

Name	V_i (μm/s)	V_f (μm/s)	μ_f	a-b	Magnitude of velocity step
mock_s1	50	1000	0.41	0.0010	19.91
mock_s2	3	30	0.41	0.0039	10
plan1_s1	0.85	50	0.36	0.0012	58.5
plan2_s1	4	50	0.41	-0.0053	11.7
plan2_s2	50	500	0.41	0.0013	10
setup1_s1	10	100	0.27	0.0048	10
setup1_s2	100	10	0.27	0.0043	0.1
setup1_s3	10	1000	0.28	0.0009	101.6
setup1_s4	10	1000	0.27	0.0022	101.6
setup1_s5	10	50	0.25	0.0074	5
setup1_s6	50	100	0.26	-0.0014	2
setup1_s7	100	500	0.26	-0.0012	5
setup2_s1	10	0.85	0.26	-0.0008	0.09
setup2_s2	0.85	1000	0.26	0.0011	1167
setup2_s3	5	500	0.26	0.0087	97.5
setup2_s4	500	50	0.25	0.0022	0.1
setup2_s5	50	500	0.26	0.0004	10
PV1_s1	10	100	0.42	-0.0030	10
PV1_s2	100	1000	0.42	0.0100	10
PV1_s3	100	10	0.43	0.0017	0.1
PV1_s4	10	100	0.44	0.0043	10
PV1_s5	10	500	0.45	0.0015	50
PV1_s6	10	50	0.44	-0.0006	5
PV1_s7	50	500	0.44	0.0026	10

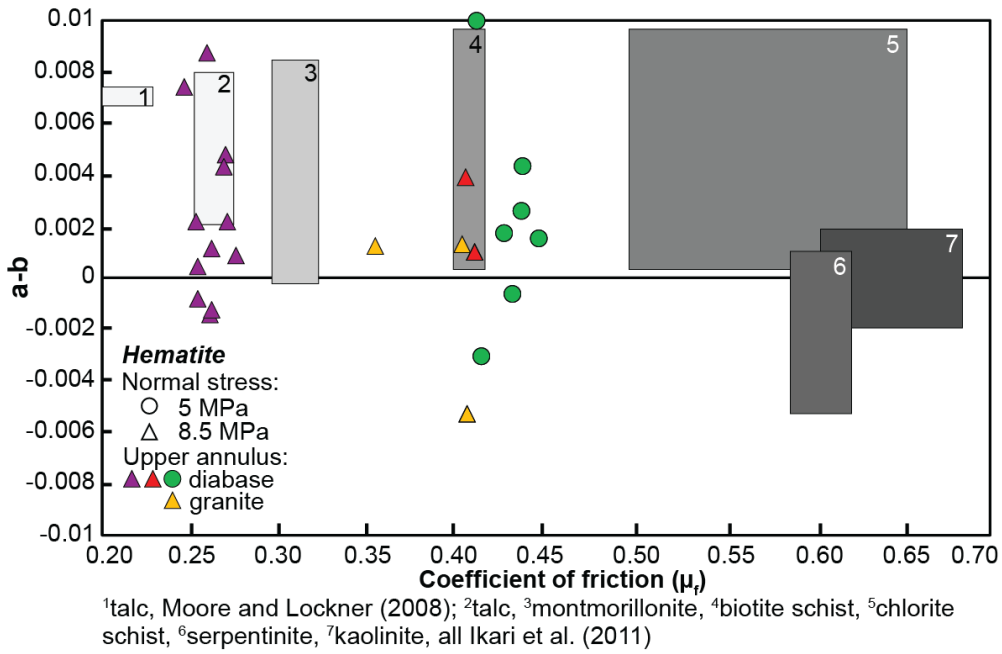

[1]talc, Moore and Lockner (2008); [2]talc, [3]montmorillonite, [4]biotite schist, [5]chlorite schist, [6]serpentinite, [7]kaolinite, all Ikari et al. (2011)

Figure 3.3. Hematite values of a-b for coefficients of friction with measured values of phyllosilicates and phyllosilicate-rich rocks in white and grey for comparison (Ikari et al., 2011; Moore and Lockner, 2008). Hematite is frictionally weak and displays primarily velocity-strengthening to velocity-neutral frictional behavior, which is similar to phyllosilicates and phyllosilicate-bearing rocks.

PHe01 (< 30 μm thick) and PHe05 (< 50 μm thick) did not generate enough gouge to cover the full slip surface. SEM shows gouge particles with diameters of > 0.1 to 65 μm (Figs. 3.4B, 3.4D, Table 3.4) on the surface and infilling depressions below the slip surface (Fig. 3.4B). Larger gouge volumes were generated where natural pores exist in the slab. Average gouge particle size decreases towards the slip surface (Fig. 3.4B). Hematite gouge particles are angular and some larger particles display conchoidal fractures (Fig. 3.4D). Below the experimentally-generated fault surface, hematite plates are either undeformed or display conchoidal fractures where grains are fractured or broken to create gouge (Fig. 3.4C).

3.3.3. (U-Th)/He results

We acquired 49 individual aliquot hematite He dates including 22 analyses from gouge generated during seven deformation experiments and 27 dates from undeformed but homogenized starting material from hematite slabs used in experiments PHe01 through PHe06 and PV1 (Table 3.5; Figs. 3.6, 3.7). Analytical uncertainties on individual analyses are ~1-3%, and standard deviations of all mean sample dates are <15%. We report the range of individual dates with their 2σ analytical error for each sample (i.e., gouge replicates and homogenized starting material replicates from each hematite slab), and mean sample dates ± 1σ standard deviation for all samples. *Undeformed homogenized starting material*

Across the entire dataset, hematite He dates from undeformed, homogenized starting material span 236 ± 7 Ma to 155 ± 5 Ma with a mean of 198 ± 17 Ma (9% standard deviation, std. dev.). Four individual dates from experiment PHe01

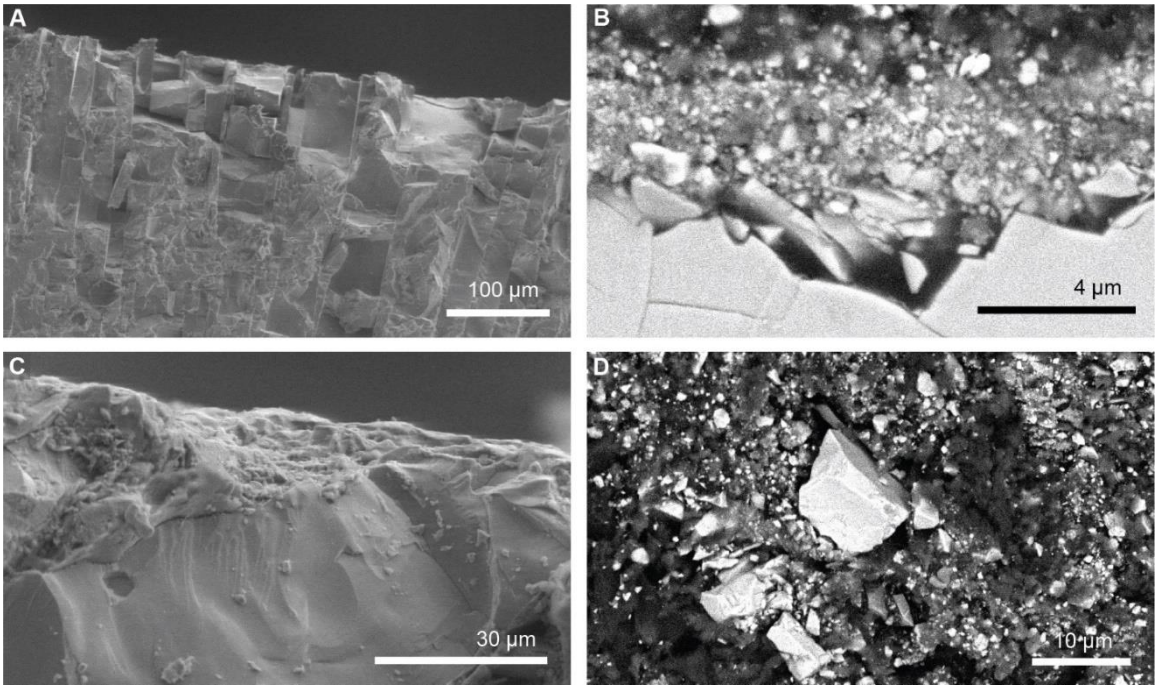

Figure 3.4. A: Secondary electron (SE) image of undeformed hematite plates perpendicular to the slip surface. **B:** Backscatter electron (BSE) image of depression along slip surface filled with gouge. **C:** SE image of surface showing conchoidal fracture with gouge particles deposited on top. **D:** BSE image of gouge particles showing a distribution of grain sizes.

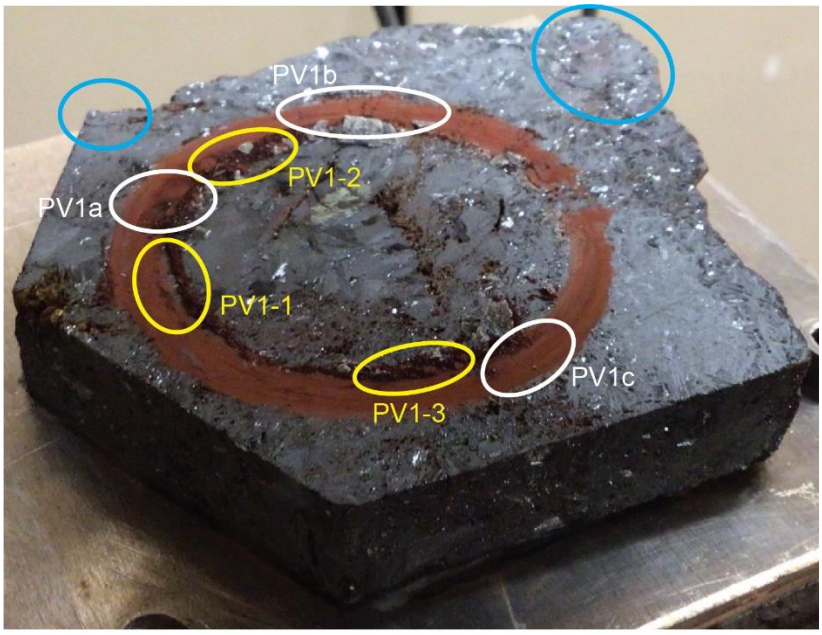

D21-PV1

Blue - undeformed homogenized material for (U-Th)/He
Yellow - deformed gouge for (U-Th)/He
White - SEM microstructures
inner diameter of ring ~44.35 mm

Figure 3.5. Specularite Plate PV1 with sampling locations for thermochronometry and SEM circled. The plate has a thin layer of gouge with slickenlines and a locally-developed thicker surrounding ring.

Table 3.4. Hematite gouge diameters measured by SEM from plates for each experiment.

Experiment	Count	Min (µm)	Max (µm)	Average (µm)	St. Dev (µm)
PHe01	324	0.1	19.5	1.1	1.7
PHe02	399	0.1	6.9	0.4	0.5
PHe03	324	0.1	17.5	0.6	1.4
PHe04	371	0.1	5.8	0.5	0.7
PHe05	325	0.1	65	1.4	3.9
PHe06	309	0.1	6.3	0.5	0.7
PV1	393	0.1	14.7	0.6	1.2

range from 210 ± 6 Ma to 196 ± 6 Ma with a mean date of 205 ± 6 Ma (3% std. dev.). Individual dates from experiment PHe02 range 197 ± 8 Ma to 176 ± 7 Ma (n = 4) with a mean of 188 ± 9 Ma (5% std. dev). PHe03 yields four individual dates of 195 ± 6 Ma to 168 ± 6 Ma with a mean of 185 ± 11 Ma (6% std. dev.). Dates from experiment PHe04 are 199 ± 6 Ma to 191 ± 6 Ma (n = 4) and a mean of 195 ± 3 Ma (2% std. dev.). Four individual dates from PHe05 are 214 ± 7 Ma to 155 ± 5 Ma, with a mean of 187 ± 22 Ma (12% std. dev.). Six dates from PHe06 range from 226 ± 7 Ma to 202 ± 6 Ma, with a mean of 209 ± 10 Ma (5% std. dev.). Three dates from PV1 are 236 ± 7 Ma to 216 ± 6 Ma, with a mean date of 224 ± 8 Ma (4% std. dev.). New dates overlap with undeformed homogenized starting material hematite He dates of Calzolari et al. (2020) of 240 ± 7 Ma to 162 ± 4 Ma, with a mean of 194 ± 28 Ma (14 % std. dev.).

Gouge

Individual dates acquired from gouge come from PHe01, PHe02, PHe04, PHe05, PHe06, and PV1 deformation experiments (Table 3.5, Figs. 3.6, 3.7). We do not report results from PHe03 owing to Th contamination from the Th-rich SiC upper annulus that broke down during the deformation experiment and mixed SiC gouge into the hematite gouge. Two individual dates from PHe01 (1 mm/s, 1 cm) are 165 ± 5 Ma and 162 ± 5 Ma (mean = 164 ± 1 Ma, 1% std. dev.). PHe02 (1 mm/s, 3 cm) yields five dates of 190 ± 5 Ma to 145 ± 4 Ma, with a mean of 170 ± 18 Ma (11% std. dev.). Two aliquots from experiment PHe04 (0.858 μm/s, 1 cm) have 193 ± 6 Ma and 176 ± 6 Ma dates (mean 184 ± 8 Ma, 5% std. dev.). PHe05 (0.858 μm/s, 3 cm) yields three dates ranging from 206 ± 7

Table 3.5. Hematite (U-Th)/He thermochronometry data. Blue samples are outlier analyses that were removed from discussion. See Appendix B for discussion of these analyses.

	Sample	U (ng)	1σ ± U (ng)	Th (ng)	1σ ± Th (ng)	Th/U	He (pmol)	1σ ± He (pmol)	Date (Ma)	2σ (Ma)
deformed	D21-PV1_h1	0.126	0.002	0.043	0.001	0.349	0.136	0.001	182	6
	D21-PV1_h2	0.104	0.002	0.040	0.001	0.398	0.111	0.003	178	12
	D21-PV1_h3	0.232	0.003	0.154	0.002	0.681	0.230	0.002	158	5
	D21-PV1_h4	0.125	0.002	0.036	0.001	0.296	0.135	0.001	185	6
	D21-PV1_h5	0.144	0.002	0.066	0.001	0.471	0.154	0.001	177	6
								Mean	**176**	
								Std. Dev.	**9**	**5%**
deformed	D21-PHe6_h1	0.121	0.002	0.052	0.001	0.440	0.105	0.001	145	5
	D21-PHe6_h2	0.127	0.002	0.040	0.001	0.323	0.121	0.001	163	5
	D21-PHe6_h3	0.179	0.003	0.090	0.001	0.516	0.188	0.002	172	6
	D21-PHe6_h4	0.078	0.001	0.025	0.000	0.331	0.062	0.001	136	5
	D21-PHe6_h5	0.089	0.001	0.059	0.001	0.682	0.084	0.001	148	5
								Mean	**153**	
								Std. Dev.	**13**	**8%**
deformed	D21-PHe5_h1	0.119	0.002	0.032	0.001	0.275	0.140	0.001	201	7
	D21-PHe5_h2	0.048	0.001	0.016	0.000	0.333	0.059	0.001	206	7
	D21-PHe5_h3	0.126	0.002	0.027	0.000	0.219	0.222	0.002	303	10
	D21-PHe5_h4	0.030	0.000	0.010	0.000	0.327	0.036	0.000	199	7
								Mean	**202**	
								Std. Dev.	**3**	**1%**

	Sample	U (ng)	1σ ± U(ng)	Th (ng)	1σ ± Th(ng)	Th/U	He (pmol)	1σ ± He (pmol)	Date (Ma)	2σ (Ma)
deformed	D21-PHe4_h1	0.193	0.003	0.049	0.001	0.262	0.216	0.002	193	6
	D21-PHe4_h2	0.101	0.002	0.039	0.001	0.398	0.106	0.001	176	6
	D21-PHe4_h3	0.071	0.001	0.061	0.001	0.875	0.066	0.001	141	4
								Mean	**184**	
								Std. Dev.	**8**	**5%**
deformed	D21-PHe3_h1	0.477	0.007	0.726	0.011	1.563	0.307	0.003	87	3
	D21-PHe3_h2	0.314	0.005	0.470	0.007	1.536	0.208	0.001	90	2
	D21-PHe3_h3	0.307	0.004	0.421	0.006	1.405	0.257	0.001	116	3
	D21-PHe3_h4	0.698	0.010	1.206	0.018	1.773	0.483	0.002	90	2
	D21-PHe3_h5	0.275	0.004	0.660	0.010	2.460	0.154	0.001	66	2
deformed	D21-PHe2_h1	0.271	0.004	0.059	0.001	0.222	0.239	0.001	154	4
	D21-PHe2_h2	0.253	0.004	0.054	0.001	0.220	0.210	0.001	145	4
	D21-PHe2_h3	0.261	0.004	0.047	0.001	0.185	0.284	0.001	190	5
	D21-PHe2_h4	0.428	0.006	0.107	0.002	0.257	0.423	0.002	171	5
	D21-PHe2_h5	0.099	0.001	0.021	0.000	0.218	0.107	0.001	188	6
								Mean	**170**	
								Std. Dev.	**18**	**11%**
deformed	D21-PHe1_h1	0.154	0.002	0.034	0.001	0.227	0.143	0.001	162	5
	D21-PHe1_h2	0.371	0.005	0.057	0.001	0.159	0.347	0.002	165	5
								Mean	**164**	
								Std. Dev.	**1**	**1%**

	Sample	U (ng)	1σ ± U(ng)	Th (ng)	1σ ± Th(ng)	Th/U	He (pmol)	1σ ± He (pmol)	Date (Ma)	2σ (Ma)
undeformed	D21-PV1P_h1	0.397	0.006	0.077	0.001	0.199	0.538	0.003	236	7
	D21-PV1P_h2	0.174	0.003	0.181	0.003	1.067	0.172	0.001	146	4
	D21-PV1P_h3	0.194	0.003	0.032	0.001	0.171	0.240	0.001	216	6
	D21-PV1P_h4	0.344	0.005	0.069	0.001	0.206	0.438	0.002	221	6
								Mean	**224**	
								Std. Dev.	**8**	**4%**
undeformed	D21-PHe1P_h1	0.206	0.003	0.031	0.001	0.152	0.245	0.001	209	6
	D21-PHe1P_h2	0.236	0.003	0.037	0.001	0.159	0.274	0.001	204	6
	D21-PHe1P_h3	0.228	0.003	0.036	0.001	0.163	0.254	0.001	196	6
	D21-PHe1P_h4	0.200	0.003	0.028	0.000	0.145	0.239	0.001	210	6
								Mean	**205**	
								Std. Dev.	**6**	**3%**
undeformed	D21-PHe2P_h1	0.250	0.004	0.056	0.001	0.230	0.282	0.004	196	8
	D21-PHe2P_h2	0.306	0.005	0.114	0.002	0.382	0.321	0.005	176	7
	D21-PHe2P_h3	0.250	0.004	0.058	0.001	0.238	0.286	0.005	197	8
	D21-PHe2P_h4	0.342	0.005	0.088	0.001	0.263	0.363	0.006	182	8
								Mean	**188**	
								Std. Dev.	**9**	**5%**

	Sample	U (ng)	1σ ± U(ng)	Th (ng)	1σ ± Th(ng)	Th/U	He (pmol)	1σ ± He (pmol)	Date (Ma)	2σ (Ma)
undeformed	D21-PHe3P_h1	0.252	0.004	0.084	0.001	0.343	0.270	0.004	182	8
	D21-PHe3P_h2	0.265	0.004	0.092	0.001	0.354	0.306	0.002	195	6
	D21-PHe3P_h3	0.265	0.004	0.130	0.002	0.503	0.314	0.002	194	6
	D21-PHe3P_h4	0.248	0.004	0.082	0.001	0.338	0.246	0.003	168	6
								Mean	**185**	
								Std. Dev.	**11**	**6%**
undeformed	D21-PHe4P_h1	0.196	0.003	0.052	0.001	0.274	0.221	0.002	193	6
	D21-PHe4P_h2	0.207	0.003	0.056	0.001	0.278	0.240	0.002	199	6
	D21-PHe4P_h3	0.194	0.003	0.050	0.001	0.264	0.223	0.002	198	6
	D21-PHe4P_h4	0.279	0.004	0.067	0.001	0.245	0.309	0.002	191	6
								Mean	**195**	
								Std. Dev.	**3**	**2%**
undeformed	D21-PHe5P_h1	0.278	0.004	0.068	0.001	0.253	0.346	0.002	214	7
	D21-PHe5P_h2	0.128	0.002	0.065	0.001	0.519	0.121	0.001	155	5
	D21-PHe5P_h3	0.303	0.005	0.113	0.002	0.381	0.361	0.002	200	6
	D21-PHe5P_h4	0.452	0.007	0.145	0.002	0.328	0.478	0.003	180	5
								Mean	**187**	
								Std. Dev.	**22**	**12%**

undeformed

Sample	U (ng)	1σ ± U(ng)	Th (ng)	1σ ± Th(ng)	Th/U	He (pmol)	1σ ± He (pmol)	Date (Ma)	2σ (Ma)
D21-PHe6P_h1	0.351	0.005	0.059	0.001	0.172	0.453	0.003	226	7
D21-PHe6P_h2	0.252	0.004	0.064	0.001	0.262	0.296	0.000	202	6
D21-PHe6P_h3	0.248	0.004	0.052	0.001	0.217	0.293	0.000	205	6
D21-PHe6P_h4	0.260	0.004	0.068	0.001	0.267	0.309	0.000	204	6
							Mean	**209**	
							Std. Dev.	**10**	**5%**

Ma to 199 ± 7 Ma, with a mean of 202 ± 3 Ma (1% std. dev.). Five dates from PHe06 (32cm/s, 3 cm) are 172 ± 6 Ma to 136 ± 5 Ma, with a mean of 153 ± 13 Ma (8% std. dev.). Five aliquots from PV1 (velocity-step test, ~13.5 cm displacement) yield dates ranging from 185 ± 6 Ma to 158 ± 5 Ma with a mean date of 176 ± 9 Ma (5% std. dev.).

3.4. Discussion

3.4.1. Frictional data

Our experimental results reveal specular hematite is frictionally weak with a μ that ranges from 0.18 to 0.45 and displays predominantly velocity-neutral to velocity-strengthening behavior at slip rates below ~1 mm/s. There is no relation between velocity and μ_{ss} at 0.85 μm/s to 1 cm/s and the upper annulus material does not impact the observed range of μ. A single data point at 320 mm/s is insufficient to evaluate whether there is a decrease in μ_{ss} when approaching seismic slip rates. Experiments described in Calzolari et al. (2020) yield a coefficient of friction of 0.28 ± 0.12 at velocities of 0.01 mm/s and 320 mm/s, which is consistent and overlaps with our results. The Calzolari et al. (2020) experiments show dynamic weakening with increased sliding distance for "interrupted slip" protocols with peak velocities of ~320 mm/s and evidence of He loss during frictional heating.

We do not observe a relationship between sliding distance and μ in hematite, indicating dynamic weakening does not occur at slower velocities (<1 mm/s, Di Toro et al., 2004; Di Toro et al., 2011). However, because our experiments explore only a portion of the range of possible sliding velocities (0.85 μm/s to ~330 mm/s) or normal stresses (>0 to 8.5 MPa) that the Instron apparatus is capable of, we have not captured conditions

that promote the transition to dynamic weakening or the dependence of μ on normal stress. The experiment conducted at 5 MPa (PV1) yielded a mean μ of 0.43 and two experiments conducted at 8.5 MPa yield lower μ of 0.26 (Setup1) and 0.25 (Setup2). The origin of this anomalous behavior where an increasing normal stress yields a low μ is unknown, but error some may be attributed to local variations in normal stress that occurred when the upper annulus material broke. Deforming these samples at plate-motion rates could also add additional context for hematite frictional behavior (Ikari, 2019; Ikari and Kopf, 2017). Owing to the nature of the starting material (i.e., slabbed, ground, competent, specularite), additional deformation experiments are required to document the impacts of gouge layer development and hematite plate orientation on frictional behavior. Aseismic creep is thought to occur on weak faults with a phyllosilicate-rich mineralogy that promotes velocity-strengthening behavior (e.g., Kaduri et al., 2017; Moore et al., 2016; Schleicher et al., 2010), and transient slow (subseismic) slip may occur on faults with heterogeneous friction, where a transition from velocity-strengthening to velocity-weakening, or velocity-neutral frictional behavior occurs (Wei et al., 2013). In laboratory experiments, slow slip arises at near the stability boundary defined by the critical stiffness (Ikari, 2019; Leeman et al., 2018; Leeman et al., 2016), but phyllosilicates may decrease the velocity that events propagate at (Ikari, 2019). Our results imply shallow hematite-bearing faults may accommodate aseismic creep or transient slow slip because hematite is frictionally weak and displays velocity-strengthening and velocity-neutral behavior at slow rates. The frictional properties (μ and a-b) of hematite are comparable to phyllosilicate minerals (Behnsen and Faulkner, 2012; Moore and Lockner, 2004, 2008; Sánchez-Roa et al., 2017), synthetic gouge with varying

proportions of phyllosilicates (Ikari et al., 2011), and gouge prepared from phyllosilicate-bearing samples collected from locations where shallow slow slip and creep are observed geodetically or geophysically (Carpenter et al., 2015; Ikari, 2019; Moore et al., 2016) (Fig. 3.3). Minor components of weak phases concentrated in a fabric may influence the strength of the surrounding rock (Collettini et al., 2009), so networks of hematite-coated faults (DiMonte et al., in review; McDermott et al., 2021) may contribute to bulk fault zone rheology.

Aseismic creep is thought to occur on weak faults with a phyllosilicate-rich mineralogy that promotes velocity-strengthening behavior (e.g., Kaduri et al., 2017; Moore et al., 2016; Schleicher et al., 2010), and transient slow (subseismic) slip may occur on faults with heterogeneous friction, where a transition from velocity-strengthening to velocity-weakening, or velocity-neutral frictional behavior occurs (Wei et al., 2013). In laboratory experiments, slow slip arises at near the stability boundary defined by the critical stiffness (Ikari, 2019; Leeman et al., 2018; Leeman et al., 2016), but phyllosilicates may decrease the velocity that events propagate at (Ikari, 2019). Our results imply shallow hematite-bearing faults may accommodate aseismic creep or transient slow slip because hematite is frictionally weak and displays velocity-strengthening and velocity-neutral behavior at slow rates. The frictional properties (μ and a-b) of hematite are comparable to phyllosilicate minerals (Behnsen and Faulkner, 2012; Moore and Lockner, 2004, 2008; Sánchez-Roa et al., 2017), synthetic gouge with varying proportions of phyllosilicates (Ikari et al., 2011), and gouge prepared from phyllosilicate-bearing samples collected from locations where shallow slow slip and creep are observed geodetically or geophysically (Carpenter et al., 2015; Ikari, 2019; Moore et al., 2016)

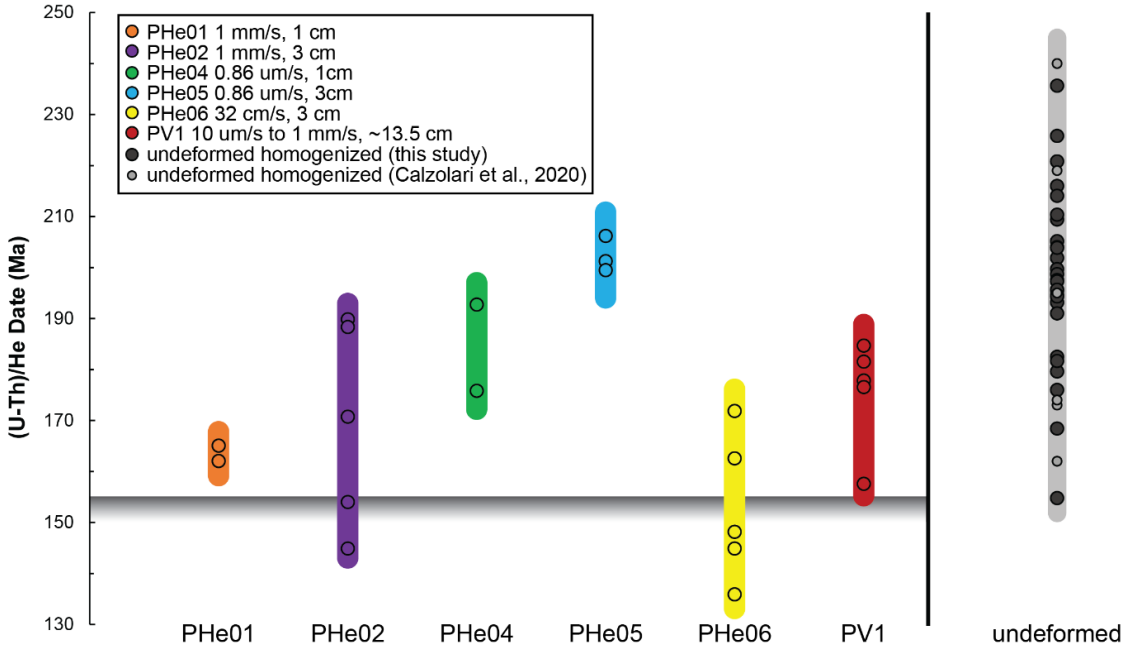

Figure 3.6. Range of hematite (U-Th)/He dates (individual dates ± 2σ analytical error) of deformed gouge aliquots (color) and undeformed (grey, right) aliquots; horizontal grey bar denoting the youngest date (-2σ analytical error) of the undeformed aliquots. Some gouge dates from experiments PHe02 and PHe06 are younger than the youngest undeformed date indicating He loss during the deformation experiment.

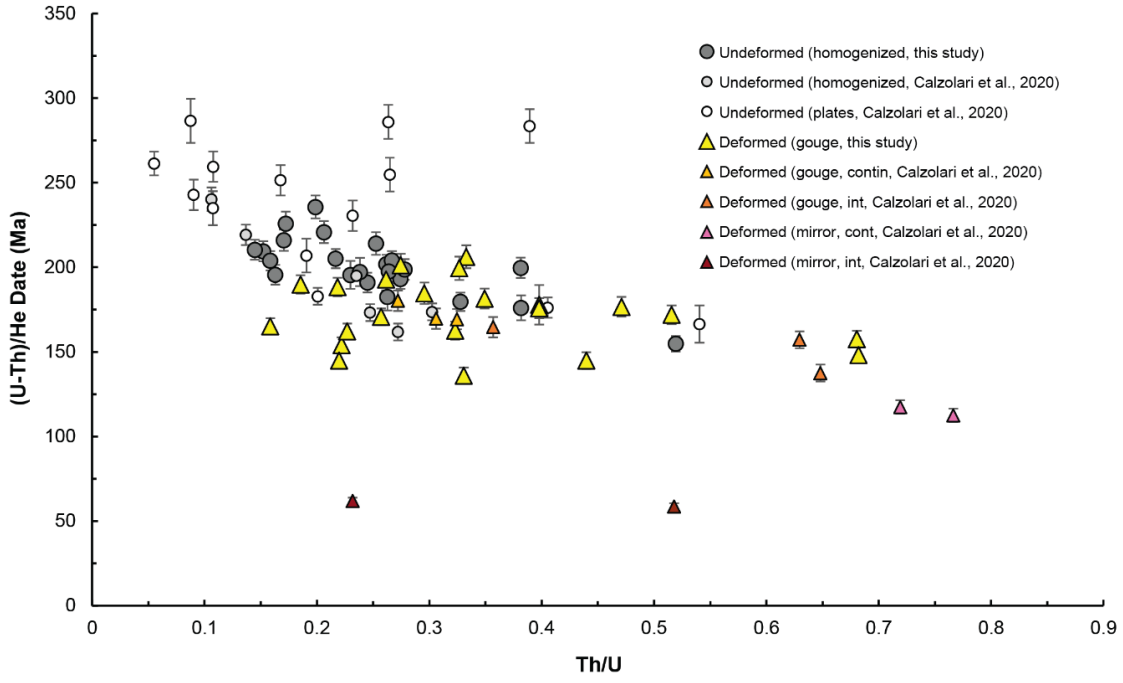

Figure 3.7. All hematite (U-Th)/He dates with their 2σ analytical error from this study (larger symbols) and (Calzolari et al., 2020) (smaller symbols) as a function of Th/U. Undeformed specularite dates denoted with grey circles; deformed gouge dates are yellow, orange, red. (U-Th)/He dates do not display a positive relationship between Th/U and date, indicating U loss during degassing likely did not occur.

(Fig. 3.3). Minor components of weak phases concentrated in a fabric may influence the strength of the surrounding rock (Collettini et al., 2009), so networks of hematite-coated faults (DiMonte et al., in review; McDermott et al., 2021) may contribute to bulk fault zone rheology.

3.4.2. Textural development and comparison to naturally deformed hematite

SEM analyses reveal the development of gouge layers comprising micro- to nanoparticles during deformation experiments. Gouge particles and broken hematite plates display conchoidal fracture because hematite does not have cleavage. Gouge creation reflects extreme grain-size reduction, with undeformed plate thicknesses average ~17 μm (Calzolari et al., 2020) and gouge particles yield an average diameter of ~0.69 μm. Assuming this initial hematite plate thickness and a ~2 mm length, and that final gouge particles are cubic with lengths of ~0.69 μm, gouge generation induces a ~7200% increase in hematite particle surface area. Experiments at slow rates and low displacement generated a limited volume of gouge. Gouge particle size is similar across all experiments regardless of slip rate and displacement, and the grain size distribution is consistent with observations from Calzolari et al. (2020). However, these prior experiments at higher slip rates and longer displacement generate thicker gouge layers and mirror-like textures comprising sintered nanoparticles (~330 mm/s, 1.5 m, Calzolari et al., 2020).

Experiments were conducted on specular hematite that likely precipitated at depth and/or at elevated fluid temperatures. This grain size distribution and grain morphology are markedly different from hematite formed at shallow depths and deformed by slow

slip fault processes (DiMonte et al., in review; McDermott et al., 2021). Natural hematite that forms at shallow depths and experienced aseismic creep or transient slow slip exhibits a high-aspect ratio platy morphology with a plate thickness of ~30 nm and length from ~300 nm to 1 μm. Shallow hematite does not experience comminution during post-mineralization slip and retains its platy, high-aspect ratio morphology (DiMonte et al., in review; McDermott et al., 2021). Natural textures differ from our experimentally-generated hematite gouge, which is the product of extreme grain size reduction and develops an angular to subangular morphology.

Hematite gouge thickness that developed on the surface of specularite slabs is on average ~5 μm, which is notably thinner than hematite-coated fault surfaces in nature (~20 μm- to ~1 cm-thick; e.g., Ault et al., 2015; Calzolari et al., 2018; DiMonte et al., in review; McDermott et al., 2017, 2021; Moser et al., 2017; Odlum et al., 2021). Polycrystalline hematite along these fault surfaces is also a significantly thinner and thus smaller volume than the specularite slabs used in these experiments. Some natural hematite surfaces are impure, hematite-matrix cataclasite with clasts of other phases, and some surfaces reflect the interaction of multi-mineral systems where weak hematite accommodates slip (DiMonte et al., in review; McDermott et al., 2021). In nature, hematite faults comprising platy hematite may exhibit a scaly fabric or S-C structures that developed via hematite interplate sliding, which are fabrics not observed in the experimentally-generated gouge (DiMonte et al., in review; McDermott et al., 2021). Other experiments conducted with phyllosilicate gouge with sheet-like morphologies as a starting material displayed Riedel shears and alignment of plates parallel to shear

(Behnsen and Faulkner, 2012; Moore and Lockner, 2004; Sánchez-Roa et al., 2017). We do not observe these structures in the hematite gouge produced during experimental slip.

3.4.3. He loss during comminution

Comparison between hematite He dates from undeformed grain-size homogenized starting material with and resulting gouge generated during slow slip experiments allows us to evaluate He loss during extreme comminution at slip rates of < 1 mm/s and 320 mm/s. We assume that (U-Th)/He date is a proxy for He concentration, and thus comparing dates from undeformed and deformed samples approximates He loss. He loss was calculated using Equation 3.2 (Table 3.6).

$$\text{He loss} = \frac{\text{Date (undeformed, Ma)- Date (deformed, Ma)}}{\text{Date (undeformed, Ma)}} \text{x } 100$$

Equation 3.2

We conservatively assess the % He loss by comparing average and minimum dates from gouge from each experiment to the entire dataset of undeformed starting material, including homogenized undeformed dates from Calzolari et al. (2020). Although we homogenized the grain size of the starting material to remove some of the hematite He date variability that is a function of grain size (Calzolari et al., 2020), we could not achieve uniform grain size. Thus, our starting material benchmark dates for each slab exhibit intrasample scatter. In addition, the undeformed homogenized starting material from each slab subsamples a portion, but not the same portion, of grain sizes and may not reflect the entire range of potential dates. Owing to these complexities, we compare gouge from each experiment with the entire range of undeformed starting

material dates. Finally, because gouge aliquots may still include larger plates with a higher He budget (i.e., older dates), calculated % He loss is a minimum estimate.

The majority of individual hematite He dates from gouge overlap with the range of dates from undeformed starting material, and most individual dates do not show evidence for He loss (Figures 3.6, 3.7, Table 3.6). However, experiments PHe06 and PHe02 show observable He loss (12% and 6%, respectively), when comparing minimum gouge dates to the minimum of the entire undeformed dataset (Figure 3.6, Table 3.6). Gouge from the interrupted slip experiment of Calzolari et al. (2020) exhibits comparable He loss (11%). Although most individual gouge dates overlap with and are not younger than the undeformed dataset, dates from gouge do not overlap with the older portion of undeformed dates. Comparison of average gouge dates to the average of the undeformed dataset shows that He loss occurred during gouge formation in the majority of experiments.

Fault slip temperature rise was calculated to evaluate the potential effect of friction-generated temperature rise on He diffusion from generated hematite gouge (Table 3.7). Temperature rise for fault surfaces is calculated with:

$$T_{fs} = \frac{\mu\sigma_n}{\rho c} \times \frac{V\sqrt{t}}{\sqrt{\pi\alpha}}$$ (Lachenbruch, 1986) Equation 3.3

where μ (average coefficient of friction for experiment), σ_n (applied normal stress, 8.5 MPa except for Phe03, 5 MPa), ρ (hematite density, 5300 kg/m3, Nesse, 2012), c (heat capacity, 137.67 J/kgK, Chase, 1983), V (applied velocity for experiment, m/s), t

Table 3.6. Hematite He loss assessment using equation 3.2.

Name	He loss (sample mean, %)	He loss (sample minimum, %)	He loss (sample average to dataset minimum, %)	He loss (sample average to dataset average, %)	He loss (sample minimum to dataset minimum, %)
PV1	22	27	-13	**12**	**-2**
PHe6	16	33	-14	**11**	**12**
PHe5	-8	-29	-31	**-3**	**-29**
PHe4	6	8	-19	**7**	**-14**
PHe2	10	18	-10	**14**	**6**
PHe1	20	17	-6	**17**	**-5**
Calzolari et al., 2020, gouge contin.			-12	**12**	**-9**
Calzolari et al., 2020, gouge int.			1	**22**	**11**
Calzolari et al., 2020, mirror contin.			61	**69**	**62**
Calzolari et al., 2020, mirror int.			26	**41**	**27**

(experiment time, s), α (thermal diffusivity, 1.55x10-5 m2/s, α = k/(ρc), where k (thermal conductivity) = 11.3 W/mK, Horai, 1971).

The results of our calculations (Table 3.7) reveal that experiments Phe03 (82 °C) and Phe06 (67 °C) yielded minor temperature rise above ambient room temperature of 20 °C. Inducing 10% He loss requires a fault surface temperature of 87 °C (i.e., PHe06) and heating duration of ~0.4 Ma for a ~0.69 μm-diameter hematite gouge (average particle diameter in PHe06 (assuming diffusion kinetics of Farley, 2018, Ea = 171, ln(Do) = -0.66). A fault experiencing continuous slip at 320 mm/s would require ~0.5 hr to induce 10% He loss (Farley, 2018). These calculations indicate temperature rise alone does not contribute to He loss within our experimental faults. Calzolari et al. (2020) interpreted substantive He loss only from mirror-like portions of faults generated at 320 mm/s. Helium is not charged nor bound within the crystal structure (Baxter et al., 2007). Typically, He loss in hematite occurs by thermally-activated volume diffusion and the minimum grain dimension (e.g., plate-width) controls the volume fraction He loss (Balout et al., 2017; Farley, 2018; Jensen et al., 2018). During fault slip, He loss may arise solely due to the formation of new grain surfaces that intersect and expose He where it was previously trapped within interstitial space in the crystal lattice (Fig. 3.8). Because we observe evidence of He loss in our slow slip deformation experiments in the absence of temperature rise, we propose that He loss in gouge may occur via comminution alone. This implies that ultracataclasite developed within specular hematite comprising μm-thick plates on natural fault surfaces (McDermott et al., 2017; Odlum et al., 2022) resembling our initial starting material may not retain all its He during fault slip regardless of whether deformation is associated with temperature rise.

Table 3.7. Fault temperature rise calculations using equation 3.3.

Name	σ_n (Mpa)	μ	Displacement (m)	Time (s)	Fault temperature rise (°C)
PHe01	8.5	0.18	0.01	10	1
PHe02	8.5	0.41	0.03	30	4
PHe03	8.5	0.4	1.5	150	82
PHe04	8.5	0.4	0.01	11880	0
PHe05	8.5	0.4	0.03	35280	0
PHe06	8.5	0.3	0.03	0.09	67
PV1	5	0.44	0.135	3330	2

In shallow portions of fault zones, networks of nanometer-scale hematite platelets retain their original morphology and do not show evidence of grain size reduction (DiMonte et al., in review; McDermott et al., 2021). Our new deformation experiment results reveal that deformation-induced He loss likely does not occur in hematite on these surfaces. Thus, ongoing slow slip accommodated on these slip surfaces does not induce He loss.

3.5. Conclusions

Our mechanical observations from experimentally generated hematite slip surfaces reveal that hematite is a weak phase that exhibits primarily velocity strengthening to velocity neutral behavior at slip rates of <1 mm/s. This frictional behavior is comparable to deformation experiment results from phyllosilicate minerals and phyllosilicate-bearing rocks.

Our textural results show that experimental hematite faults developed thin gouge layers reflecting comminution along the slip surface that increases the hematite particle surface area by 7200%, which serves to expose a greater number of He atoms to the surface. Although interpretation of our hematite He thermochronometric data is complicated because of the wide range of dates from the undeformed starting material that did not fully homogenize He date-grain size effects, our comparative results suggest gouge generated during experiments experiences some He loss without the associated temperature rise that typically induces volume diffusion of He over seconds to hours. Our data comparison and calculations reveal a non-thermal mechanism caused He loss. We

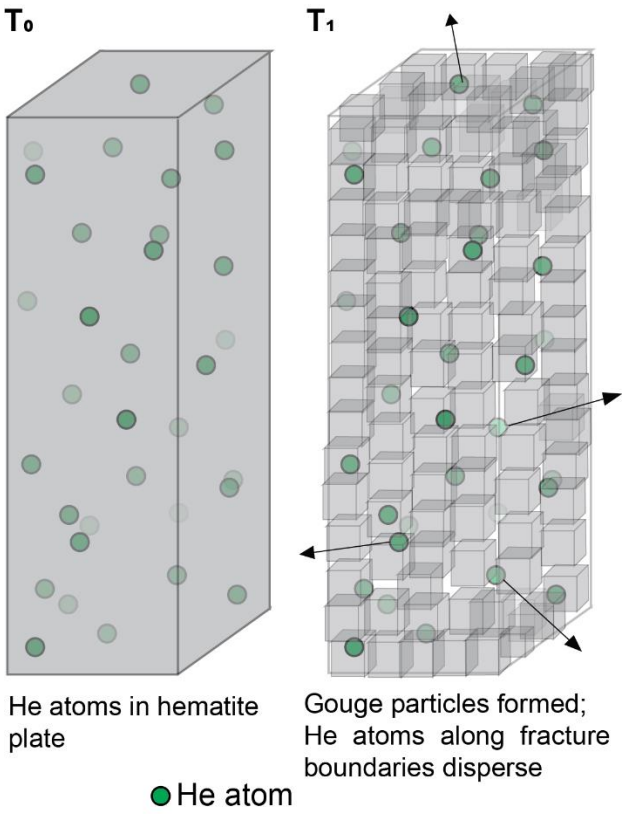

Figure 3.8. Schematic diagram of a hematite plate with He atoms in the crystal lattice (T_0). Hematite plate comminutes to form smaller gouge particles and He disperses along developed grain boundaries (T_1).

suggest that He is lost from hematite along surfaces generated during grain size reduction that significantly increases surface area.

These results have implications for hematite-bearing faults in nature. Hematite faults may accommodate aseismic creep or transient slow slip due to its rate-and-state frictional behavior that promotes stable slip at slow driving velocities. Additional experiments will determine whether hematite displays greater velocity-weakening behavior at faster velocities, a property that could permit earthquakes to propagate within hematite. We also emphasize that the starting material and generated gouge in our slow slip experiments display different textures and grain size distributions from hematite that precipitates in the shallow portions of fault zones (DiMonte et al., in review; McDermott et al., 2021). Experiments conducted on gouge with high-aspect ratio hematite plates extracted from natural fault surface will provide complementary rate-and-state frictional data and inform the textural evolution of these shallow natural surfaces. Our (U-Th)/He data patterns imply that hematite gouge or ultracataclasite reflecting comminution may show evidence of He loss that would be solely due to this grain size reduction. Hematite surfaces characterized by a platy morphology that do not accommodate grain size reduction during post-precipitation fault slip should only reflect He loss due to thermal processes (i.e., friction-generated heat and hydrothermal fluid circulation). This observation is important for the interpretation of hematite (U-Th)/He dates from fault rocks.

REFERENCES

Allegre, C. J., Poirier, J.-P., Humler, E., and Hofmann, A. W., 1995, The chemical composition of the Earth: Earth and Planetary Science Letters, v. 134, no. 3-4, p. 515-526.

Ault, A. K., 2020, Hematite fault rock thermochronometry and textures inform fault zone processes: Journal of Structural Geology, p. 104002.

Ault, A. K., Jensen, J. L., McDermott, R. G., Shen, F.-A., and Van Devener, B. R., 2019, Nanoscale evidence for temperature-induced transient rheology and postseismic fault healing: Geology.

Balout, H., Roques, J., Gautheron, C., Tassan-Got, L., and Mbongo-Djimbi, D., 2017, Helium diffusion in pure hematite (α-Fe2O3) for thermochronometric applications: A theoretical multi-scale study: Computational and Theoretical Chemistry, v. 1099, p. 21-28.

Baxter, E. F., Asimow, P. D., and Farley, K. A., 2007, Grain boundary partitioning of Ar and He: Geochimica et Cosmochimica Acta, v. 71, no. 2, p. 434-451.

Beeler, N., Tullis, T., and Weeks, J., 1994, The roles of time and displacement in the evolution effect in rock friction: Geophysical Research Letters, v. 21, no. 18, p. 1987-1990.

Behnsen, J., and Faulkner, D. R., 2012, The effect of mineralogy and effective normal stress on frictional strength of sheet silicates: Journal of Structural Geology, v. 42, p. 49-61.

Bürgmann, R., 2018, The geophysics, geology and mechanics of slow fault slip: Earth and Planetary Science Letters, v. 495, p. 112-134.

Calzolari, G., Ault, A. K., Hirth, G., and McDermott, R. G., 2020, Hematite (U-Th)/He thermochronometry detects asperity flash heating during laboratory earthquakes: Geology.

Carpenter, B., Saffer, D., and Marone, C., 2015, Frictional properties of the active San Andreas Fault at SAFOD: Implications for fault strength and slip behavior: Journal of Geophysical Research: Solid Earth, v. 120, no. 7, p. 5273-5289.

Chase, M., 1983, Heats of Transition of the Elements: Bull. Alloy Phase Diagrams, v. 4, no. 1, p. 124-124.

Collettini, C., Niemeijer, A., Viti, C., and Marone, C., 2009, Fault zone fabric and fault weakness: Nature, v. 462, no. 7275, p. 907-910.

Cornell, R. M., and Schwertmann, U., 2003, The iron oxides: structure, properties, reactions, occurrences and uses, John Wiley & Sons.

Di Toro, G., Goldsby, D. L., and Tullis, T. E., 2004, Friction falls toward zero in quartz rocks as slip velocity approaches seismic slip rates: Nature, v. 427, no. 6973, p. 436-439.

Di Toro, G., Han, R., Hirose, T., De Paola, N., Nielsen, S. B., Mizoguchi, K., Ferri, F., Cocco, M., and Shimamoto, T., 2011, Fault lubrication during earthquakes: Nature, v. 471, no. 7339, p. 494-498.

Dieterich, J. H., 1979, Modeling of rock friction: 1. Experimental results and constitutive equations: Journal of Geophysical Research: Solid Earth, v. 84, no. B5, p. 2161-2168.

DiMonte, A. A., Ault, A. K., Hirth, G., and Bradbury, K. K., in review, Hematite accommodates shallow, transient Pleistocene slow slip in the exhumed southern San Andreas fault system: submitted to Geology.

Fagereng, Å., and Beall, A., 2021, Is complex fault zone behaviour a reflection of rheological heterogeneity?: Philosophical Transactions of the Royal Society A, v. 379, no. 2193, p. 20190421.

Farley, K. A., 2018, Helium diffusion parameters of hematite from a single-diffusion-domain crystal: Geochimica et Cosmochimica Acta, v. 231, p. 117-129.

French, M. E., and Condit, C. B., 2019, Slip partitioning along an idealized subduction plate boundary at deep slow slip conditions: Earth and Planetary Science Letters, v. 528, p. 115828.

Goldsby, D. L., and Tullis, T. E., 2011, Flash heating leads to low frictional strength of crustal rocks at earthquake slip rates: Science, v. 334, p. 216-218.

Harris, R. A., 2017, Large earthquakes and creeping faults: Reviews of Geophysics, v. 55, no. 1, p. 169-198.

Horai, K. i., 1971, Thermal conductivity of rock-forming minerals: Journal of geophysical research, v. 76, no. 5, p. 1278-1308.

Ikari, M. J., 2019, Laboratory slow slip events in natural geological materials: Geophysical Journal International, v. 218, no. 1, p. 354-387.

Ikari, M. J., and Kopf, A. J., 2017, Seismic potential of weak, near-surface faults revealed at plate tectonic slip rates: Science advances, v. 3, no. 11, p. e1701269.

Ikari, M. J., Marone, C., and Saffer, D. M., 2011, On the relation between fault strength and frictional stability: Geology, v. 39, no. 1, p. 83-86.

Janecke, S. U., and Evans, J. P., 1988, Feldspar-influenced rock rheologies: Geology, v. 16, no. 12, p. 1064-1067.

Jensen, J. L., Reiners, P. W., Siddoway, C. S., Ault, A. K., Thomson, S. N., and Steele-MacInnis, M., 2018, Single-crystal hematite (U-Th)/He dates and fluid inclusions document Cryogenian seismic clastic injection in granite: Earth and Planetary Science Letters, v. 500, p. 145-155.

Jolivet, R., and Frank, W., 2020, The transient and intermittent nature of slow slip: AGU Advances, v. 1, no. 1, p. e2019AV000126.

Kaduri, M., Gratier, J. P., Renard, F., Çakir, Z., and Lasserre, C., 2017, The implications of fault zone transformation on aseismic creep: Example of the North Anatolian Fault, Turkey: Journal of Geophysical Research: Solid Earth, v. 122, no. 6, p. 4208-4236.

Kohli, A. H., Goldsby, D. L., Hirth, G., and Tullis, T., 2011, Flash weakening of serpentinite at near-seismic slip rates: Journal of Geophysical Research: Solid Earth, v. 116, no. B3.

Lachenbruch, A. H., 1986, Simple models for the estimation and measurement of frictional heating by an earthquake: U.S. Geological Survey Open File Report 86-508, p. 13 p.

Leeman, J., Marone, C., and Saffer, D., 2018, Frictional mechanics of slow earthquakes: Journal of Geophysical Research: Solid Earth, v. 123, no. 9, p. 7931-7949.

Leeman, J., Saffer, D., Scuderi, M., and Marone, C., 2016, Laboratory observations of slow earthquakes and the spectrum of tectonic fault slip modes: Nature communications, v. 7, no. 1, p. 1-6.

Linker, M., and Dieterich, J. H., 1992, Effects of variable normal stress on rock friction: Observations and constitutive equations: Journal of Geophysical Research: Solid Earth, v. 97, no. B4, p. 4923-4940.

Marone, C., 1997, On the rate of frictional healing and the constitutive law for time-and slip-dependent friction: International Journal of Rock Mechanics and Mining Sciences, v. 34, no. 3-4, p. 187. e181-187. e117.

-, 1998, Laboratory-derived friction laws and their application to seismic faulting: Annual Review of Earth and Planetary Sciences, v. 26, no. 1, p. 643-696.

McDermott, R. G., Ault, A. K., and Caine, J. S., 2021, Dating fault damage along the eastern Denali fault zone with hematite (U-Th)/He thermochronometry: Earth and Planetary Science Letters, v. 563, p. 116872.

McDermott, R. G., Ault, A. K., Evans, J. P., and Reiners, P. W., 2017, Thermochronometric and textural evidence for seismicity via asperity flash heating on exhumed hematite fault mirrors, Wasatch fault zone, UT, USA: Earth and Planetary Science Letters, v. 471, p. 85-93.

Moore, D. E., and Lockner, D. A., 2004, Crystallographic controls on the frictional behavior of dry and water-saturated sheet structure minerals: Journal of Geophysical Research: Solid Earth, v. 109, no. B3.

-, 2008, Talc friction in the temperature range 25–400 C: Relevance for fault-zone weakening: Tectonophysics, v. 449, no. 1-4, p. 120-132.

Moore, D. E., Lockner, D. A., and Hickman, S., 2016, Hydrothermal frictional strengths of rock and mineral samples relevant to the creeping section of the San Andreas Fault: Journal of Structural Geology, v. 89, p. 153-167.

Nesse, W. D., 2012, Introduction to mineralogy, v. 549 NES.

Odlum, M., Ault, A., Channer, M., and Calzolari, G., 2022, Seismicity recorded in hematite fault mirrors in the Rio Grande rift: Geosphere, v. 18, no. 1, p. 241-260.

Reiners, P. W., Chan, M. A., and Evenson, N. S., 2014, Radiogenic helium dating and chemistry of diagenetic Fe- and Mn-oxides in Mesozoic sandstones of the Colorado Plateau: Geological Society of America Bulletin, v. 126, no. 9-10, p. 1363-1383.

Romanet, P., Bhat, H. S., Jolivet, R., and Madariaga, R., 2018, Fast and slow slip events emerge due to fault geometrical complexity: Geophysical Research Letters, v. 45, no. 10, p. 4809-4819.

Rudnicki, J. W., and Chen, C. H., 1988, Stabilization of rapid frictional slip on a weakening fault by dilatant hardening: Journal of Geophysical Research: Solid Earth, v. 93, no. B5, p. 4745-4757.

Ruina, A., 1983, Slip instability and state variable friction laws: Journal of Geophysical Research: Solid Earth, v. 88, no. B12, p. 10359-10370.

Saffer, D. M., and Wallace, L. M., 2015, The frictional, hydrologic, metamorphic and thermal habitat of shallow slow earthquakes: Nature Geoscience, v. 8, no. 8, p. 594-600.

Sánchez-Roa, C., Faulkner, D., Boulton, C., Jimenez-Millan, J., and Nieto, F., 2017, How phyllosilicate mineral structure affects fault strength in Mg-rich fault systems: Geophysical Research Letters, v. 44, no. 11, p. 5457-5467.

Schleicher, A. M., van der Pluijm, B. A., and Warr, L. N., 2010, Nanocoatings of clay and creep of the San Andreas fault at Parkfield, California: Geology, v. 38, no. 7, p. 667-670.

Scholz, C. H., 2019, The mechanics of earthquakes and faulting, Cambridge university press.

Skarbek, R. M., Rempel, A. W., and Schmidt, D. A., 2012, Geologic heterogeneity can produce aseismic slip transients: Geophysical Research Letters, v. 39, no. 21.

Wei, M., Kaneko, Y., Liu, Y., and McGuire, J. J., 2013, Episodic fault creep events in California controlled by shallow frictional heterogeneity: Nature geoscience, v. 6, no. 7, p. 566-570.

Williams, R. T., Rowe, C. D., Okamoto, K., Savage, H. M., and Eves, E., 2021, How Fault Rocks Form and Evolve in the Shallow San Andreas Fault: Geochemistry, Geophysics, Geosystems, v. 22, no. 11, p. e2021GC010092.

Wintsch, R., Christoffersen, R., and Kronenberg, A., 1995, Fluid-rock reaction weakening of fault zones: Journal of Geophysical Research: Solid Earth, v. 100, no. B7, p. 13021-13032.

Xing, T., Zhu, W., French, M., and Belzer, B., 2019, Stabilizing effect of high pore fluid pressure on slip behaviors of gouge-bearing faults: Journal of Geophysical Research: Solid Earth, v. 124, no. 9, p. 9526-9545.

CHAPTER IV

SUMMARY AND CONCLUSIONS

This thesis utilizes observations from the rock record (Chapter II) and deformation experiments (Chapter III) to evaluate whether hematite accommodates shallow slow slip. In Chapter II, I present field, scanning electron microscopy (SEM), and (U-Th)/He thermochronometry data that show networks of hematite-coated faults in Mecca Hills initially formed from ~0.8 Ma to ~0.4 Ma at <1.5 km depth, potentially by fluid overpressure, and are reactivated by subseismic or slow slip. This work is innovative because it utilizes microtextures and hematite (U-Th)/He data patterns to document past transient slow slip in a shallowly exhumed fault and illustrates the fault slip processes that may operate at depth today in voluminous, basement-hosted fault zones.

In Chapter III, I present friction data, SEM, and hematite (U-Th)/He dates from slow slip deformation experiments to demonstrate that hematite is weak and exhibits primarily velocity-neutral to velocity-strengthening friction behavior. Coarse-grained specular hematite used in these experiments comminutes to form ultra-fine gouge. These gouge particles exhibit He loss along newly formed grain boundaries without temperature rise. The results of this collective research have implications for hematite (U-Th)/He thermochronometry, the geology of shallow hematite-bearing faults, and the mechanics of transient slow slip. These data imply hematite-bearing faults can accommodate shallow, transient slow slip without displaying thermally-induced He loss.

Some observations and interpretations from this research raise additional research questions. Future work will characterize spatial patterns of Mecca hematite (U-Th)/He

dates and further evaluate sources of error in these young dates. Hematite fault surfaces from within the Painted Canyon fault (PCF) zone and the Platform Block are commonly exposed near mixed hematite-clay surfaces and Mg-Fe clay gouge with minor hematite. Although these clay-rich surfaces cannot be dated using (U-Th)/He thermochronometry, they reflect evolving mechanical and fluid conditions, and likely play an important role in accommodating deformation in the PCF and San Andreas fault system more broadly. X-ray diffraction (XRD) will identify the clay mineral phases, SEM will characterize the microstructures, and deformation experiments will utilize mixed hematite-clay surfaces to evaluate how these surfaces formed and influenced subsequent deformation.

The main trace of the San Andreas Fault through Mecca Hills is delineated by a wide zone of red clay gouge with sandstone phacoids that also extends into low-angle en-echelon faults and appears along the SAF further to the south. The origin of this gouge and the type of deformation that it accommodated are enigmatic, but XRD, Ar or He thermochronometry, stable isotope analysis of clay, and deformation experiments will provide insight to potential hypotheses including if formation involved fluid or thermal alteration of sediments or clay smearing. These data can ultimately inform whether this gouge and other gouge in shallow continental fault systems accommodates aseismic creep or slow slip or propagates earthquakes to the near surface.

Additional potential avenues of research involve refining the cooling history of basement rocks in Mecca Hills to evaluate if existing apatite (U-Th)/He thermochronometry data patterns reflect solely exhumation following burial beneath Plio-Pleistocene sedimentary rocks (Moser et al., 2017) and/or hydrothermal fluid circulation. Detrital thermochronometry from these overlying sedimentary rocks could refine the

timing of the development of the basement-sediment nonconformity or thermal resetting by reburial. Hematite is commonly interlayered with calcite veins, and isotope or fluid inclusion thermometry could inform fluid temperatures to constrain potential partial resetting of hematite and apatite He dates from fault rocks and basement, respectively.

Hematite slow slip experiments were conducted using coarse-grained specular hematite, which is a different grain size and texture compared to the nanometer-scale, high-aspect ratio hematite platelets found in shallow faults such as the Mecca Hills (Chapter II) and the Eastern Denali fault zone (McDermott et al., 2021). Future deformation experiments will utilize gouge prepared from Mecca Hills hematite for deformation experiments to evaluate friction properties, and SEM will be used to evaluate textural and structural evolution. Comparison of these data with those from Chapter III will inform how grain size and morphology influences hematite fault behavior. Prior experiments (Chapter III, Calzolari et al., 2020) did not utilize the full spectrum of fault slip rates or normal stresses in these experiments. Future work will further constrain the effect of these different rates on hematite friction properties. To date, I have not evaluated how gouge formation and dilation influences slip localization and frictional behavior.

Finally, hematite (U-Th)/He dates provide an indirect observation of the process(es) of He loss from comminuted hematite gouge. Experiments, microscopy, and models will inform how He is lost following disaggregation or whether He can diffuse through the surface layers of a crystal lattice at low temperatures. Calculations will estimate the number of He atoms in a hematite gouge particle along the exposed surface and compare to the number of atoms in a hematite plate to quantify He loss.

REFERENCES

Calzolari, G., Ault, A. K., Hirth, G., and McDermott, R. G., 2020, Hematite (U-Th)/He thermochronometry detects asperity flash heating during laboratory earthquakes: Geology.

McDermott, R. G., Ault, A. K., and Caine, J. S., 2021, Dating fault damage along the eastern Denali fault zone with hematite (U-Th)/He thermochronometry: Earth and Planetary Science Letters, v. 563, p. 116872.

Moser, A. C., Evans, J. P., Ault, A. K., Janecke, S. U., and Bradbury, K. K., 2017, (U-Th)/He thermochronometry reveals Pleistocene punctuated deformation and synkinematic hematite mineralization in the Mecca Hills, southernmost San Andreas Fault zone: Earth and Planetary Science Letters, v. 476, p. 87-99.

APPENDIX A

Supporting Information for Chapter II

A1. Scanning electron microscopy and grain size analysis

Secondary electron (SE) and back-scattered electron (BSE) images, as well as energy dispersive spectroscopy (EDS) maps were acquired using a FEI Quanta FEG 650 field-emission scanning electron microscope (SEM) equipped with an Oxford EDS X-Max detector at Utah State University's Microscopy Core Facility. Hematite aliquots from samples listed in Table A1 were affixed onto 1/2" and 1" metal posts with double-sided Cu adhesive tape in plan (slip surface) view and in cross-section (Fig. A8). C-coated 1" ring epoxy mounts were prepared from cm-scale slip surface cross-sections of samples D20-3a, D20-3b, D20-3c, D20-3d, D20-4a/i, D20-4b/ii, D20-6a, D20-8a, and D20-8b (Fig. A4).

C-coated mounts were analyzed under high vacuum at pressures of $<5 \times 10^{-6}$ torr with 10-20 kV accelerating voltage, and ~9-12 mm working distance. Cu adhesive tape mounts were imaged in low vacuum mode at pressures of 0.08-0.53 torr, with an accelerating voltage of 10-20 kV, and ~9-12 mm working distance. Images were acquired at ~100-250,000x magnification.

Hematite plate-width measurements (n = 1567) were conducted using the xT Microscope Control software on images acquired at 75,000-125,000x magnifying power. The hematite He closure temperature (T_c) was calculated for each measurement assuming

Farley (2018) diffusion kinetics (E_a = 171 kJ/mol and $\ln(D_0)$ = -0.66), a spherical geometric factor, a cooling rate of 10 °C/Myr, and that the hematite plate half-width corresponds to the diffusion domain. Assuming an infinite plane sheet geometry increases the T_c values. Figure A7 presents histograms of hematite plate half-widths and calculated T_c.

A2. Hematite (U-Th)/He analytical methods

Hematite aliquots were selected for (U-Th)/He analysis at the Utah State University's Mineral Microscopy and Spectroscopy Lab. Sub-mm aliquots were isolated from slip surfaces using fine-point tweezers under a stereomicroscope. Aliquots were pre-screened using SEM (see above) prior to (U-Th)/He analysis to identify and analyze aliquots comprising solely hematite, and thus exclude aliquots containing interstitial phases (i.e., calcite, quartz, chlorite). Because SEM-prescreening yield exterior views of three-dimensional aliquots, some dated aliquots may contain minor amounts of these interstitial phases.

Pre-screened aliquots were analyzed for He, U, and Th contents at the Arizona Radiogenic Helium Dating Laboratory at the University of Arizona in two sessions (November 2020 and May 2021). We used analytical methods described in Reiners et al. (2014), with some differences owing to the nature of our aliquots. Aliquots were heated with a diode laser in an ultra-high vacuum gas extraction line. This line has been modified to include a charcoal-filled, cold finger submerged in liquid N to scavenge reactive gases from laser-heated aliquots *in vacuo* prior to spike addition. Owing to the ultra-fine grain size, packets were lased at temperatures of ~850-900 °C, associated with

a packet “very low glow” for 5 minutes. For most samples, a 3-minute gas re-extract was performed on the first aliquot per sample to confirm that measured $^{4}He/^{3}He$ ratios were at blank levels. Extracted He gas was spiked with ^{3}He, purified using cryogenic and gettering methods, and analyzed and measured on a quadrupole mass spectrometer. Analysis of a known quantity of ^{4}He was performed after every ~8 unknown analyses to monitor instrumental sensitivity drift. Each planchette of Fe-oxides is processed with several line blanks and hot blanks (on empty Nb packets) to constrain the $^{4}He/^{3}He$ ratios of unknown aliquots, together with $^{4}He/^{3}He$ ratios of ^{3}He shots. ^{4}He blanks from these procedures are ~0.05 fmol.

U and Th contents of each aliquot were measured by isotope dilution and solution ICPMS following the methods detailed in (Reiners, 2005). The degassed packets were dissolved in hydrochloric acid in a pressure digestion vessel (Parr bomb). Following addition of a ^{233}U-^{229}Th spike, equilibration, and dissolution, U and Th isotopes were measured on an Element 2 ICP-MS. The ^{233}U-^{229}Th spike contains 0.4-0.8 ng of ^{233}U and 0.6-1.2 ng of ^{229}Th. Example $^{238}U/^{233}U$ values of spike blanks and spike normals that accompanied each ICP-MS run are 0.00357 ± 0.00007 (± 1σ) and 1.27864 ± 0.004323 (± 1σ), respectively. Example $^{232}Th/^{229}Th$ values spike blanks and spike normals are 0.001575 ± 0.000073 (± 1σ) and 2.306317 ± 0.016291 (± 1σ), respectively. Typical background corrections for U and Th come from analysis of the same empty Nb tubes and are 0.001 ± 0.0001 ng U (± 1σ) and 0.0005 ± 0.0001 ng Th (± 1σ).

Blank corrected (U-Th)/He dates were calculated with propagated analytical uncertainties from U, Th, and He measurements. Hematite dates were determined assuming that the grains were unzoned in U and Th. Dates in Table A2 are not reported

with an F_t correction, assuming He implantation balances alpha (a)-ejection. Some samples with hematite slip surfaces have hematite preserved on both sides of the fault, and aliquots that were extracted from these surfaces are larger than the a-stopping distance.

A3. F_T correction to hematite (U-Th)/He dates

Within a polycrystalline hematite aliquot, alpha ejection is assumed to balance implantation between individual crystals within the mass, so we consider He loss from the aliquot to its surroundings. We explore the possibility of a-ejection from hematite aliquots through one side or both sides of the targeted material (Fig. A9, A10; Table A3). Calculations assume a Th/U ratio of 0.045 (average of the entire dataset), a weighted a stopping distance of 13.605 μm for U^{238} and U^{235}, an a stopping distance of 16.04 μm for Th^{232} (Ketcham et al., 2011), a uniform distribution of U and Th, and an aliquot width of 75 μm (lower range of observed aliquot widths). Evaluation of the F_T correction was implemented in a Python code (DR#), which performs n = 10,000,000 calculations that converge on an (1) F_t = 0.94, for a- ejection from only one side of the aliquot and, (2) F_t = 0.88, for a ejection from both sides of the aliquot. F_T-corrected dates do not change the overall interpretation of the data patterns.

A4. Discussion of hematite (U-Th)/He data outliers and secular disequilibrium

Aliquots analyzed for hematite (U-Th)/He thermochronometry are small volume, owing to efforts to target specific textures and pure hematite, and young. We report all analyses in Table A2, but do not discuss a subset (19%) of analyses in the main text with

analytical issues. These manifest as (1) low U content, (2) anomalously high Th/U ratios, and (3) low He content. We discuss these data and issues here.

First, aliquots 3cii-B4, 3di-A2, 4i-D1, 4ii-B4, 6aii-E1, 8ai-E4, 8aii-E1, and 17h-B4 yield U content that is lower compared to other aliquots from the same sample. We set a cutoff of a z-score <-1.25 for inclusion in the main text discussion. Samples with anomalously low U may have lost U during degassing. Second, aliquot 8ai-D3 has an anomalously high Th/U ratio (7.583) compared to aliquots within the sample and across the entire dataset, and U may have been lost during degassing (Hofmann et al., 2020; Vasconcelos et al., 2013). In general, we observe no positive *intrasample* trends between hematite He date and Th/U that would reflect U loss (Fig. A11). Third, aliquot 18ci-A2 yields anomalously low He content both within the sample and across the dataset, suggesting that He extraction during degassing was incomplete. In addition, we do not discuss aliquot 8ai-C6 because it was the only aliquot without analytical issues for sample 8ai. To do so would place significance on an individual analysis, which is not standard practice in (U-Th)/He thermochronometry. Finally, the (U-Th)/He date for 8aii-C2 is not discussed because it a notable outlier for the sample, but the cause of analytical dispersion is unknown.

Secular disequilibrium due to chemical fractionation within the ^{238}U decay series impacts the He ingrowth rate in minerals with crystallization ages <1 Ma. [^{234}U/^{238}U] and [^{230}Th/^{238}U] activity ratios that are >1 and <1 cause (U-Th)/He dates to be older than or younger than the “true age,” respectively, provided dates record formation and not cooling. Although we lack [^{234}U/^{238}U] and [^{230}Th/^{238}U] activity ratios for our dataset, it is likely that, for aliquots with (U-Th)/He dates >400 ka, low Th/U, and low U

concentration, the error associated with our individual analyses is <±15% (Farley et al., 2002). This error overlaps in part with calculated sample standard deviations from dates that record formation ages, which range from 4-15% (Table A1). Consideration of the worst-case scenario does not influence the overall interpretation of our hematite He dates as mineralization dates. Because analytical error due to secular disequilibrium is larger with younger dates and exceeds the maximum percent standard deviation, we do not discuss three aliquots (26a-A1, 26bii-F3, and 20a-A1) in the main text with dates <<0.30 Ma.

REFERENCES

Farley, K. A., 2018, Helium diffusion parameters of hematite from a single-diffusion-domain crystal: Geochimica et Cosmochimica Acta, v. 231, p. 117-129.

Hofmann, F., Treffkorn, J., and Farley, K. A., 2020, U-loss associated with laser-heating of hematite and goethite in vacuum during (U–Th)/He dating and prevention using high O2 partial pressure: Chemical Geology, v. 532, p. 119350.

Ketcham, R. A., Gautheron, C., and Tassan-Got, L., 2011, Accounting for long alpha-particle stopping distances in (U-Th-Sm)/He geochronology: refinement of the baseline case: Geochimica et Cosmochimica Acta, v. 75, p. 7779-7791.

Reiners, P. W., 2005, Zircon (U-Th)/He thermochronometry: Reviews in Mineralogy and Geochemistry, v. 58, p. 151-179.

Reiners, P. W., Chan, M. A., and Evenson, N. S., 2014, Radiogenic helium dating and chemistry of diagenetic Fe- and Mn-oxides in Mesozoic sandstones of the

Colorado Plateau: Geological Society of America Bulletin, v. 126, no. 9-10, p. 1363-1383.

Vasconcelos, P. M., Heim, J. A., Farley, K. A., Monteiro, H., and Waltenberg, K., 2013, $^{40}Ar/^{39}Ar$ and (U-Th)/He - $^{4}He/^{3}He$ geochronology of landscape evolution and channel iron deposits genesis at Lynn Peak, Western Australia: Geochimica et Cosmochimica Acta, v. 117, p. 283-312.

Table A1. Sample information and locations with samples analyzed for (U-Th)/He hematite thermochronometry and included in main text highlighted.

Sample	*Type*[a]	*SEM ID*	*Hem He?*	*SEM?*	*Slip Surface*	*Slickenline*	*GPS Location*	*Elevation*
D20-1a	hematite *ss*				047/55	46-->181	33.63353, -115.99178	182 m
D20-2	basement						33.63087, -115.99118	301 m
D20-3a	hematite *ss*		x	x	102/85	curved	33.61606, -115.99806	177 m
D20-3b	hem/clay *ss*			x	129/66	30NW	33.61606, -115.99806	177 m
D20-3c	hematite *ss*		x	x	135/54	90SE (dip)	33.61606, -115.99806	177 m
D20-3d	hematite *ss*		x	x			33.61606, -115.99806	177 m
D20-3e	silica *ss*						33.61606, -115.99806	177 m
D20-4a		D20-4i	x	x	105/15, 205/56,			
D20-4b	hematite *ss*	D20-4ii	x	x	181/27,	14-->205	33.61622, -115.99790	166 m
D20-4c		D20-4iii		x	151/66, 244/90			
D20-5	hematite *ss*				143/27		33.61508, -115.99854	320 m
D20-6a	hematite *ss*		x	x	255/77	43SE	33.61684, -115.99954	181 m
D20-6b	hematite *ss*				285/38		33.61684, -115.99954	181 m
D20-6c	hematite *ss*						33.61684, -115.99954	181 m
D20-6d	hematite *ss*						33.61684, -115.99954	181 m
D20-6e	hematite *ss*						33.61684, -115.99954	181 m
D20-7	gouge				253/42, 224/46		33.61634, -115.99943	177 m
D20-8a	hematite *ss*		x	x	137/79		33.61498, -116.00181	127 m
D20-8b	hematite *ss*		x	x			33.61498, -116.00181	127 m
D20-9	paly *ss*							
D20-10a	hematite *ss*						33.61627, -115.99769	159 m
D20-10b	gouge						33.61627, -115.99769	159 m
D20-10c	clay				328/74, 324/71		33.61627, -115.99769	159 m
D20-10d	hem/clay *ss*				256/53		33.61627, -115.99769	159 m
D20-12a	hem *ss*						33.61639, -115.99781	178 m
D20-12b	hem/clay *ss*						33.61639, -115.99781	178 m
D20-12c	basement						33.61639, -115.99781	178 m
D20-13	hem/clay *ss*						33.61634, -115.99814	181 m
D20-14	clay						33.61605, -115.99803	168 m

Table A1 (continued).

Sample	*Type*[a]	*SEM ID*	*Hem He?*	*SEM?*	*Slip Surface*	*Slickenline*	*GPS Location*	*Elevation*
D20-15A	clay				290/87		33.61590, -115.99881	163 m
D20-15b	cat/gouge				308/78		33.61590, -115.99881	163 m
D20-16	hematite ss						33.61608, -115.99881	165 m
D20-17a-h	hematite ss		x	x	245/88		33.61627, -115.99848	177 m
D20-18a	breccia						33.61678, -115.9940	185 m
D20-18b	gouge						33.61678, -115.9940	185 m
D20-18c	hematite ss	D20-18ci	x	x			33.61678, -115.9940	185 m
D20-18d		D20-18cii	x	x				
D20-19a	hematite ss						33.61670, -116.00082	214 m
D20-19b	alt volc						33.61670, -116.00082	214 m
D20-20a	hematite ss		x	x			33.61957, -116.05000	315 m
D20-20b	breccia						33.61957, -116.05000	315 m
D20-22a	alt volc						33.61522, -116.00076	129 m
D20-22b	clay						33.61522, -116.00076	129 m
D20-22c	red clay				043/35	30-->133	33.61522, -116.00076	129 m
D20-22d	hematite ss						33.61522, -116.00076	129 m
D20-23a	gr/black surf				023/81, 001/84		33.61516, -116.00077	178 m
D20-23b	hem/chlor ss						33.61516, -116.00077	178 m
D20-23c	hem/chlor ss						33.61516, -116.00077	178 m
D20-24	hematite ss						33.61588, -116.00329	190 m
D20-25a	hematite ss				111/78, 092/63		33.62817, -115.98956	345 m
D20-25b	mix hem/clay						33.62817, -115.98956	345 m
D20-26a	hematite ss		x	x			33.62940, -115.98999	267 m
D20-26b	hematite ss	D20-26bii	x	x			33.62940, -115.98999	267 m

[a]ss = slip surfaces. basement = crystaline basement, hem = hematite, paly = palygorskite, cat = cataclasite, alt volc = altered crystalline rock, gr/black surf = joint surface with green-black mineral, chlor = chlorite

Table A2. Hematite (U-Th)/He thermochronometry data.

Sample	U (ng)	± 1σ	z U	Th (ng)	± 1σ	Th/U	He (fmol)	± 1σ	Date (Ma)	2σ (Ma)
D20-3a-A3	0.460	0.0067	-1.003	0.003	0.0001	0.007	1.551	0.051	0.63	0.04
D20-3a-B2	1.226	0.0175	1.016	0.005	0.0001	0.004	3.773	0.060	0.57	0.02
D20-3a-C2	1.346	0.0193	1.332	0.006	0.0001	0.004	4.198	0.057	0.58	0.02
D20-3a-D4	0.728	0.0104	-0.297	0.003	0.0001	0.004	2.489	0.048	0.63	0.03
D20-3a-D1	0.443	0.0064	-1.048	0.003	0.0001	0.007	1.631	0.049	0.68	0.05
								Mean	**0.62**	
								Std. Dev	**0.04**	**7%**
D20-3cii-A2	0.334	0.0049	0.484	0.022	0.0003	0.068	0.965	0.051	0.53	0.06
D20-3cii-B2	0.386	0.0080	1.053	0.034	0.0008	0.091	0.902	0.044	0.42	0.04
[a]D20-3cii-B4	0.167	0.0024	-1.344	0.004	0.0001	0.024	0.894	0.043	0.99	0.10
D20-3cii-C2	0.369	0.0053	0.861	0.007	0.0001	0.020	0.840	0.046	0.42	0.05
D20-3cii-D2	0.193	0.0028	-1.054	0.002	0.0001	0.012	0.628	0.041	0.60	0.08
								Mean	**0.49**	
								Std. Dev	**0.08**	**15%**
D20-3di-A1	0.464	0.0067	1.669	0.012	0.0002	0.026	1.828	0.051	0.73	0.04
D20-3di-A2	0.200	0.0029	-1.328	0.004	0.0001	0.021	0.618	0.047	0.57	0.09
D20-3di-B1	0.333	0.0048	0.174	0.004	0.0001	0.012	1.086	0.048	0.60	0.06
D20-3di-B5	0.328	0.0047	0.123	0.007	0.0001	0.021	1.215	0.052	0.68	0.06
D20-3di-C3	0.261	0.0038	-0.638	0.019	0.0003	0.075	0.825	0.044	0.58	0.06
D20-3dii-B1	0.632	0.0090	-0.276	0.011	0.0002	0.017	2.373	0.053	0.69	0.04
D20-3dii-C2	1.409	0.0202	1.688	0.007	0.0002	0.005	6.655	0.063	0.88	0.03
D20-3dii-E4	0.384	0.0057	-0.903	0.005	0.0001	0.013	1.373	0.022	0.66	0.03
D20-3dii-F1	0.539	0.0078	-0.510	0.005	0.0001	0.009	2.165	0.040	0.74	0.03
								Mean	**0.70**	
								Std. Dev	**0.09**	**12%**
D20-4a-C1	0.901	0.0130	1.320	0.009	0.0001	0.010	3.661	0.053	0.75	0.03
D20-4a-D1	0.233	0.0034	-1.478	0.004	0.0001	0.017	0.848	0.023	0.67	0.04
D20-4a-D5	0.646	0.0093	0.254	0.015	0.0003	0.024	2.339	0.040	0.67	0.03
D20-4a-D6	0.562	0.0081	-0.097	0.006	0.0001	0.010	2.160	0.041	0.71	0.03
								Mean	**0.71**	
								Std. Dev	**0.03**	**5%**
D20-4b-A5	0.405	0.0058	1.240	0.009	0.0002	0.024	1.477	0.038	0.67	0.04
D20-4b-B4	0.248	0.0036	-1.521	0.024	0.0004	0.101	1.358	0.031	0.99	0.05
D20-4b-B7	0.329	0.0047	-0.093	0.050	0.0007	0.154	1.123	0.033	0.61	0.04
D20-4b-C5	0.356	0.0052	0.374	0.012	0.0002	0.035	0.902	0.037	0.47	0.04
								Mean	**0.58**	
								Std. Dev	**0.09**	**15%**

Table A2 (continued).

Sample	U (ng)	± 1σ	z U	Th (ng)	± 1σ	Th/U	He (fmol)	± 1σ	Date (Ma)	2σ (Ma)
D20-6aii-B4	0.414	0.0059	0.339	0.046	0.0007	0.113	2.622	0.042	1.15	0.05
D20-6aii-C2	0.380	0.0055	0.110	0.041	0.0007	0.112	2.079	0.037	0.99	0.04
D20-6aii-C4	0.535	0.0078	1.149	0.082	0.0012	0.158	3.636	0.056	1.22	0.05
D20-6aii-E1	0.124	0.0018	-1.598	0.036	0.0006	0.303	0.771	0.034	1.08	0.10
D20-6aiii-C1	0.822	0.0118	1.528	0.025	0.0004	0.032	9.900	0.120	2.22	0.08
D20-6aiii-C4	0.291	0.0042	-1.055	0.016	0.0003	0.058	2.217	0.032	1.40	0.06
D20-6aiii-D1	0.556	0.0080	0.234	0.031	0.0004	0.057	4.159	0.058	1.37	0.05
D20-6aiii-D4	0.362	0.0052	-0.706	0.028	0.0005	0.079	2.938	0.047	1.48	0.06
								Mean	**1.40**	
								Std. Dev	**0.37**	**26%**
D20-8ai-C6	0.142	0.0021	0.088	0.009	0.0001	0.066	0.744	0.029	0.96	0.08
D20-8ai-D3	0.189	0.0028	1.178	1.398	0.0200	7.583	2.377	0.040	0.85	0.03
D20-8ai-E4	0.082	0.0012	-1.266	0.007	0.0002	0.082	0.611	0.027	1.35	0.13
D20-8aii-C2	0.365	0.0052	0.690	0.013	0.0002	0.038	0.620	0.026	0.31	0.03
D20-8aii-E1	0.273	0.0039	-1.612	0.004	0.0001	0.016	1.083	0.024	0.73	0.04
D20-8aii-E2	0.336	0.0049	-0.039	0.021	0.0003	0.065	1.464	0.034	0.80	0.04
D20-8aii-E4	0.375	0.0054	0.961	0.005	0.0001	0.014	1.603	0.043	0.79	0.05
								Mean	**0.79**	
								Std. Dev	**0.00**	**0.5%**
D20-8b-B4	0.651	0.0094	-0.528	0.061	0.0009	0.096	3.177	0.051	0.89	0.04
D20-8b-D5	0.919	0.0131	0.191	0.188	0.0027	0.210	3.603	0.060	0.69	0.03
D20-8b-F1	0.427	0.0061	-1.127	0.006	0.0001	0.015	1.539	0.039	0.67	0.04
D20-8b-C1	0.717	0.0103	-0.351	0.019	0.0003	0.027	2.430	0.047	0.63	0.03
D20-8b-C6	1.526	0.0221	1.815	0.049	0.0007	0.033	5.377	0.038	0.65	0.02
								Mean	**0.70**	
								Std. Dev	**0.09**	**13%**
D20-17g-B4	0.305	0.0045	1.299	0.005	0.0002	0.016	0.785	0.022	0.48	0.03
D20-17g-C4	0.194	0.0028	-0.166	0.004	0.0001	0.019	0.550	0.021	0.53	0.04
D20-17g-D2	0.120	0.0018	-1.133	0.002	0.0001	0.019	0.275	0.018	0.42	0.06
								Mean	**0.48**	
								Std. Dev	**0.04**	**9%**

TableA2 (continued).

Sample	U (ng)	± 1σ	z U	Th (ng)	± 1σ	Th/U	He (fmol)	± 1σ	Date (Ma)	2σ (Ma)
D20-17h-A3	0.815	0.0119	1.031	0.026	0.0004	0.033	2.404	0.029	0.54	0.02
D20-17h-B2	0.713	0.0104	0.552	0.011	0.0002	0.017	1.674	0.028	0.43	0.02
D20-17h-B3	0.683	0.0100	0.410	0.008	0.0002	0.012	1.878	0.019	0.51	0.02
D20-17h-B4	0.159	0.0024	-2.051	0.004	0.0001	0.025	0.396	0.016	0.46	0.04
D20-17h-C2	0.526	0.0078	-0.328	0.003	0.0001	0.005	1.481	0.020	0.52	0.02
D20-17h-C4	0.678	0.0099	0.386	0.008	0.0002	0.012	1.803	0.022	0.49	0.02
								Mean	**0.50**	
								Std. Dev	**0.04**	**7%**
D20-18c-A1	0.592	0.0086	-0.638	0.011	0.0002	0.019	1.987	0.025	0.62	0.02
D20-18c-A2	0.920	0.0136	0.759	0.013	0.0003	0.015	1.614	0.026	0.32	0.01
D20-18c-B1	0.517	0.0076	-0.956	0.056	0.0009	0.111	2.021	0.030	0.71	0.03
D20-18c-B2	0.564	0.0084	-0.756	0.030	0.0005	0.054	1.917	0.041	0.62	0.03
D20-18c-C3	1.116	0.0162	1.591	0.016	0.0003	0.015	3.640	0.040	0.60	0.02
								Mean	**0.64**	
								Std. Dev	**0.04**	**6%**
D20-18d-C4	0.515	0.0076	-1.026	0.011	0.0002	0.022	1.750	0.030	0.63	0.03
D20-18d-D4	0.826	0.0120	0.463	0.025	0.0004	0.031	3.008	0.044	0.67	0.03
D20-18d-Z1	1.025	0.0149	1.416	0.016	0.0003	0.016	2.901	0.048	0.52	0.02
D20-18d-Z2	0.551	0.0080	-0.853	0.008	0.0001	0.015	1.620	0.032	0.54	0.03
								Mean	**0.59**	
								Std. Dev	**0.06**	**10%**
D20-20a-A1	2.554	0.0438	1.902	0.094	0.0014	0.038	1.664	0.038	0.12	0.01
D20-20a-B4	0.686	0.0100	-1.017	0.008	0.0002	0.012	1.868	0.038	0.50	0.02
D20-20a-C3	1.303	0.0191	-0.054	0.016	0.0003	0.013	3.076	0.045	0.44	0.02
D20-20a-D2	1.067	0.0156	-0.422	0.014	0.0002	0.014	2.208	0.037	0.38	0.02
D20-20a-D4	1.075	0.0156	-0.409	0.135	0.0020	0.129	2.371	0.039	0.40	0.02
								Mean	**0.43**	
								Std. Dev	**0.05**	**11%**
D20-26a-A1	0.238	0.0035	-1.082	0.052	0.0008	0.225	0.317	0.008	0.23	0.01
D20-26a-B1	0.820	0.0119	-0.457	0.035	0.0006	0.044	1.474	0.020	0.33	0.01
D20-26a-B2	1.062	0.0154	-0.197	0.023	0.0005	0.022	2.711	0.037	0.47	0.02
D20-26a-C2	1.104	0.0159	-0.151	0.025	0.0004	0.023	2.663	0.032	0.45	0.02
D20-26a-D2	3.000	0.0173	1.887	0.059	0.0009	0.051	2.815	0.041	0.43	0.02
								Mean	**0.42**	
								Std. Dev	**0.05**	**13%**

Table A2 (continued).

Sample	U (ng)	± 1σ	z U	Th (ng)	± 1σ	Th/U	He (fmol)	± 1σ	Date (Ma)	2σ (Ma)
D20-26b-B4	0.651	0.0097	-0.320	0.007	0.0001	0.011	1.258	0.026	0.36	0.02
D20-26b-C3	2.527	0.0367	1.709	0.027	0.0004	0.011	4.723	0.024	0.35	0.01
D20-26b-E5	0.382	0.0057	-0.612	0.008	0.0001	0.021	0.793	0.012	0.38	0.02
D20-26b-F3	0.229	0.0033	-0.777	0.008	0.0002	0.036	0.315	0.013	0.25	0.02
								Mean	**0.36**	
								Std. Dev	**0.02**	**4%**

[a]Blue samples are outlier analyses that are not included in the geometric mean calculation. See text A4 for discussion of outlier analyses.

Table A3. F_T-corrected hematite (U-Th)/He dates. See text A3 for discussion.

Sample	Raw Date (Ma)	Ejected from one side ($F_T = 0.94$) Date (Ma)	Δ Date (Ma)[a]	Ejected from both sides ($F_T = 0.88$) Date (Ma)	Δ Date (Ma)[a]
D20-3a-A3	0.63	0.67	0.04	0.71	0.09
D20-3a-B2	0.57	0.61	0.04	0.65	0.08
D20-3a-C2	0.58	0.62	0.04	0.66	0.08
D20-3a-D4	0.63	0.68	0.04	0.72	0.09
D20-3a-D1	0.68	0.73	0.04	0.78	0.09
D20-3cii-A2	0.53	0.56	0.03	0.60	0.07
D20-3cii-B2	0.42	0.45	0.03	0.48	0.06
D20-3cii-C2	0.42	0.45	0.03	0.48	0.06
D20-3cii-D2	0.60	0.64	0.04	0.68	0.08
D20-3di-A1	0.73	0.77	0.05	0.83	0.10
D20-3di-B1	0.60	0.64	0.04	0.69	0.08
D20-3di-B5	0.68	0.73	0.04	0.78	0.09
D20-3di-C3	0.58	0.61	0.04	0.66	0.08
D20-3dii-B1	0.69	0.74	0.04	0.79	0.09
D20-3dii-C2	0.88	0.93	0.06	1.00	0.12
D20-3dii-E4	0.66	0.70	0.04	0.75	0.09
D20-3dii-F1	0.74	0.79	0.05	0.85	0.10
D20-4a-C1	0.75	0.80	0.05	0.86	0.10
D20-4a-D5	0.67	0.71	0.04	0.76	0.09
D20-4a-D6	0.71	0.76	0.05	0.81	0.10
D20-4b-A5	0.67	0.72	0.04	0.77	0.09
D20-4b-B7	0.61	0.65	0.04	0.70	0.08
D20-4b-C5	0.47	0.50	0.03	0.53	0.06
D20-6aii-B4	1.15	1.22	0.07	1.30	0.16
D20-6aii-C2	0.99	1.05	0.06	1.13	0.14
D20-6aii-C4	1.22	1.29	0.08	1.38	0.17
D20-6aiii-C1	2.22	2.36	0.14	2.52	0.30
D20-6aiii-C4	1.40	1.49	0.09	1.59	0.19
D20-6aiii-D1	1.37	1.46	0.09	1.56	0.19
D20-6aiii-D4	1.48	1.57	0.09	1.68	0.20
D20-8aii-E2	0.80	0.85	0.05	0.91	0.11
D20-8aii-E4	0.79	0.84	0.05	0.90	0.11

Table A3 (continued).

Sample	Raw Date (Ma)	Ejected from one side ($F_T = 0.94$) Date (Ma)	Δ Date (Ma)[a]	Ejected from both sides ($F_T = 0.88$) Date (Ma)	Δ Date (Ma)[a]
D20-8b-B4	0.89	0.94	0.06	1.01	0.12
D20-8b-D5	0.69	0.74	0.04	0.79	0.09
D20-8b-F1	0.67	0.71	0.04	0.76	0.09
D20-8b-C1	0.63	0.67	0.04	0.71	0.09
D20-8b-C6	0.65	0.69	0.04	0.74	0.09
D20-20a-B4	0.50	0.54	0.03	0.57	0.07
D20-20a-C3	0.44	0.47	0.03	0.50	0.06
D20-20a-D2	0.38	0.41	0.02	0.44	0.05
D20-20a-D4	0.40	0.42	0.03	0.45	0.05
D20-17g-B4	0.48	0.51	0.03	0.54	0.06
D20-17g-C4	0.53	0.56	0.03	0.60	0.07
D20-17g-D2	0.42	0.45	0.03	0.48	0.06
D20-17h-A3	0.54	0.58	0.03	0.62	0.07
D20-17h-B2	0.43	0.46	0.03	0.49	0.06
D20-17h-B3	0.51	0.54	0.03	0.58	0.07
D20-17h-C2	0.52	0.56	0.03	0.59	0.07
D20-17h-C4	0.49	0.52	0.03	0.56	0.07
D20-18c-A1	0.62	0.66	0.04	0.71	0.08
D20-18c-B1	0.71	0.75	0.05	0.80	0.10
D20-18c-B2	0.62	0.66	0.04	0.71	0.09
D20-18c-C3	0.60	0.64	0.04	0.69	0.08
D20-18d-C4	0.63	0.67	0.04	0.71	0.09
D20-18d-D4	0.67	0.71	0.04	0.76	0.09
D20-18d-Z1	0.52	0.56	0.03	0.60	0.07
D20-18d-Z2	0.54	0.58	0.03	0.62	0.07
D20-26a-B1	0.33	0.35	0.02	0.38	0.05
D20-26a-B2	0.47	0.50	0.03	0.54	0.06
D20-26a-C2	0.45	0.47	0.03	0.51	0.06
D20-26a-D2	0.43	0.46	0.03	0.49	0.06
D20-26b-B4	0.36	0.38	0.02	0.41	0.05
D20-26b-C3	0.35	0.37	0.02	0.39	0.05
D20-26b-E5	0.38	0.41	0.02	0.44	0.05

[a]Δ = increase in date (Ma) after applying F_T correction

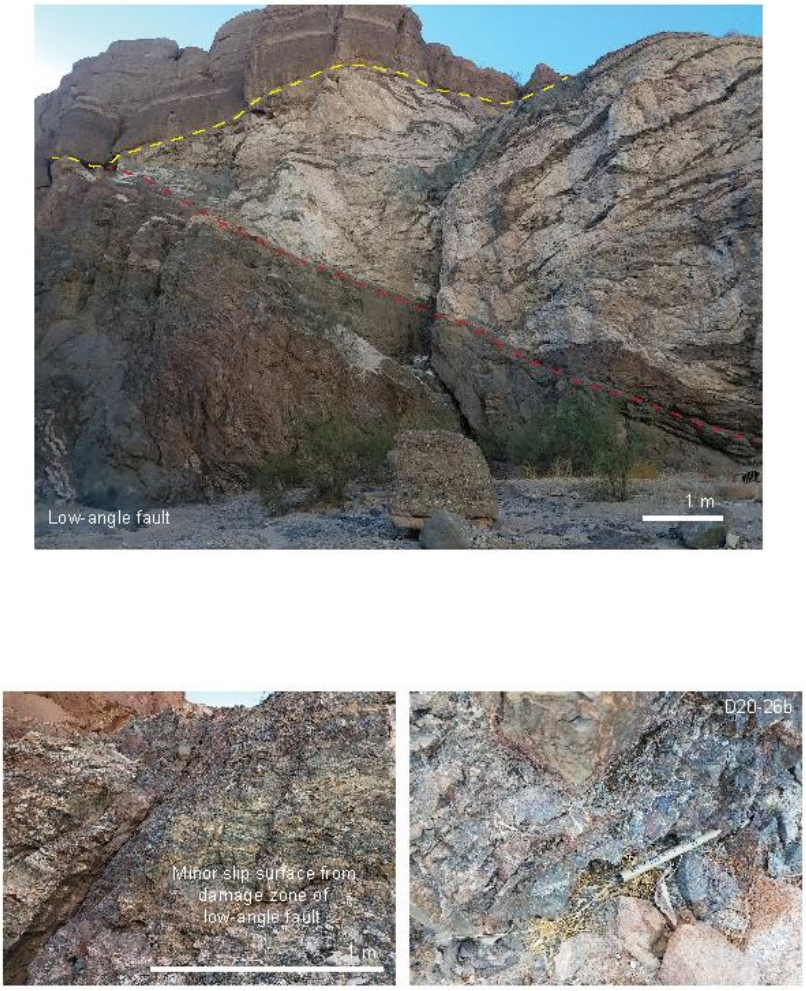

Figure A1. Map-scale low-angle fault cutting basement rock in Platform block. Dashed red line = fault surface. Dashed yellow line = basement-Pleistocene sediment nonconformity. Associated damage zone structures including minor fault (lower left) and hematite-coated slip surface (lower right.)

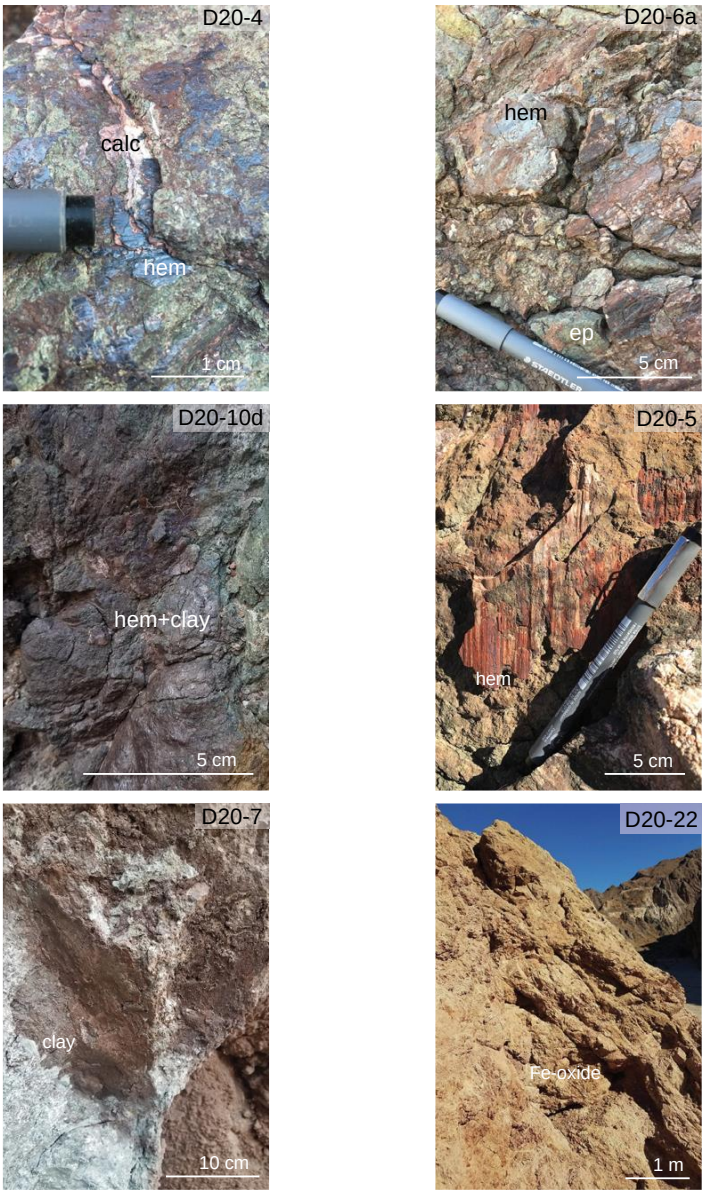

Figure A2. Field photographs of selected sample locations. calc = calcite, hem = hematite, ep = epidote.

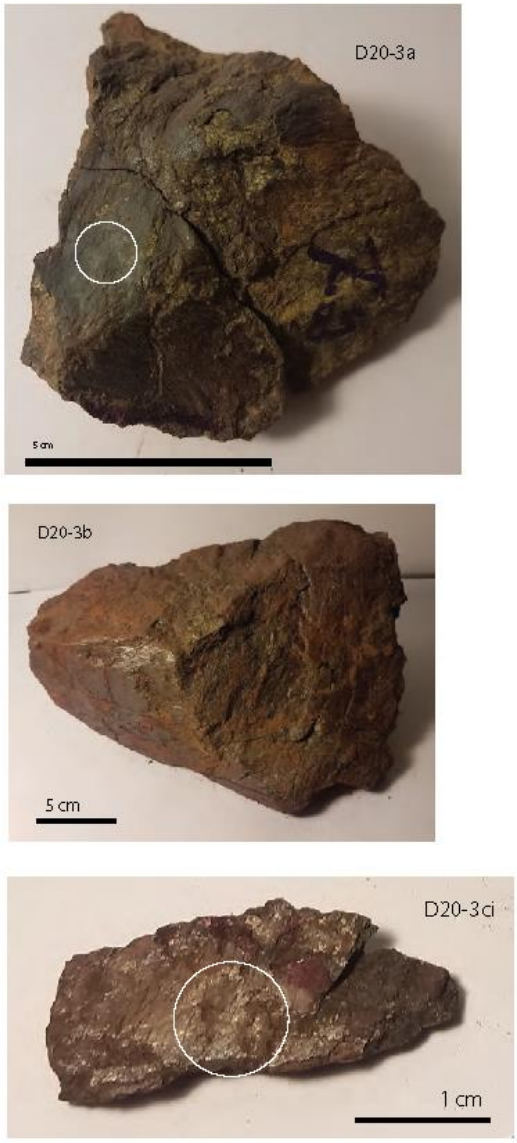

Figure A3. Hand sample photographs. Circles identify target locations for aliquots for thermochronometry and microscopy.

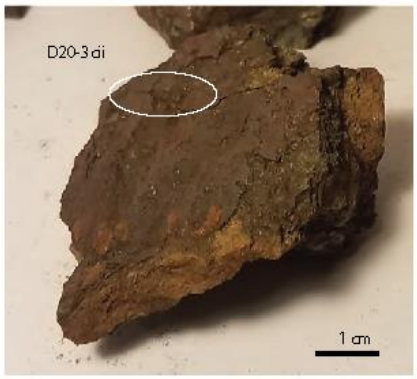

Figure A3 (continued).

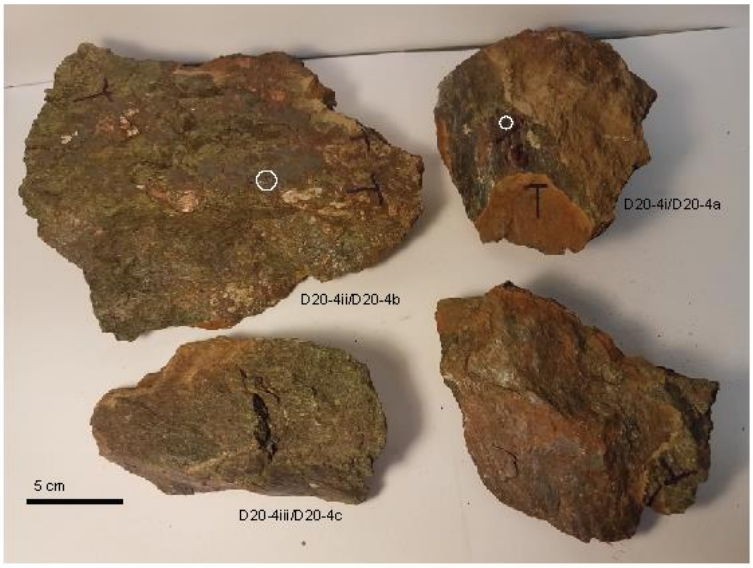

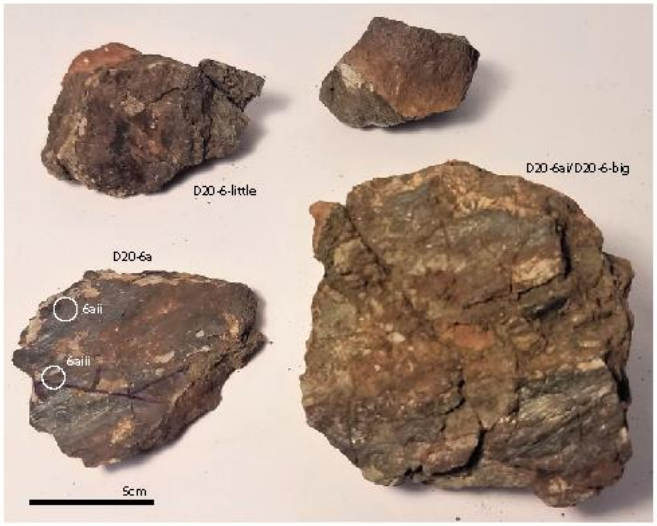

Figure A3 (continued).

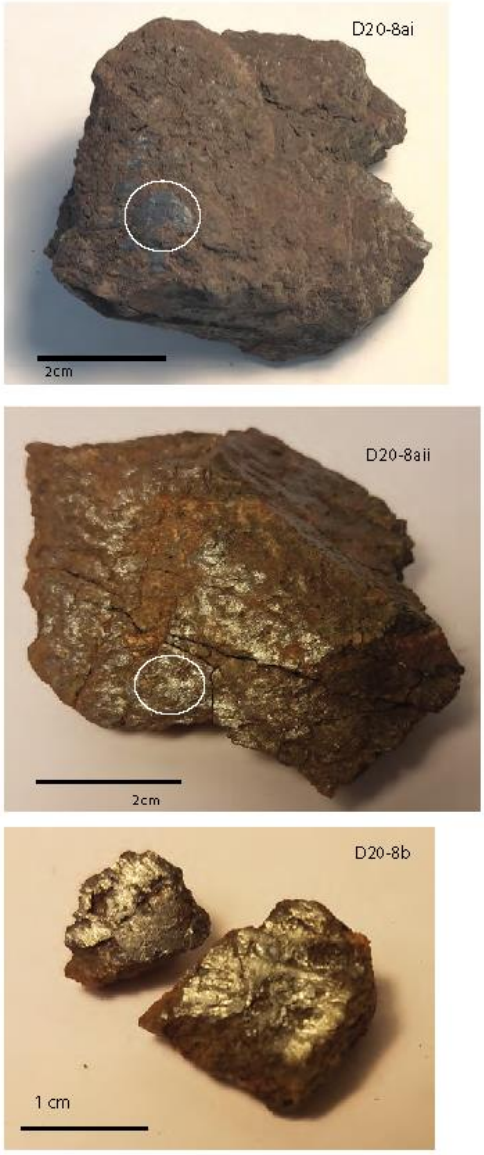

Figure A3 (continued).

Figure A3 (continued).

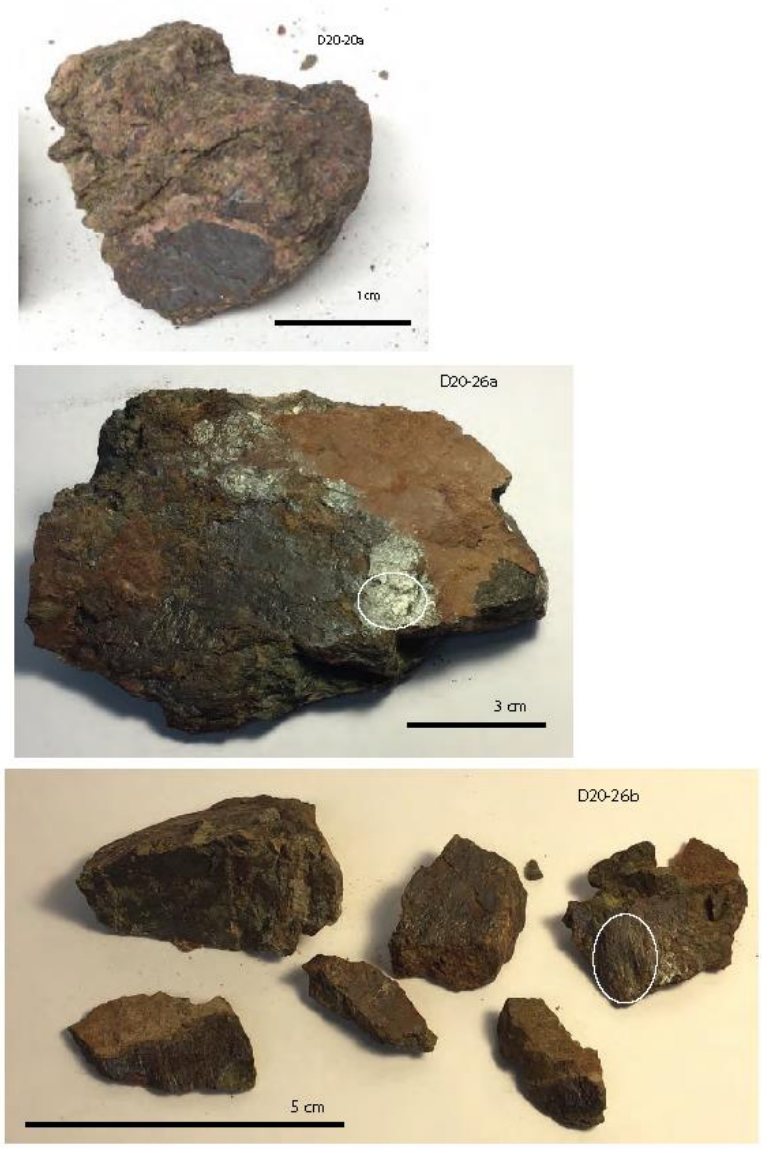

Figure A3 (continued).

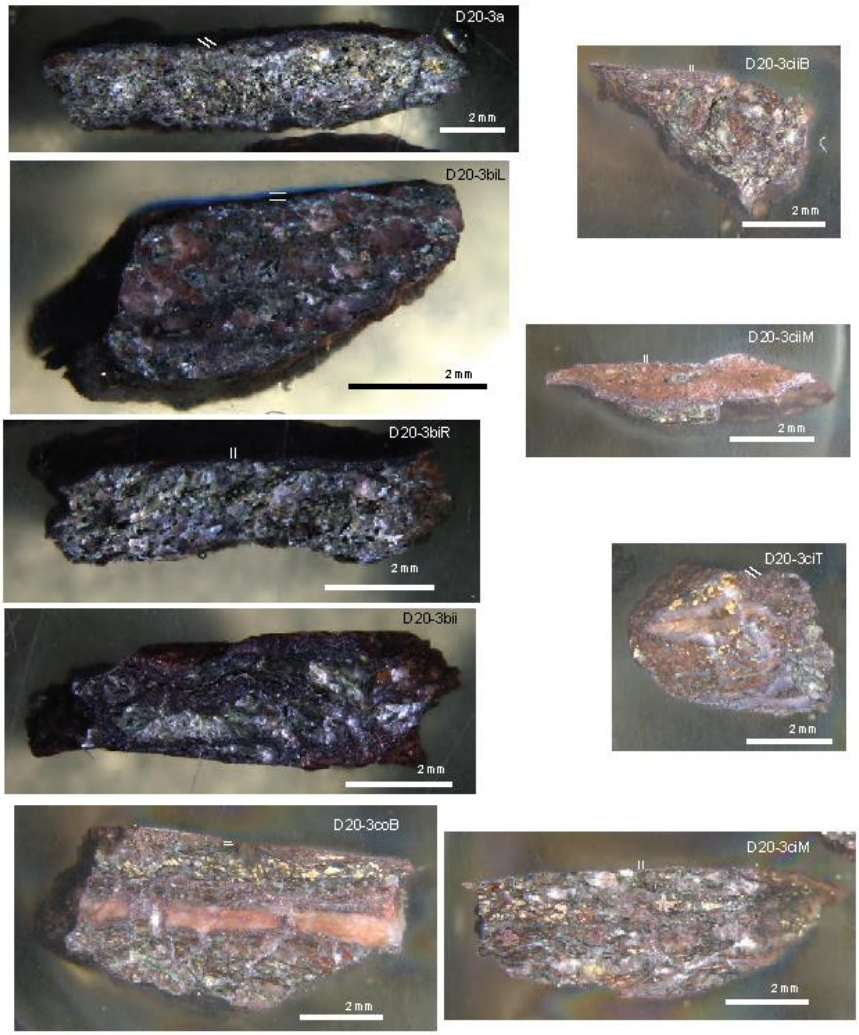

Figure A4. Photographs of sample chips in SEM epoxy mounts.

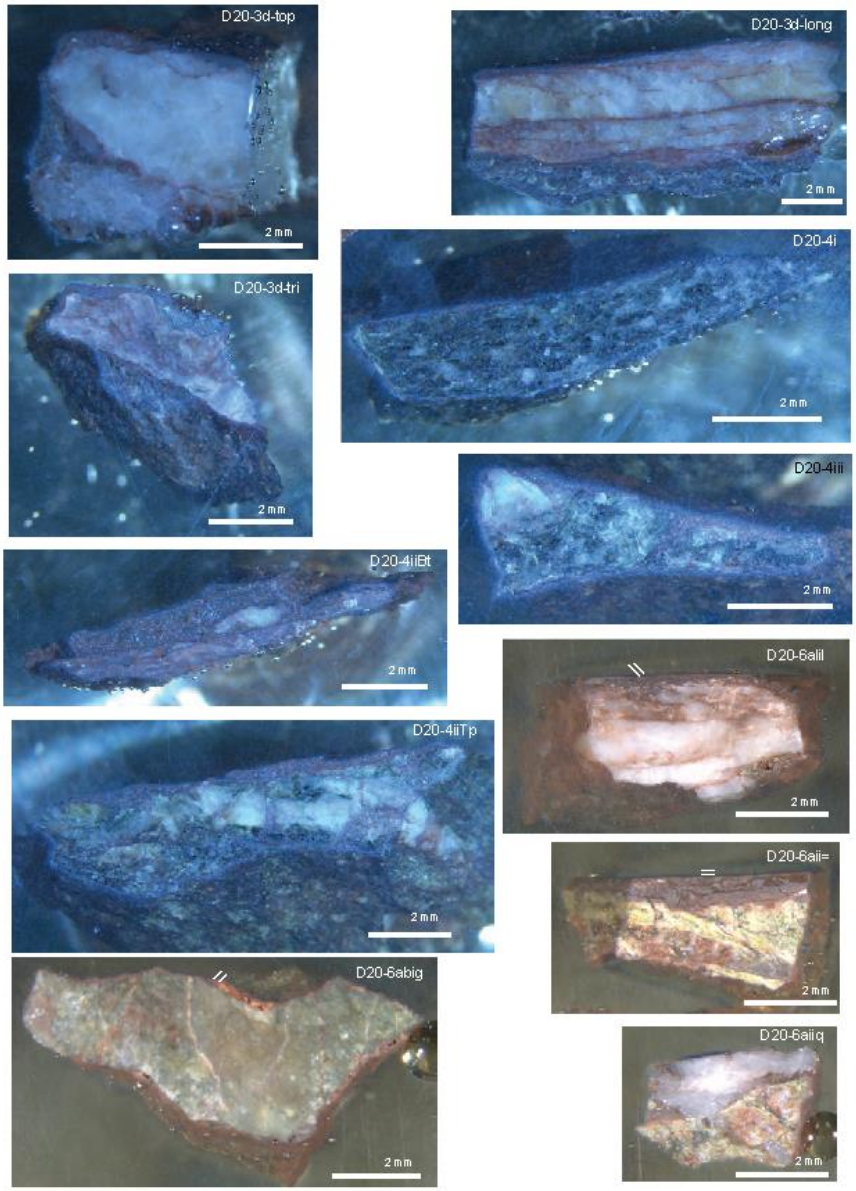

Figure A4 (continued)

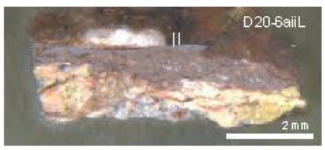

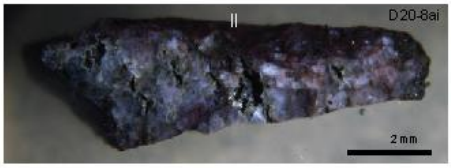

Figure A4 (continued).

Interlayered veins

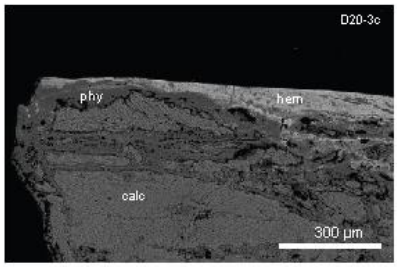

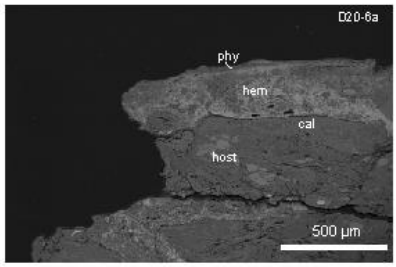

Other samples - 3b, 4a, 4b, 18c, 18d, 20a, 26a (main - 3d)

Hematite-filled injection veins

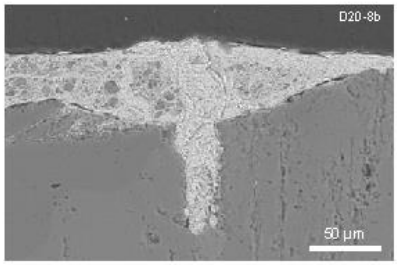

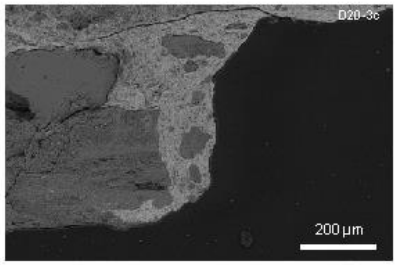

Other samples - 3b, 3d, 4a, 26a (main - 4b)

Reworked clasts and 'hematite' fish

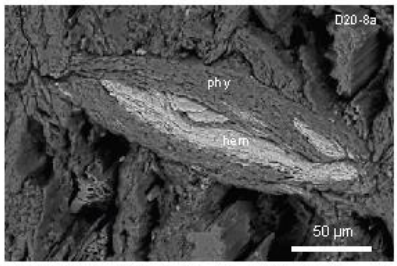

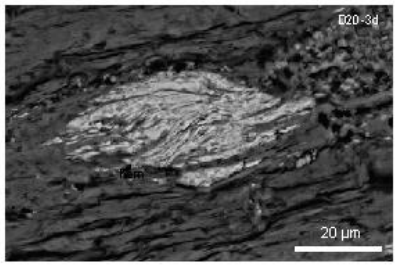

Other samples - 3b, 3c, 4a, 6a, 8a, 8b (main - 4b)

Figure A5. Additional SEM-BSE images of hematite microstructures. In addition to examples shown in images, other samples with each specific texture are noted.

Hematite tailed clasts and clast impressions

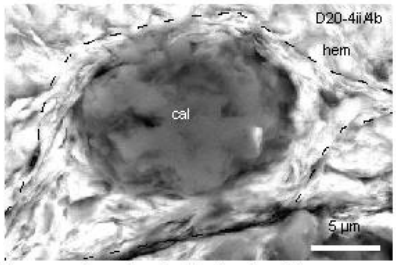

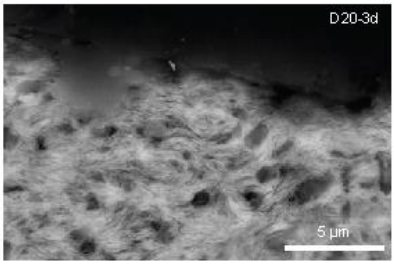

Other samples - 3a, 3b, 3c, 4a, 8a, 8b)

S-C fabrics developed in hematite

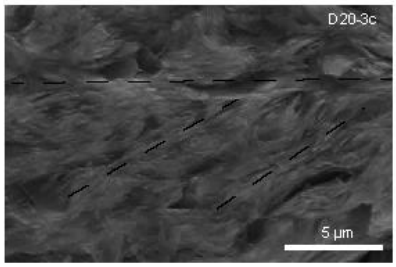

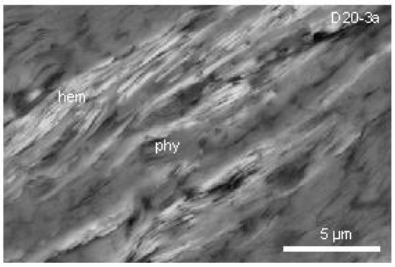

Other samples - 3d, 8a (main - 3b)

Clast-size sorted layers of hematite-matrix cataclasite

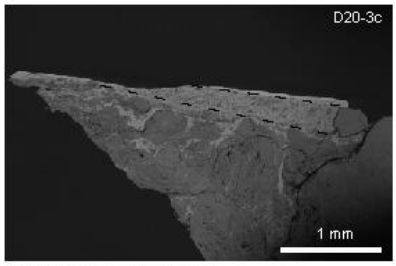

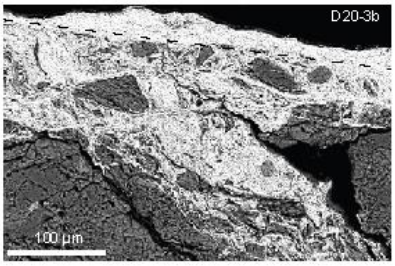

Other samples - 3a, 3d, 4a

Figure A5 (continued).

High aspect ratio plates

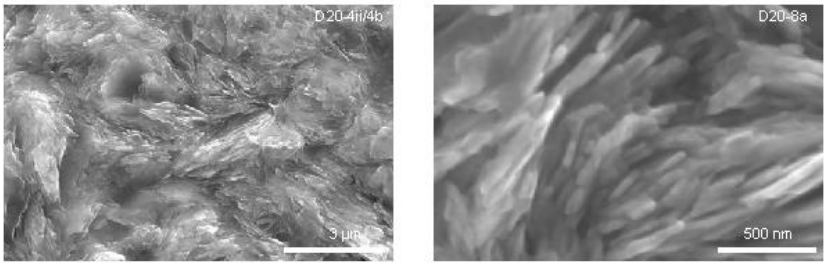

Other samples - 3b, 3c, 3d, 4a, 6a, 8b, 17g, 17h, 20a, 26a, 26b (main - 3a)

Plates with serrated grain boundaries

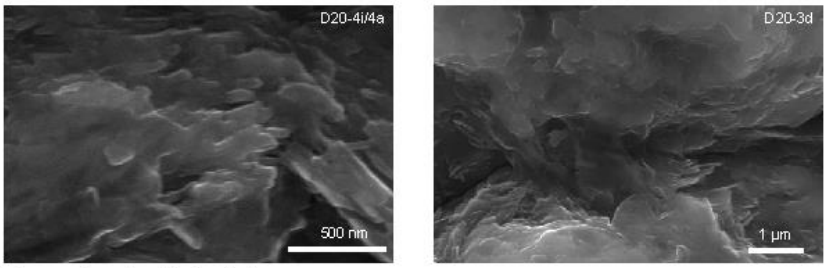

Other samples - 3a, 3b, 3c, 4b, 6a

Euhedral, hexagonal plates

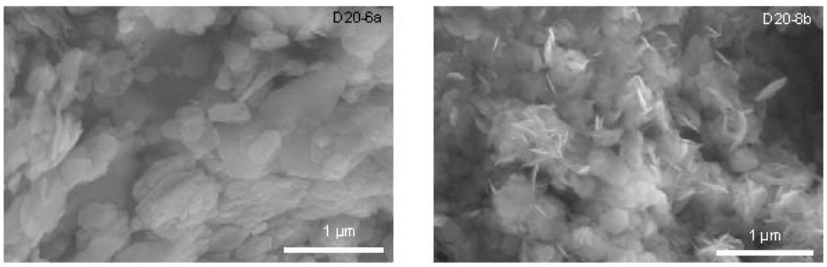

Other samples - 8a, 17g, 17h (main - 7)

Figure A6. Additional SEM-SE images of hematite morphologies. In addition to examples shown in images, other samples with each specific hematite grain morphologies are noted.

Stubby plates

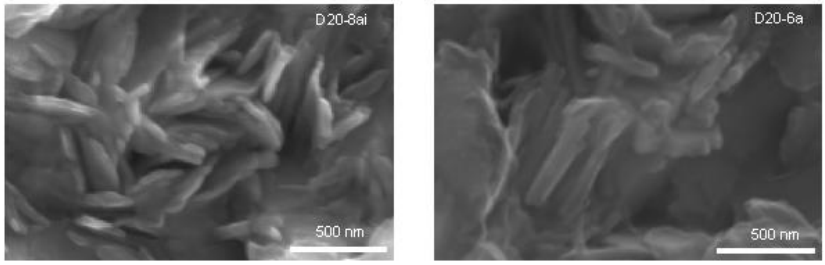

Other samples - 3c, 3d, 4a, 4b, 8aii 18c, 18d, 20a

'Petal'-shaped plates

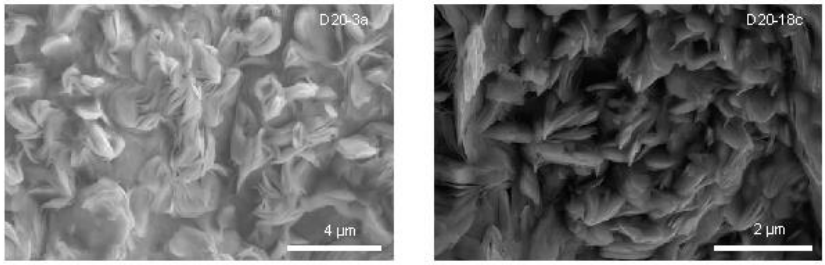

Other samples - 3b, 3c, 4a, 4b 8a, 8b, 17g, 17h, 18d, 20a, 26a, 26b

Figure A6 (continued).

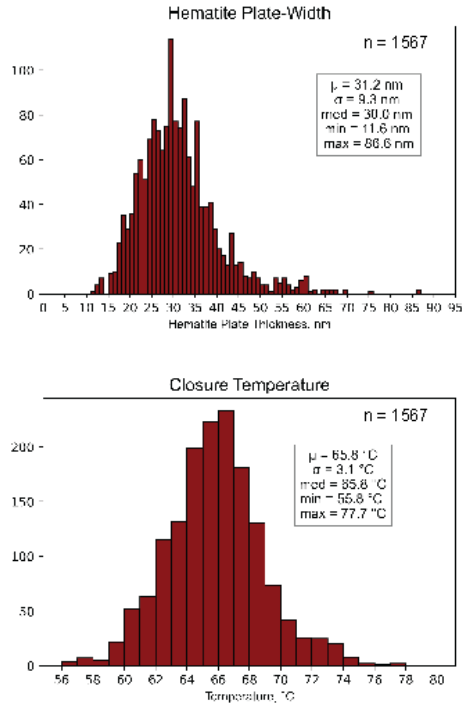

Figure A7. Histograms of hematite plate-width and calculated closure temperature (n = 1567 measurements). μ = mean, σ = standard deviation.

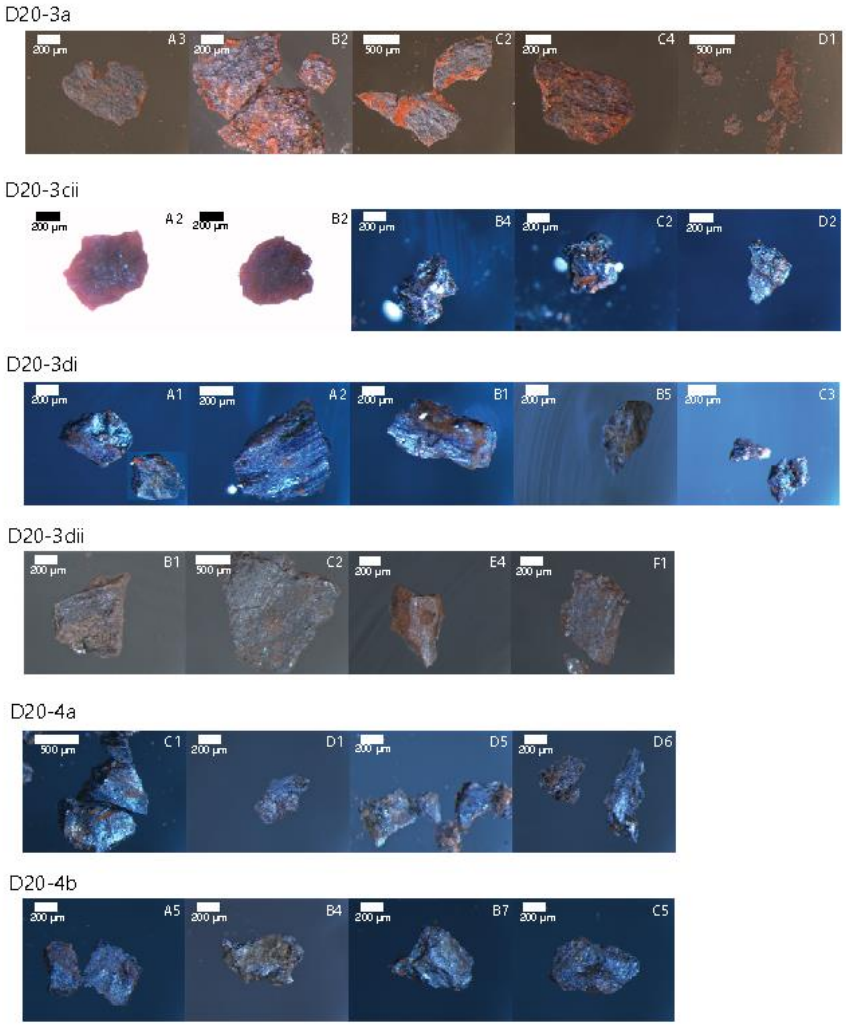

Figure A8. Stereoscopic photomicrographs of aliquots analyzed for (U-Th)/He thermochronometry.

D20-6aii

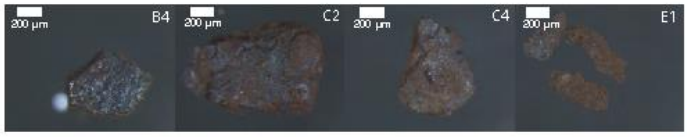

D20-6aiii

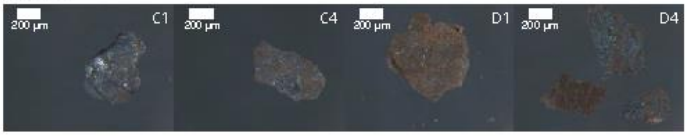

D20-8ai

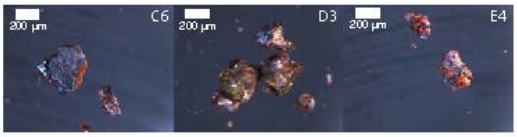

D20-8aii

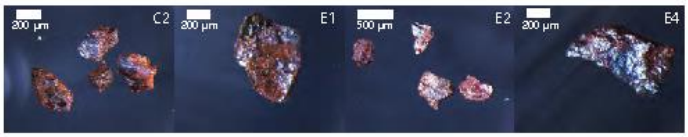

D20-8b

Figure A8 (continued).

D20-17g

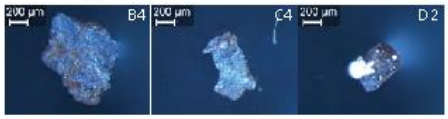

D20-17h

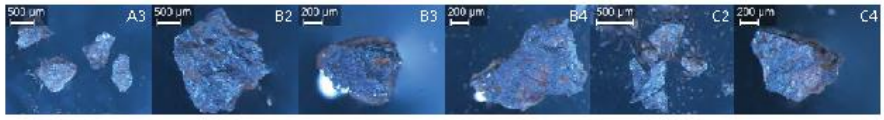

D20-18c

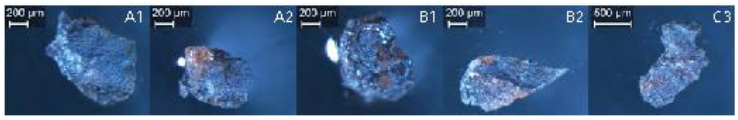

D20-18d

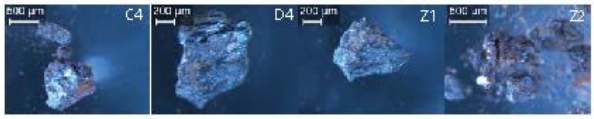

D20-20a

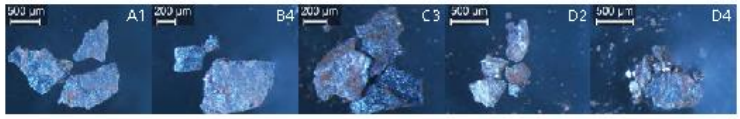

D20-26a

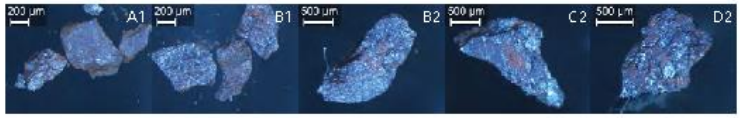

D20-26b

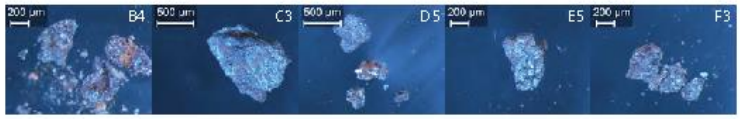

Figure A8 (continued).

In [1]:
```
import numpy as np
```

In [2]:
```
n = 10000000
rat = 0.045                                          #insert th/u ratio
hg = 75                                              #insert z height aliquot
sdU = 13.605                                         #stopping dist hematite U238/U235 abundances
sdTh = 16.04                                         #stopping dist hematite Th
sd = (sdU*(1/(1+rat))) + (sdTh*(rat/(1+rat)))        #calculates average stopping distance
```

In [3]:
```
#3-dimensional calculation

threedth = np.random.random(n)* 360 + -180           #generates polar angle
threedph = np.random.random(n)* 360 + -180           #generates azimuth angle
radth = np.deg2rad(threedth)
radph = np.deg2rad(threedph)
x = np.random.random(n)                              #generates initial x pos
y = np.random.random(n)                              #generates initial y pos
z = np.random.random(n)* hg + -hg                    #generates initial z pos
a = sd*np.cos(radph)*np.sin(radth)                   #x direction magnitude
b = sd*np.sin(radph)*np.sin(radth)                   #y direction magnitude
c = sd*np.cos(radth)                                 #z direction magnitude
s = (x+a, y+b, z+c)
q = np.sqrt(a*a + b*b + c*c)
sq = z+c                                             #z-direction new position

vec = (sq > 0).sum()                                 #loss in +z dir
nvec = (sq < -hg).sum()                              #loss in -z dir if not balanced
case = vec+nvec                                      #if both
FT = 1-(vec/n)                                       #FT if one side balanced
FTneither = 1-(case/n)                               #FT if He loss both sides

print(FT)
print(FTneither)
```

```
0.9418202
0.8836962
```

Figure A9. Python code implemented for F_T correction calculation (see text A3 for discussion).

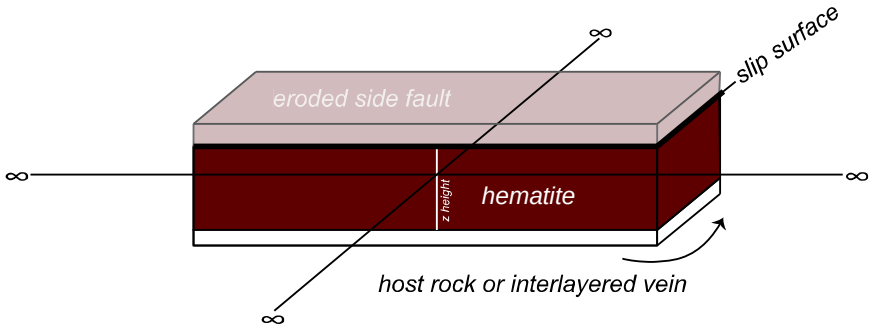

Figure A10. Schematic of hematite fault surface analyzed for (U-Th)/He thermochronometry demonstrating the parameters for the F_T correction (see text A3 for discussion).

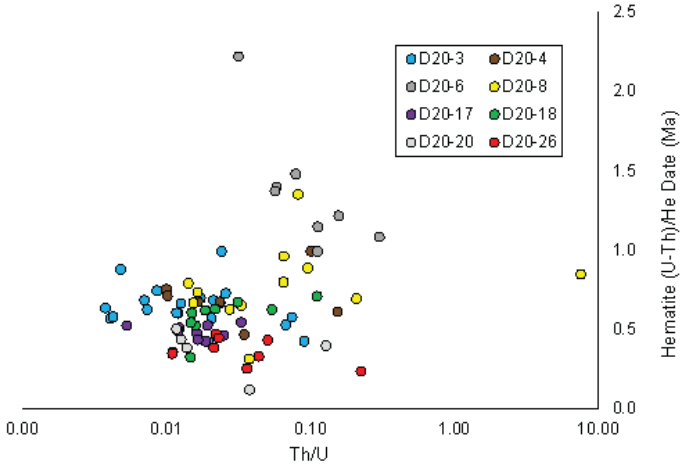

Figure A11. Individual hematite (U-Th)/He classified by sample as a function of Th/U to evaluate U loss during degassing (see text A2 for discussion).

APPENDIX B

Supporting information for Chapter III

B.1. Hematite (U-Th)/He analytical methods

Aliquots were analyzed for He, U, and Th contents at the Arizona Radiogenic Helium Dating Laboratory at the University of Arizona in September and October 2021. We used analytical methods described in Reiners et al. (2014), with some differences owing to the nature of our aliquots. Aliquots were heated with a diode laser in an ultra-high vacuum gas extraction line. This line has been modified to include a cold finger submerged in liquid N and charcoal getter to scavenge reactive gases from laser-heated aliquots *in vacuo* prior to spike addition. Aliquots were lased at temperatures comparable to apatite lasing (~975-1065 °C) associated with a packet "low glow" for 15-18 minutes. For all aliquots, a gas re-extract at higher lasing temperatures was performed to ensure that all He was extracted, and several aliquots required multiple re-extracts until negligible gas was released. Extracted He gas was spiked with ^{3}He, purified using cryogenic and gettering methods, and analyzed and measured on a quadrupole mass spectrometer. Analysis of a known quantity of ^{4}He was performed after every ~8 analyses of an unknown quantity to monitor instrumental sensitivity drift. Each planchette of Fe-oxides is processed with several line blanks, cold blanks, and hot blanks (on empty Nb packets) to constrain the ^{4}He/^{3}He ratios of unknown aliquots, together with ^{4}He/^{3}He ratios of ^{3}He shots. ^{4}He blanks from these procedures are on average ~0.005 fmol.

U and Th contents of each aliquot were measured by isotope dilution and solution ICPMS following the methods detailed in (Reiners, 2005). The degassed packets were dissolved in hydrochloric acid in a pressure digestion vessel (Parr bomb). Following addition of a ^{233}U-^{229Th} spike, equilibration, and dissolution, U and Th isotopes were measured on an Element 2 HR-ICP-MS. The ^{233}U-^{229}Th spike contains 0.4-0.8 ng of ^{233}U and 0.6-1.2 ng of ^{229}Th. Mean $^{238}U/^{233}U$ values of spike blanks and spike normals that accompanied each ICP-MS run are 0.002908 ± 0.000347 (± 1σ std. dev.) and 1.307907 ± 0.004961 (± 1σ std. dev.), respectively. Mean $^{232}Th/^{229}Th$ values spike blanks and spike normals are 0.001351 ± 0.0008809 (± 1σ std. dev.) and 2.366377 ± 0.0038271 (± 1σ std. dev.), respectively. Typical background corrections for U and Th come from analysis of the same empty Nb tubes and are 0.0003 ± 0.0001 ng U (± 1σ) and 0.0006 ± 0.0001 ng Th (± 1σ).

Blank corrected hematite (U-Th)/He dates were calculated with propagated analytical uncertainties from U, Th, and He measurements. Hematite dates were determined assuming that the grains were unzoned in U and Th. Dates in Table 3.5 are not reported with an F_t correction, due to the assumption that He implantation balances alpha (a)-ejection. Aliquots were acquired from slabs that were part of a large hematite boulder and hematite was visible on both the slip surface and the upper annulus following experiments, so these observations support α-ejection balancing implantation.

B.2. Hematite (U-Th)/He data outliers

We report all (n = 57) individual-aliquot hematite (U-Th)/He dates in Table 3.5, but we do not discuss a subset (~14%) of the dates in the main text owing to analytical issues manifest as high Th/U ratios (>0.7) and outlier dates.

Aliquots D21-PHe4_h3, D21-PV1P_h2, and all five aliquots from D21-PHe3 (h1-h5) yield Th/U ratios (>0.7) that exceed the rest of the dataset. The majority of aliquots from deformed gouge yield Th/U ratios that overlap with ratios of undeformed homogenized starting material. However, aliquots D21-PHe4_h3 and D21-PV1P_h2 yield high Th/U ratios (0.875 and 1.067, respectively) and lower U compared to other aliquots from the same sample. These observations may support U volatilization, but their younger dates (141 Ma, 146 Ma) compared to other aliquots in these samples and across the dataset do not support this. Regardless, we do not include these aliquots in our interpretations due to concerns of anomalous errors. We do not discuss gouge data from experiment D21-PHe03, which utilized a SiC upper annulus, and all aliquots from this experiment exhibit high Th/U ratios (>1) and yield young dates (<120 Ma). These aliquots may reflect Th addition from breakdown of the SiC upper annulus during the experiment (Calzolari et al., 2020). Prior ICPMS analyses of the SiC reveals that this material has anomalously high Th content.

We do not discuss aliquot D21-PHe5_h3 because its date (~303 Ma) is a notable outlier for the entire dataset. The aliquot was sampled from gouge on a deformed hematite slab, but it is older than all undeformed homogenized starting material *and* all individual plates analyzed in Calzolari et al. (2020). This cause of this anomalously old date is not known.

To summarize, we exclude seven dates from deformed gouge and one date from undeformed material in the discussion of results in the main text. These anomalous dates are associated with an unknown source of error that manifests as high Th/U ratios and/or outlier dates, and high Th/U ratios due to Th implantation from the upper annulus.

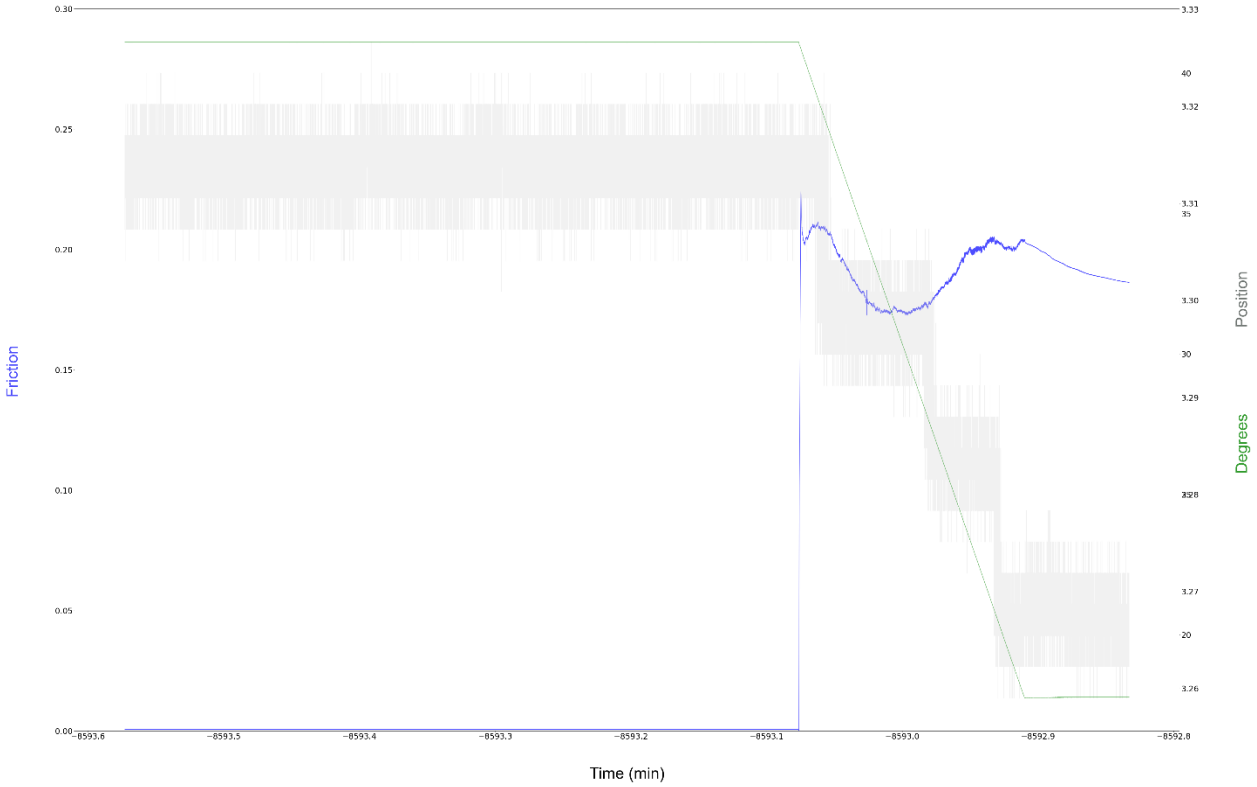

Figure B1. Values of coefficient of friction calculated over time for experiment PHe01.

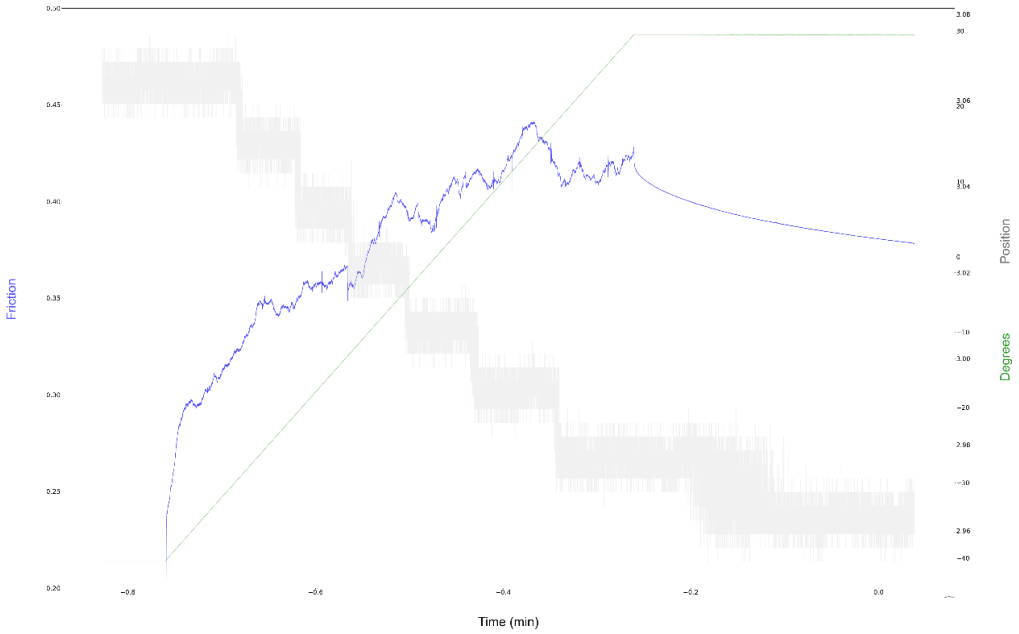

Figure B1 (cont). Values of coefficient of friction calculated over time for experiment PHe02.

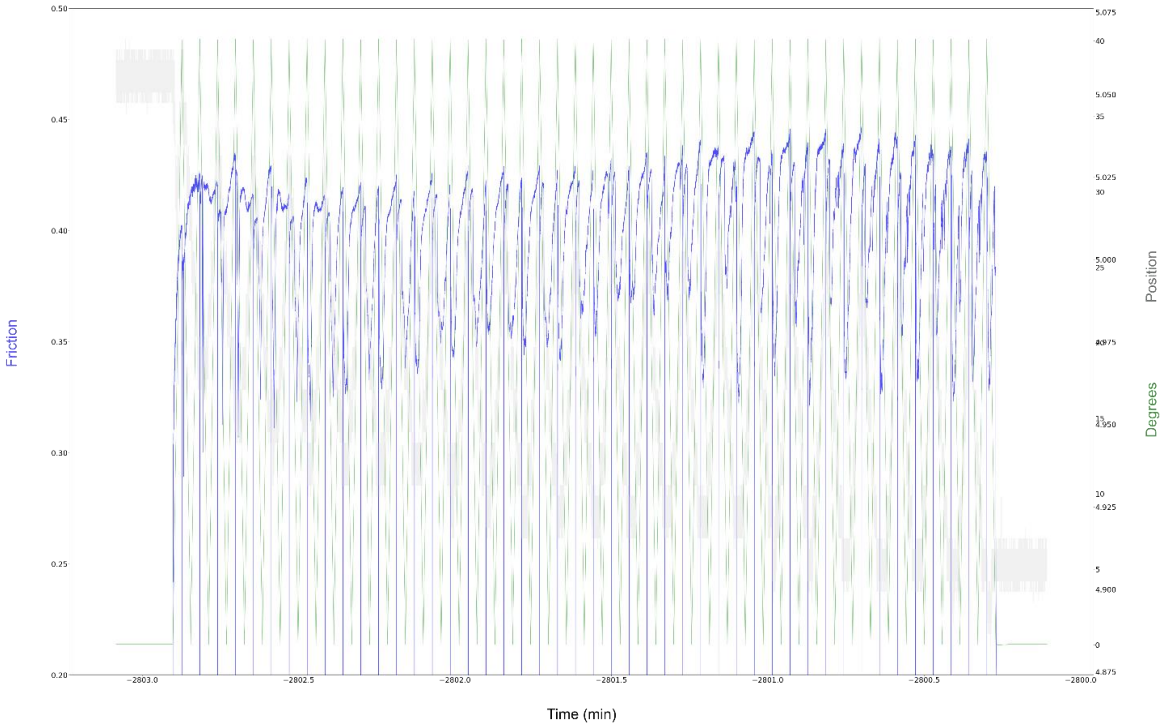

Figure B1 (cont). Values of coefficient of friction calculated over time for experiment PHe03.

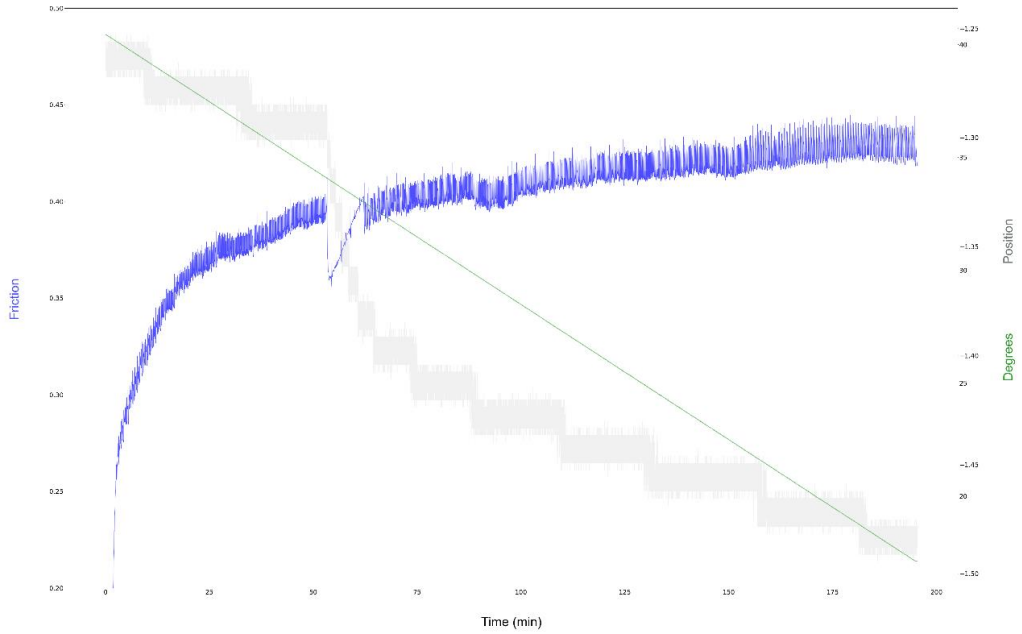

Figure B1 (cont). Values of coefficient of friction calculated over time for experiment PHe04.

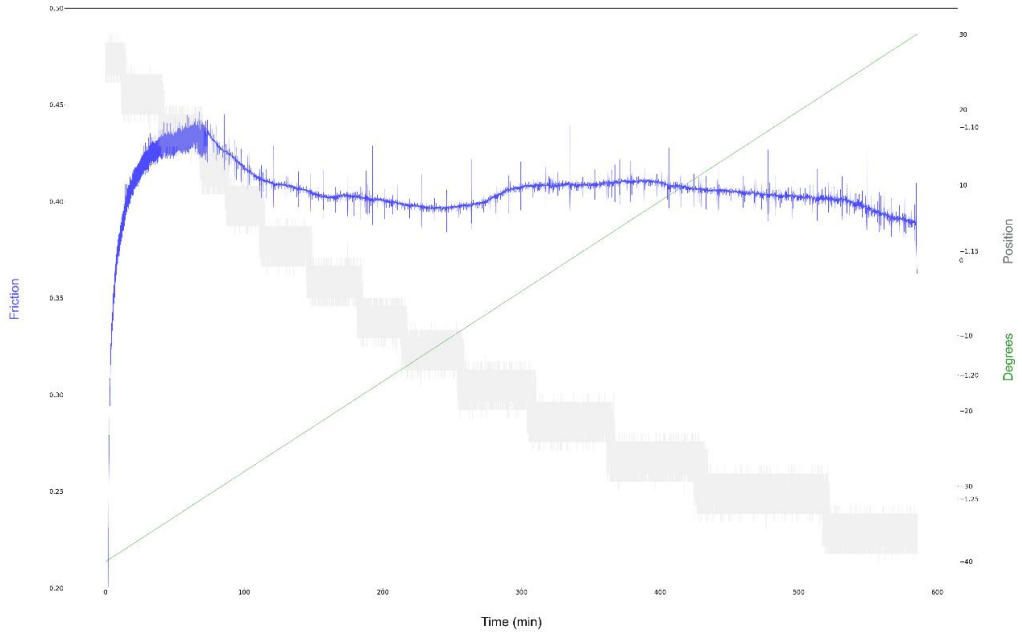

Figure B1 (cont). Values of coefficient of friction calculated over time for experiment PHe05.

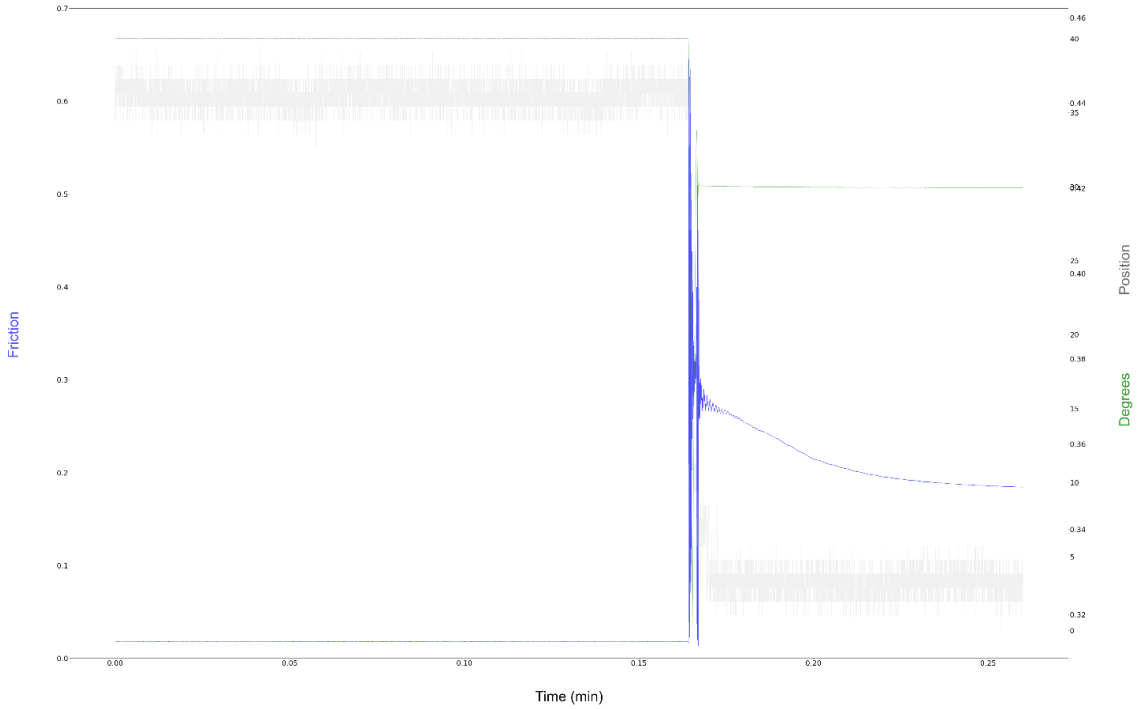

Figure B1 (cont). Values of coefficient of friction calculated over time for experiment PHe06.

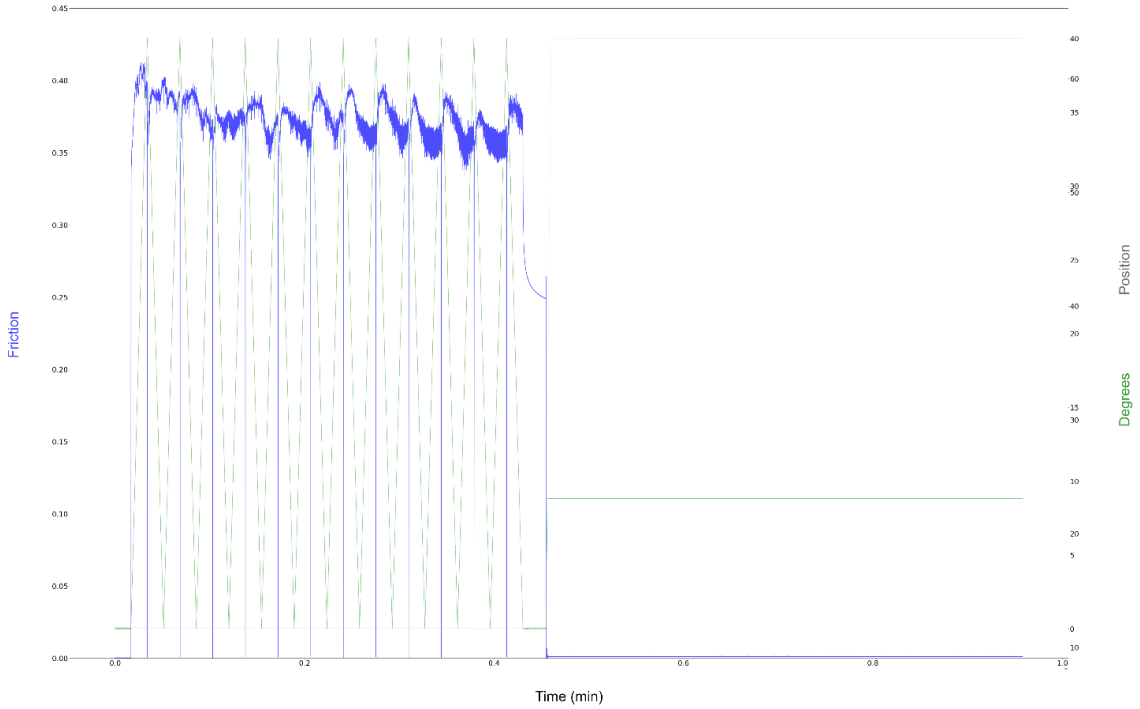

Figure B1 (cont). Values of coefficient of friction calculated over time for experiment Test001.

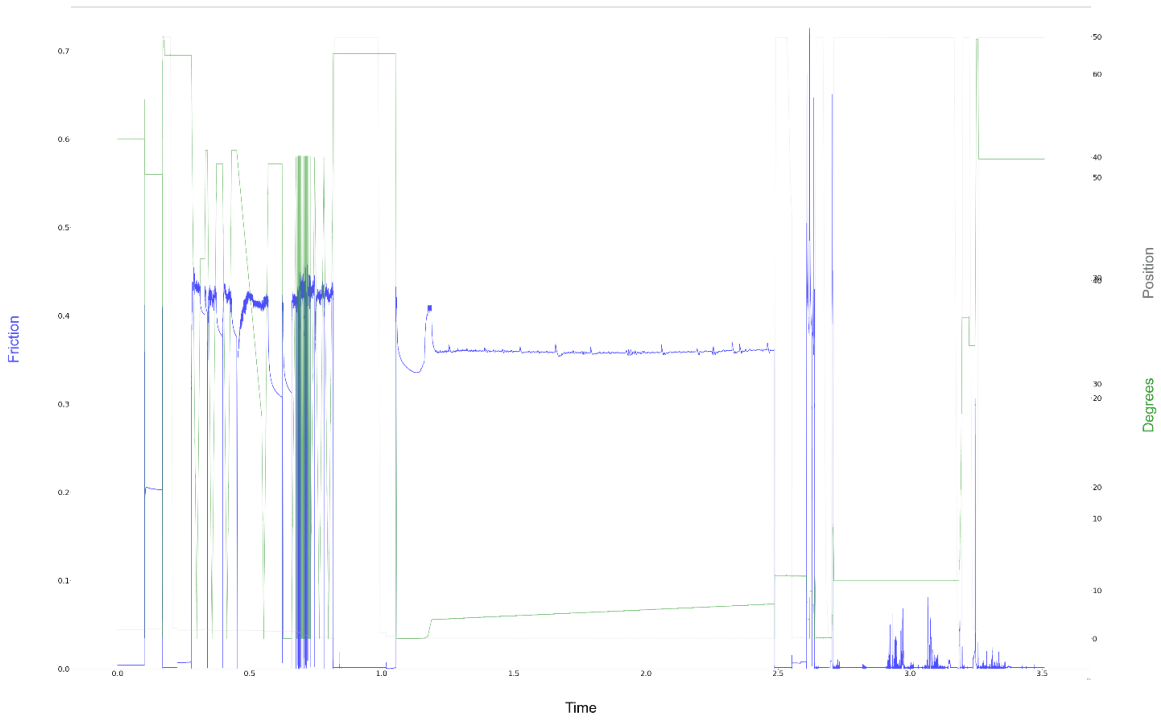

Figure B1 (cont). Values of coefficient of friction calculated over time for experiment Mock.

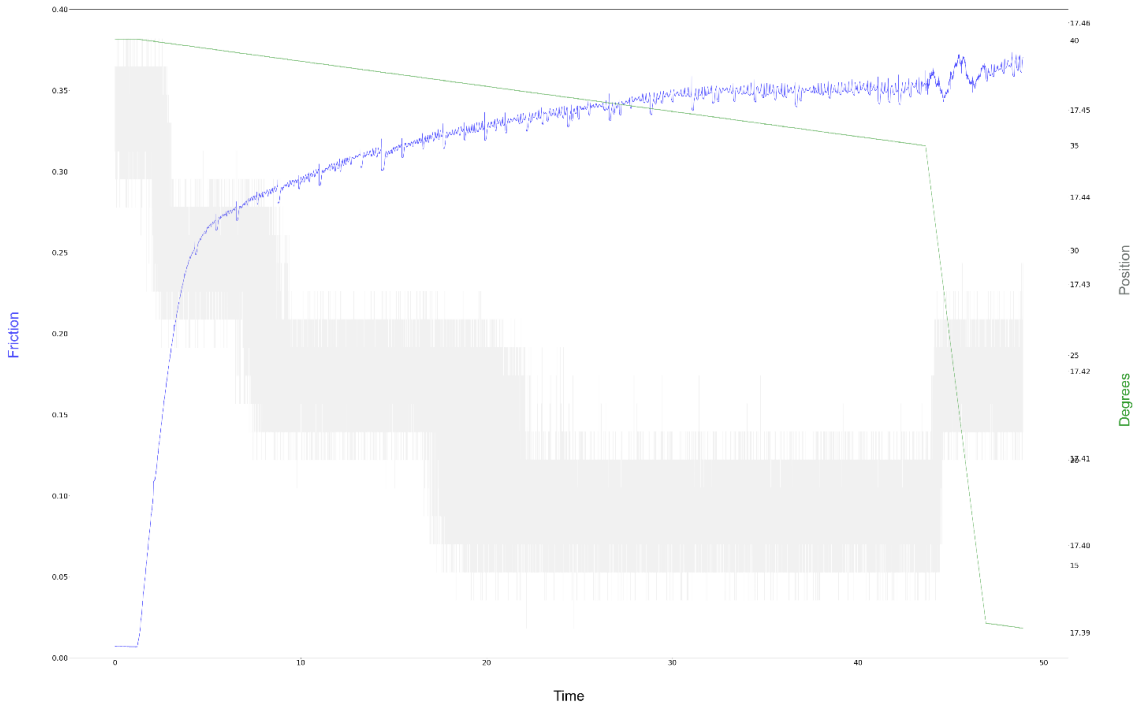

Figure B1 (cont). Values of coefficient of friction calculated over time for experiment Plan1.

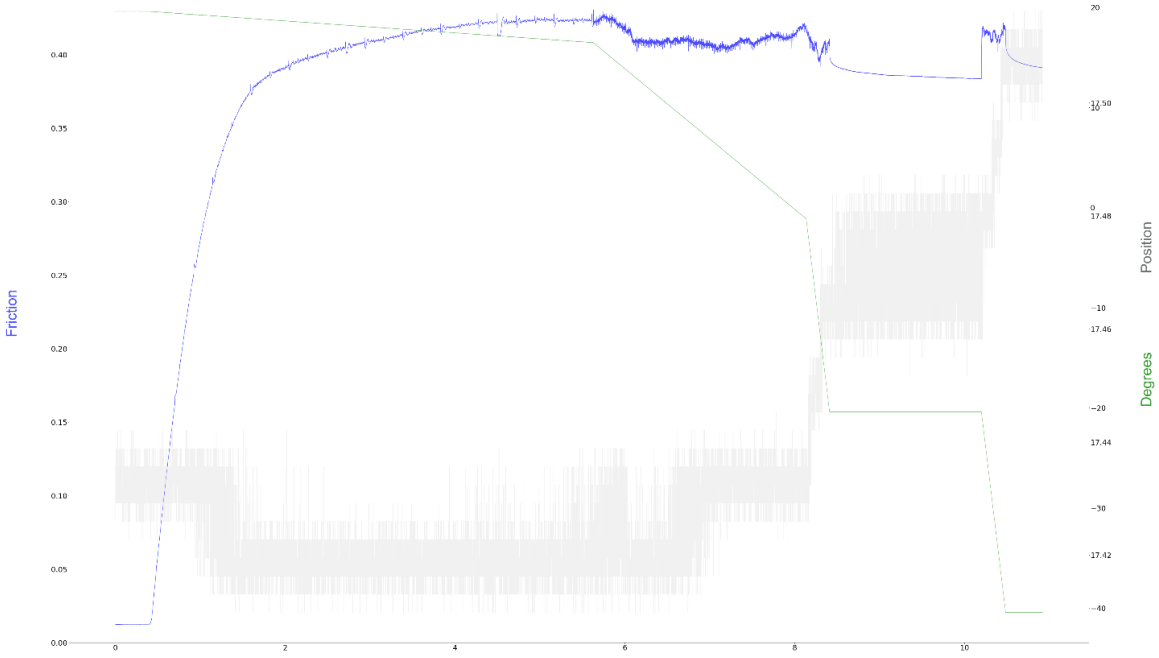

Figure B1 (cont). Values of coefficient of friction calculated over time for experiment Plan2.

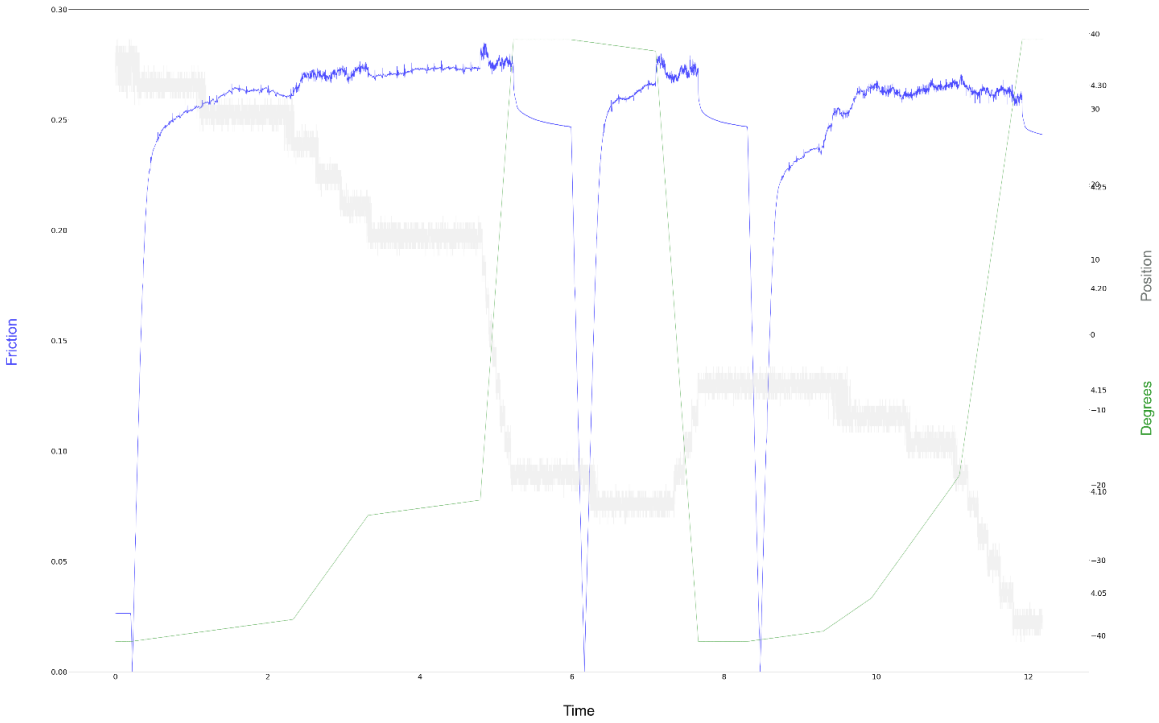

Figure B1 (cont). Values of coefficient of friction calculated over time for experiment Setup1.

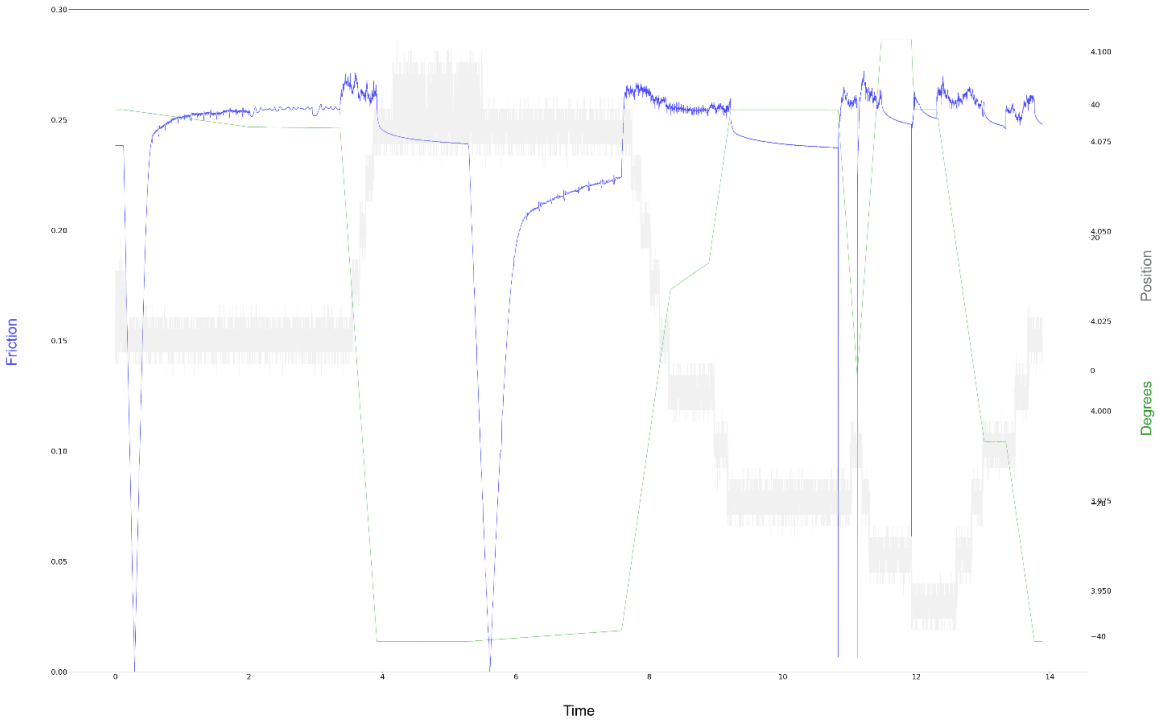

Figure B1 (cont). Values of coefficient of friction calculated over time for experiment Setup2.

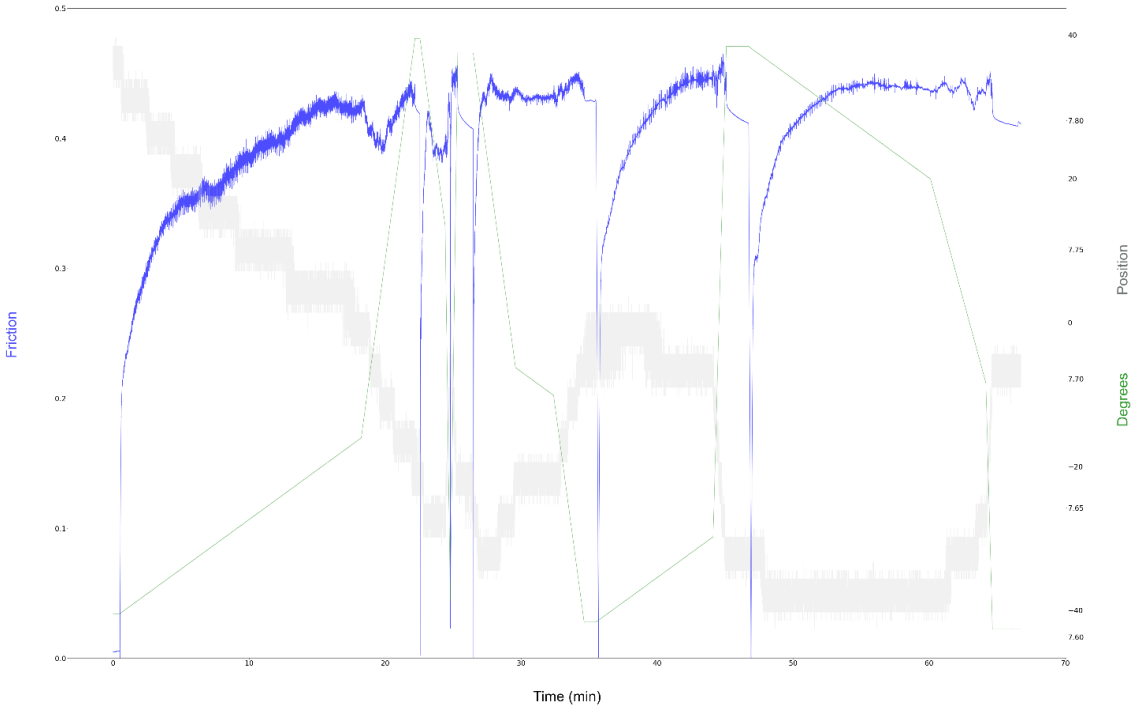

Figure B1 (cont). Values of coefficient of friction calculated over time for experiment PV1.

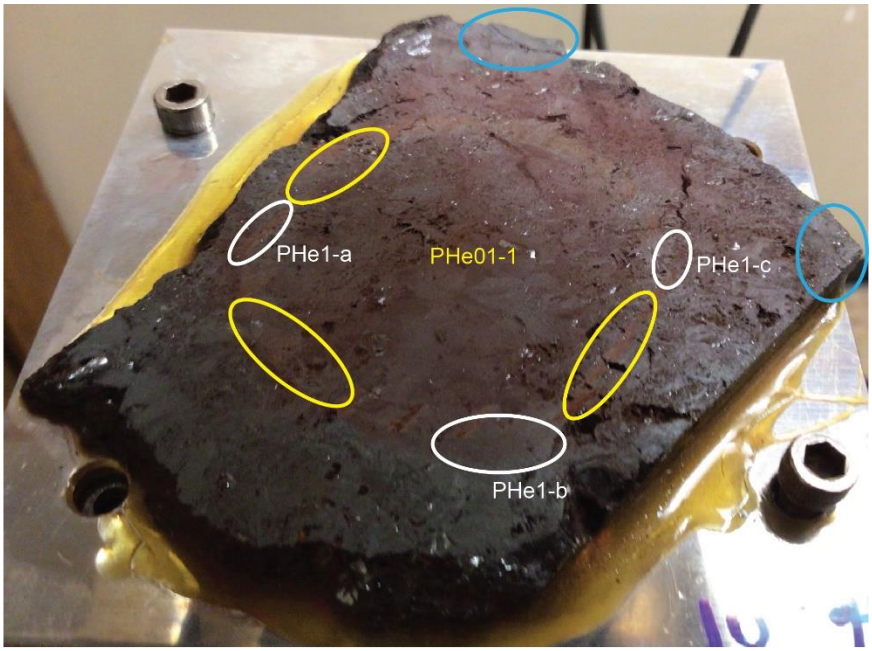

D21-PHe-01

Blue - undeformed homogenized material for (U-Th)/He
Yellow - deformed gouge for (U-Th)/He
White - SEM microstructures
inner diameter of ring ~44.35 mm

Figure B2. Plate PHe01 with sampling locations circled.

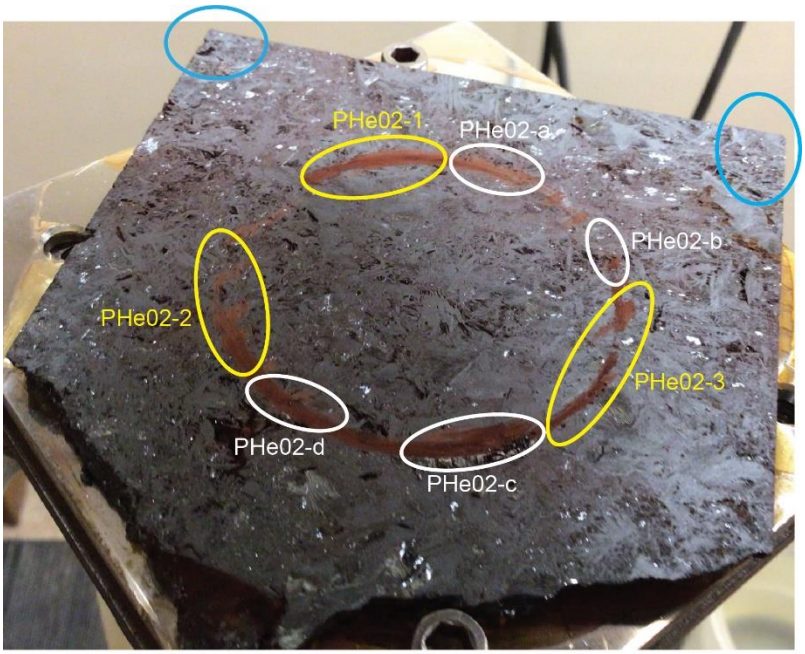

D21-PHe-02
Blue - undeformed homogenized material for (U-Th)/He
Yellow - deformed gouge for (U-Th)/He
White - SEM microstructures
inner diameter of ring ~44.35 mm

Figure B2 (cont). Plate PHe02 with sampling locations circled.

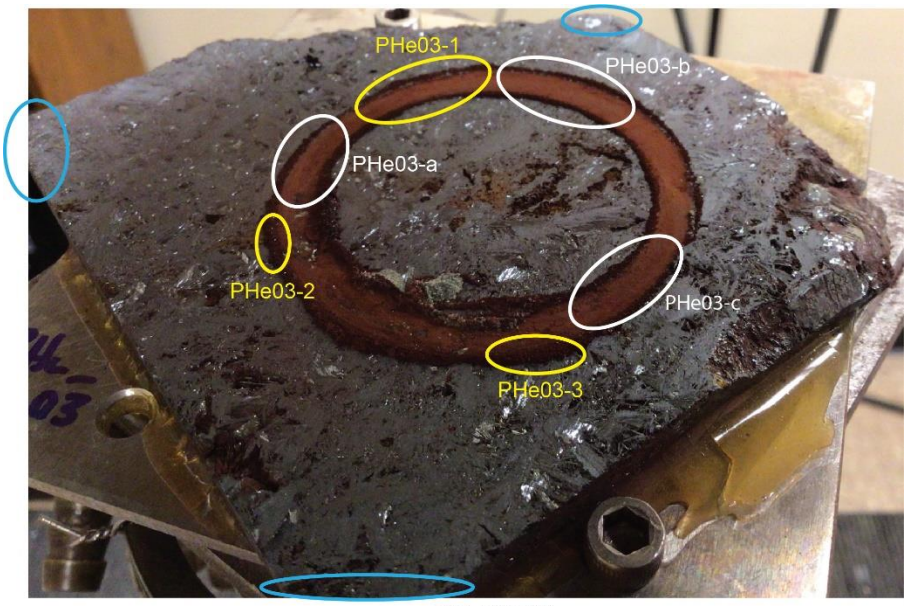

D21-PHe-03
Blue - undeformed homogenized material for (U-Th)/He
Yellow - deformed gouge for (U-Th)/He
White - SEM microstructures
inner diameter of ring ~44.35 mm

Figure B2 (cont). Plate PHe03 with sampling locations circled.

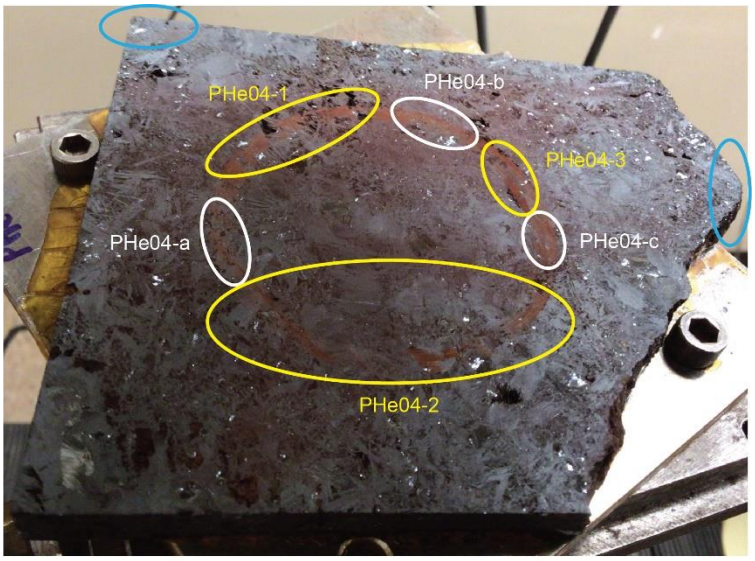

D21-PHe-04
Blue - undeformed homogenized material for (U-Th)/He
Yellow - deformed gouge for (U-Th)/He
White - SEM microstructures
inner diameter of ring ~44.35 mm

Figure B2 (cont). Plate PHe04 with sampling locations circled.

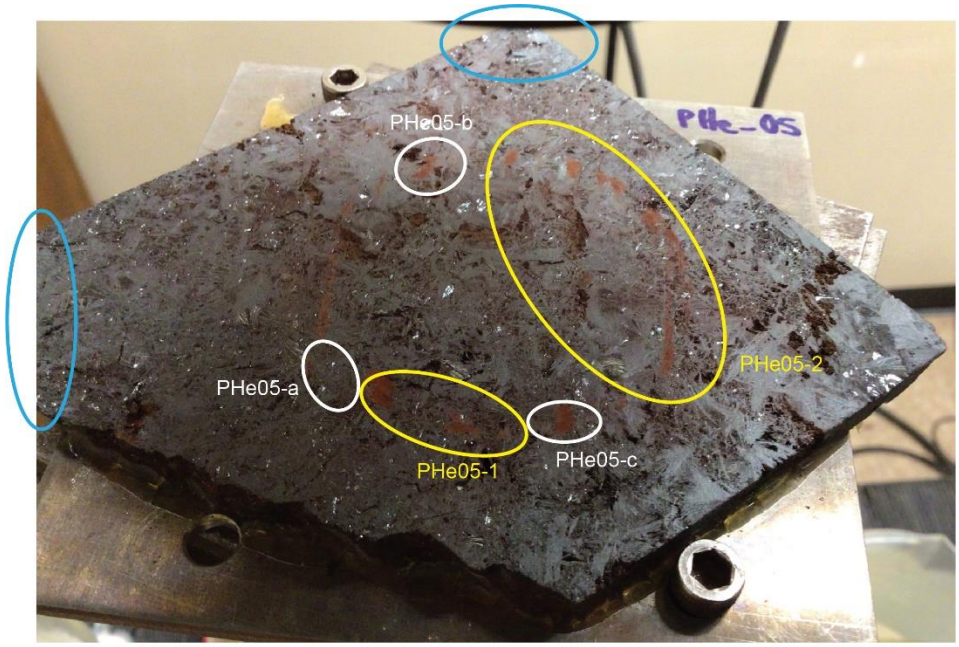

D21-PHe-05

Blue - undeformed homogenized material for (U-Th)/He
Yellow - deformed gouge for (U-Th)/He
White - SEM microstructures
inner diameter of ring ~44.35 mm

Figure B2 (cont). Plate PHe05 with sampling locations circled.

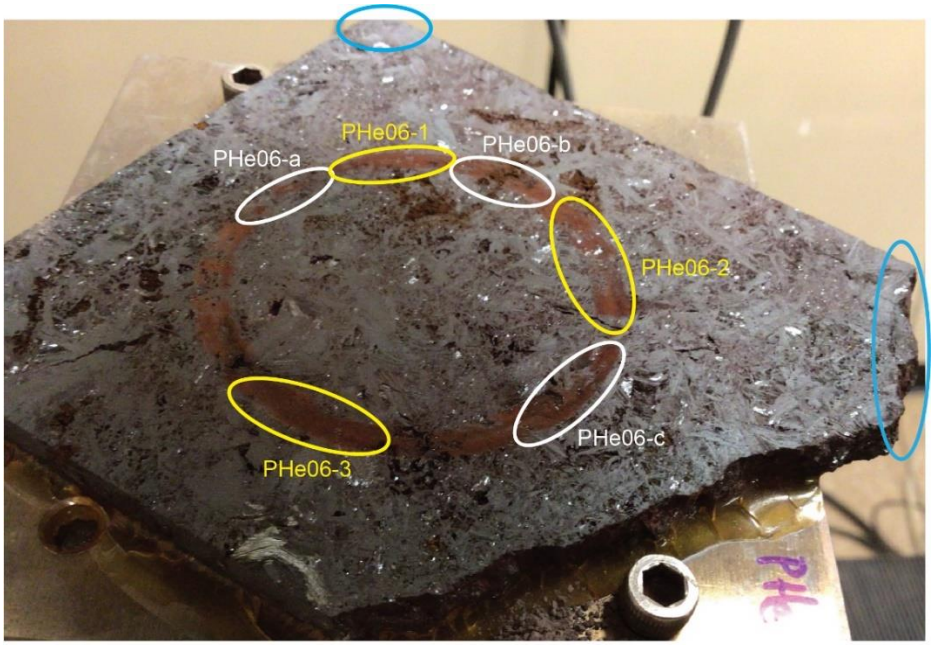

Figure B2 (cont). Plate PHe06 with sampling locations circled.